

**DESIGN AND SYNTHESIS TECHNIQUES FOR
RECONFIGURABLE MICROWAVE FILTERS USING
SINGLE AND DUAL-MODE RESONATORS**

A Dissertation
Presented to
The Academic Faculty

By

Cesar A. Lugo Jr.

In Partial Fulfillment
of the Requirements for the Degree
Doctor of Philosophy
in
Electrical and Computer Engineering



School of Electrical and Computer Engineering
Georgia Institute of Technology
December 2006

Copyright © 2006 by Cesar A. Lugo Jr.

DESIGN AND SYNTHESIS TECHNIQUES FOR RECONFIGURABLE MICROWAVE FILTERS USING SINGLE AND DUAL-MODE RESONATORS

Approved by:

Dr. John Papapolymerou, Advisor
Assoc. Professor, School of ECE
Georgia Institute of Technology

Dr. James Hamblen
Professor, School of ECE
Georgia Institute of Technology

Dr. Manos Tentzeris
Assoc. Professor, School of ECE
Georgia Institute of Technology

Dr. Dennis Hess
Professor, School of Chemical and Biomolecular Engineering
Georgia Institute of Technology

Dr. John Cressler
Professor, School of ECE
Georgia Institute of Technology

Date Approved: December 1, 2006

TABLE OF CONTENTS

ACKNOWLEDGMENTS	iv
LIST OF TABLES	v
LIST OF FIGURES	vi
LIST OF SYMBOLS AND ABBREVIATIONS	x
SUMMARY	xii
CHAPTER 1 INTRODUCTION	1
CHAPTER 2 BACKGROUND	6
CHAPTER 3 FRACTIONAL BANDWIDTH VARIATION TECHNIQUES . .	10
3.1 Coupling Variation and Length Compensation	10
3.2 Reconfigurable Filter Design with Bandwidth Control at 5.8 GHz	12
3.3 Six State All Tunable X-Band Filter	19
3.4 Chapter Summary	29
CHAPTER 4 DUAL-MODE RECONFIGURABLE FILTERS	31
4.1 Square Loop Topology with Bandwidth Control	32
4.2 Single Switch Triangular Patch Topology	39
4.3 Chapter Summary	46
CHAPTER 5 FILTERS WITH ASYMMETRICAL RESPONSES	48
5.1 Asymmetrical Response of the Dual-Mode Triangular Loop Resonator . .	49
5.2 Topology with Asymmetrical Control of Transmission Zeros	55
5.3 Chapter Summary	62
CHAPTER 6 FERROELECTRIC FILTERS AND MEMS SWITCHES	64
6.1 Continuous Tuning using Ferroelectric Capacitors	64
6.2 Bandwidth Control using MEMS Switches	67
6.3 Chapter Summary	78
CHAPTER 7 PLANAR REALIZATION OF A TRIPLE-MODE FILTER . .	79
7.1 Multilayer Approach for Third Order Degeneracy	80
7.2 Triple-Mode Design Methodology	89
7.3 Chapter Summary	93
CHAPTER 8 CONCLUSION AND FUTURE WORK	94
8.1 Future Work	95
REFERENCES	96

ACKNOWLEDGMENTS

First, I would like to thank my mother Beatriz Lugo and my father Cesar Lugo Sr. They have always emphasized the importance of strong education and spiritual values. I especially appreciate their support through out my years as a student at Georgia Tech. My mother has been very strong, particularly after seeing the sizes of the Georgia Tech dorms, where I lived for four years.

I would like to thank my PhD advisor, Dr. John Papapolymerou. He has been actively involved in many aspects of this thesis, and has provided many intellectual contributions to this research. His work as an advisor has gone beyond expectation, not only in facilitating the financial resources needed to make this investigation possible, but also by making sure that the work was significant. He has also emphasized the importance of appropriate research allowing my exposure to several projects with industry collaboration.

I am grateful for being part of the Georgia Tech family. My long years in this school have been difficult, filled with many sleepless nights, but they have also been very rewarding. I have probably taken at least one class with almost every professor in the ECE department; their work has provided me with a unique learning experience. I would like to thank my fellow graduate students from the microwave circuit technology group. I am greatly thankful for their contributions to this work. Their help in fabrications, measurements and technical discussions were countless.

I am thankful for the work provided by the nGimat personnel, their collaboration has made possible the combined use of ferroelectric and MEMS switches in reconfigurable filters. Also many thanks to Dr. Guoan Wang for helping in the fabrication of the MEMS switches used in some of my designs. Finally, I extend a "thank you" to the rest of the Georgia Tech staff for their necessary work.

LIST OF TABLES

Table 1	Filter Responses Vs. Diode Biasing	21
Table 2	Measured Filter Characteristics	24
Table 3	Third Order Intercept Points	45
Table 4	Resonant Frequencies and Coupling Factor	51

LIST OF FIGURES

Figure 1	Simplified schematic of a doppler radar.	2
Figure 2	Simplified schematic of a frequency division multiplexed microwave radio receiver.	3
Figure 3	Conventional second order admittance inverter microstrip filter.	10
Figure 4	Second order filter with added tuning stubs for bandwidth tuning.	12
Figure 5	Layout of tunable filter with bias lines.	15
Figure 6	Picture of fabricated filter.	15
Figure 7	Measured and simulated S21 parameters of wideband state.	16
Figure 8	Measured and simulated S21 parameters of Narrowband state.	17
Figure 9	Measured and simulated S11 parameters of wideband state.	18
Figure 10	Measured and simulated S11 parameters of narrowband state.	18
Figure 11	Intermodulation measurement setup.	19
Figure 12	Antenna system with reconfigurable filter.	20
Figure 13	Proposed topology.	21
Figure 14	Picture of fabricated filter with diodes and bias lines.	24
Figure 15	Wideband measurement results (solid line), simulated results (dashed line). (a) Transmission loss. (b) Return loss.	25
Figure 16	Narrowband measurement results (solid line), simulated results (dashed line). (a) Transmission loss(b) Return loss.	26
Figure 17	Measured intermodulation third order intercepts IIP3.	28
Figure 18	Conceptual treatment of intermediate resonators in higher order tunable filters.	29
Figure 19	Microstrip loop and patch resonator topologies for dual-mode operation (a) square shape (b) triangular shape (c) circular shape	31
Figure 20	Reconfigurable dual-mode square loop topology	33

Figure 21	Electric field distribution at the center frequency. (a) Electric field distribution of a single mode (topology without perturbations) (b) Narrow-band state. (c) Wideband state. Dark sections represent electric field minima. Light sections represent electric field maxima.	35
Figure 22	Picture of fabricated filter with DC bias lines	35
Figure 23	Measured and simulated S21 parameters of the wideband and narrow-band state	37
Figure 24	Measured and simulated S11 parameters of the wideband and narrow-band state	37
Figure 25	Measured intermodulation third order intercepts IIP3	38
Figure 26	Higher order filters using dual-mode square loops. (a) Four pole filter configuration. (b) Four pole filter with non resonant nodes	38
Figure 27	Current distributions of the degenerate modes in a microstrip triangular patch (a) Even mode (mode 1). (b) Odd mode (mode 2).	40
Figure 28	Proposed reconfigurable filter.	40
Figure 29	2-pole filter with weakly input/output coupling and variable tuning stub length S.	42
Figure 30	Simulated frequency location of the resonant poles produced by the filter in Fig. 29.	43
Figure 31	Picture of fabricated filter.	43
Figure 32	Measured and simulated transmission loss.	44
Figure 33	Measured and simulated return loss.	45
Figure 34	Standard cascaded configuration to produced higher order filters using dual-mode triangular patch resonators	46
Figure 35	Proposed topology	48
Figure 36	Topology configuration with respective simulated electric field pattern. (a) $p = r = 0$. (b)-(c) $p < r$. (d)-(e) $p > r$. Lighter sections indicate field's maxima. Darker sections indicate field's minima.	49
Figure 37	(a) Transmission line model (b) Model with magnetic wall for even mode (b) Model with electric wall for odd mode.	50
Figure 38	Transmission line model response (solid line) Vs. Chebyshev filtering function (dotted line) with (a) zeros at $s = 6.53$ and $j15.21$ (b) zeros at $s = -j6.53$ and -15.21	53

Figure 39	Measurement results (solid line), EM simulation results (dashed line). (a) Configurations with $p < r$. (b) Configurations with $p > r$	54
Figure 40	Higher order realizations using triangular loop resonators	54
Figure 41	Proposed reconfigurable filter topology.	55
Figure 42	Polarization of degenerate modes. (a) conventional coupling scheme (b) coupling scheme with cross coupling	57
Figure 43	Frequency responses from coupling matrices M . Dotted line with sym- metrical placement of zeros ($s = .95$ mm), M_0 ($s = 0$ mm) and M_1 ($s =$ 1.34 mm) vs. angular frequency normalized to $f_0 = 10$ GHz	58
Figure 44	Coupling matrix schematic (a) Symmetrical placement of zeros with $s =$.95 mm and $M(2, 2) = 1.32$, $M(3, 3) = 3.42$. (b) M_1 with $s = 1.34$ mm. (c) M_0 with $s = 0$ mm.	59
Figure 45	Picture of Fabricated Filter.	60
Figure 46	Measured (solid line) and simulated (dotted line) S21 and S11 param- eters	60
Figure 47	Resonator configuration for higher order tunable filter realizations	61
Figure 48	Proposed filter schematic. (a) 2pole filter. (b) 3-pole filter.	64
Figure 49	Cross section of a BST gap capacitor (not to scale).	65
Figure 50	Capacitance versus bias voltage of a BST gap capacitor.	66
Figure 51	Layout of MEMS tuning mechanism for bandwidth control.	68
Figure 52	Simulated response. Marker at 42.5 GHz corresponds to a pole location in the wideband response and a 10 dB rejection in the narrowband response. 69	
Figure 53	Current density distribution at 42.5 GHz (a) Wideband state. (b) Nar- rowband state.	70
Figure 54	Geometry of the meander-shaped support.	71
Figure 55	Picture of fabricated filter.	71
Figure 56	Effect of fixed input/output coupling and BST loss on filter response. . .	73
Figure 57	Transmission loss of 2-pole filter measured wideband state (MEMS switches up).	74
Figure 58	Return loss of 2-pole filter measured wideband state (MEMS switches up). 74	

Figure 59	Transmission loss of 2-pole filter measured narrowband state (MEMS switches down).	75
Figure 60	Return loss of 2-pole filter measured narrowband state (MEMS switches down).	75
Figure 61	Transmission loss of 3-pole filter measured wideband state (MEMS switches up).	76
Figure 62	Return loss of 3-pole filter measured wideband state (MEMS switches up).	76
Figure 63	Transmission loss of 3-pole filter measured narrowband state (MEMS switches down).	77
Figure 64	Return loss of 3-pole filter measured narrowband state (MEMS switches down).	77
Figure 65	Proposed topology.	80
Figure 66	Filter cross-section.	82
Figure 67	Top view of proposed resonator including cavity with periodic via walls.	82
Figure 68	Rotations of planes with minima and maxima electric field, (a) E_1 at $f_{01} = f_0$, symmetrical plane with normal $N_1 = z$ ($\theta_1 = 0$ and $\phi_1 = 0$), (b) E_2 at $f_{02} > f_0$ plane with normal N_2 ($\theta_2 = 345^\circ, \phi_2 = 19.65^\circ$), (c) E_3 at $f_{03} < f_0$ with normal vector N_3 ($\theta_3 = 375^\circ, \phi_3 = 19.65^\circ$)	84
Figure 69	Electric field intensity patterns for (a) E_1 even-mode with field minima along plane AA' ($\delta_1 = 45^\circ$) (b) E_2 with field minimum along plane BB' ($\delta_2 = 75^\circ$) (c) E_3 with field minimum along plane CC' ($\delta_3 = 105^\circ$)	84
Figure 70	Equivalent circuit model for a triple mode filter with fully canonical response.	86
Figure 71	Simulated response for $p = 20, 25, 30$ mil and optimal $r = 22$ mil.	88
Figure 72	Simulated response for $r = 19, 22, 25$ mil and optimal $p = 25$ mil.	88
Figure 73	Construction layers for the fabricated triple mode filter.	90
Figure 74	Measured (solid line) vs. simulated (dashed line).	91
Figure 75	Conceptual realization of higher order filters	92

LIST OF SYMBOLS AND ABBREVIATIONS

RF	radio frequency.
DC	direct current.
Q_u	unloaded quality factor.
Q_e	external quality factor.
YIG	yttrium iron garnet.
MEMS	micro-electro-mechanical-systems.
CPW	coplanar-waveguide.
f	frequency.
k	coupling factor.
J	inverter constant.
B	susceptance
C	capacitance
Y	admittance
G	filter prototype element constant
Δ	fractional bandwidth
$\theta_{resonator}$	positive electric length
$\varphi_{resonator}$	negative electric length
GHz	gigahertz = 10^9 cycles per second
$\tan\delta$	loss tangent
dB	decibel
Δf	frequency shift

IIP3	third order intermodulation intercept point
ω	normalized angular frequency
I/O	input/output coupling
ϵ_r	relative permittivity
λ_g	guided wavelength
IL	insertion loss
RL	return loss
I_f	forward bias current
V_r	reverse bias voltage
Z_{in}	input impedance
C_N	chebyshev filtering function
M	cupling matrix
BST	barium sronioum titanate.
ITO	indium tin oxide
CCVD	combustion chemical vapor deposition
k_{eff}	effective spring constant
ϵ_o	permittivity of air
ν	poissons ratio
SOLT	short-open-load-through
TM	transfer magnetic
TE	transfer electric
HEM	hybrid electric magnetic

SUMMARY

This thesis discusses the investigation and development of design methodologies for the creation of multi-functional bandpass filters at microwave frequencies. These filters are capable of tuning to different frequency bands as well as varying their fractional bandwidth. The research also studies polynomial synthesis procedures as a tool for the derivation of reconfigurable planar filters with advanced asymmetrical responses.

The work presented here relates to the evolving multifunction philosophy of RF systems. This analysis presents a comprehensive study of microwave resonators, which generate reliable and scalable filter topologies with tunable properties. The study includes the analysis of single, dual and triple-mode filters together with an investigation of the coupling behavior of synchronously and asynchronously tuned resonators. This study identified the main properties responsible for frequency and bandwidth control in a filter, and consequently systematically created innovative design techniques.

The research also deals with the development of synthesis procedures for filters with advanced asymmetrical responses. The main goal of this effort is the creation of planar reconfigurable filters with arbitrary assigned transmission zeros. These advanced realizations require meeting complex design specifications of advanced systems in both commercial and military applications. This work involves an in-depth investigation of polynomial synthesis methods for filters with crossed-coupled resonators and fully canonical form realizations using topologies with source and load coupling.

CHAPTER 1

INTRODUCTION

Some of the most fundamental applications in microwave engineering are communications and radar. Since the conception of radio waves by Maxwell (1864), the evolution of electromagnetic systems continues to have many implications in basic human interactions. Although the essential functionality of communications and radars is different, these two applications share many electromagnetic phenomena. Development of both communication systems and radars begin with milestones dating back to the pioneering work in early radio transmission of Hertz (1887) and Marconi (1901). The transmission of intelligence bearing signals through distinct media channels transformed our way of sharing information. Modern communication systems and today's reliance on radio propagation facilitates mobility, a great value in today's society.

Early radar systems were developed as a military tool for ranging, navigation, guidance, and detection. Today, radars enjoy a growing range of applications in everyday activities. Some common applications include police traffic radars, air traffic control, meteorological radars, and collision avoidance in both aviation and the automobile industry. Another use of modern radars is electromagnetic imaging, an application that allows the mapping of three-dimensional areas without ideal weather conditions or light.

Communication and radar systems deal with the analog and digital processing of high frequency signals. Communication systems concentrate on the modulation techniques to transmit and receive intelligence-carrying signals. Radars use electromagnetic processing to detect the echoes produced by their own transmitted pulses. With this information, they form a complete picture of object detection, range and velocity. Recently, the combination of these fundamental tasks encompasses complex applications, where detection and range in a radar and transmission of modulated signals use the same channel. This concept being implemented for the interrogation and sensing of electronic tags also expands to a new

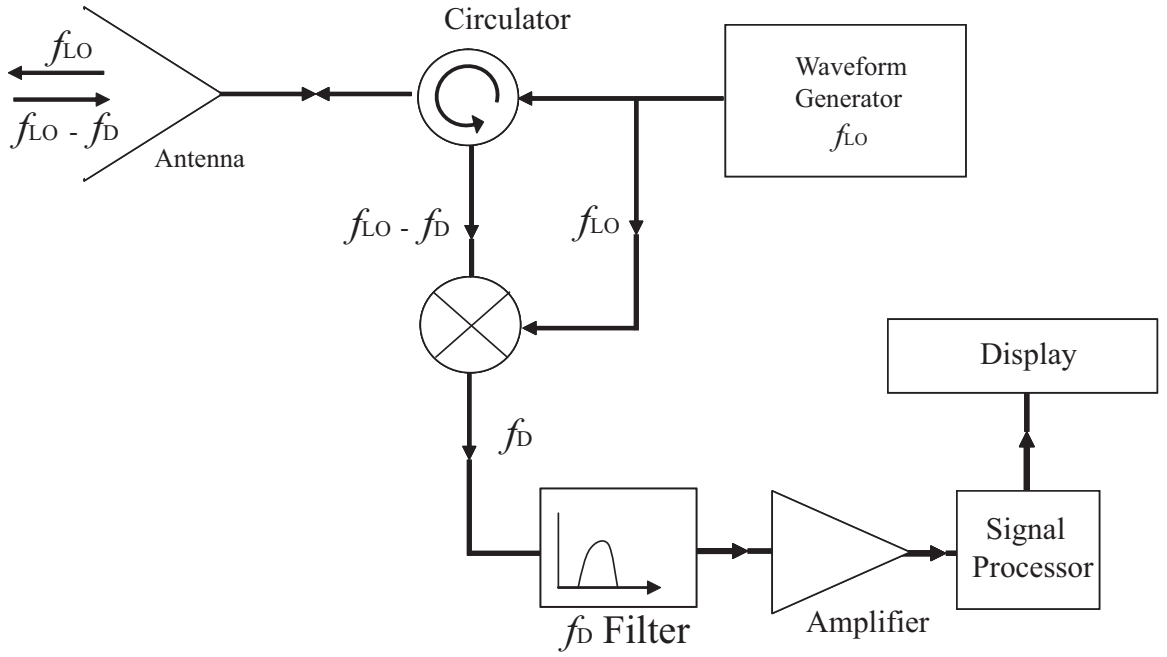


Figure 1. Simplified schematic of a doppler radar.

range of multifunctional applications.

In recent years, evolving communication technology has increased the demand for components with multi-band and multi-functionality. For this reason, it becomes essential for RF front-end electronics to support multiple information channels. In order to achieve a level of multi-band and multifunctional capabilities, it is necessary to increase the number of electronic configurations a specific circuit has. Reconfigurable filters are modern RF components designed with a multifunctional frequency behavior. These filters need to meet superior requirements in dynamic range, insertion loss, and distortion, while also maintaining realizable low cost and compact size topologies.

Fig. 1 shows the schematic of a simplified doppler radar. Doppler radars are used to determine the velocity of moving objects. In this example, the initial radar pulses are radiated by the antenna at a frequency of f_{LO} . The doppler shift phenomenon simply states that the returning pulse, after bouncing off a moving object, will incur in a frequency shift proportional to the object's velocity. For this reason, the returning signal will have a frequency of $f_{LO} \pm f_D$. This pulse is then down converted by the mixer to isolate f_D , the

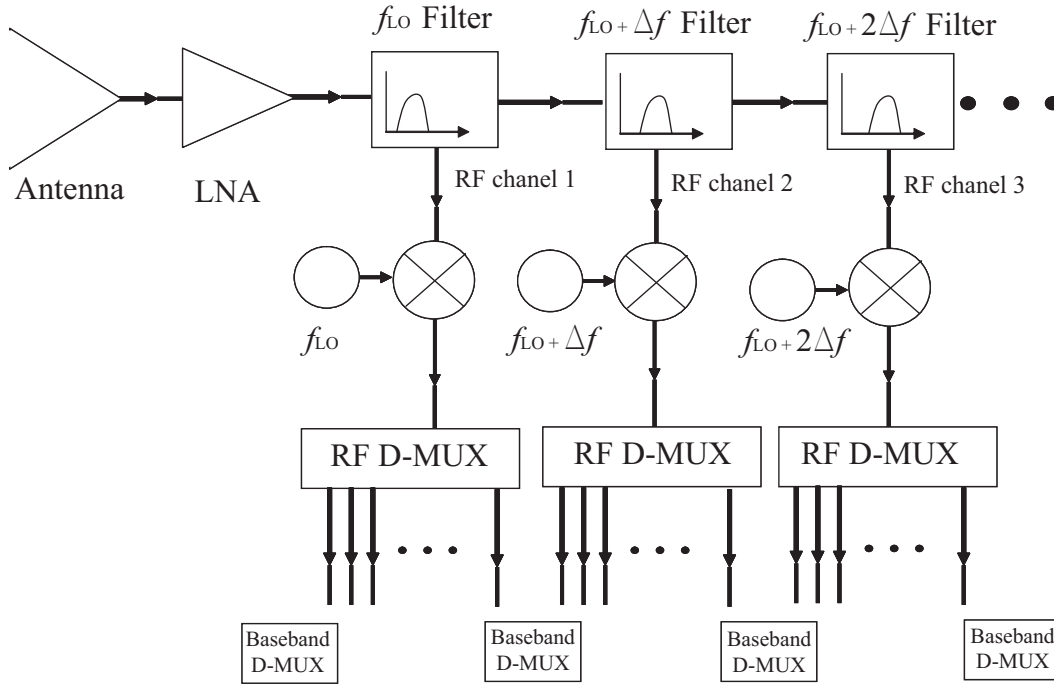


Figure 2. Simplified schematic of a frequency division multiplexed microwave radio receiver.

frequency shift associated with a specific object velocity. The filter following the mixer is required to select the minimum and maximum expected target velocities. This eliminates the clutter produced by static objects such as trees and ground. A multi-functional system implemented here may allow this radar to adapt its function to different situations. For example, at one instance the radar may be used at higher frequencies for the detection of flying objects, while in a different occasion it may be tuned to detect slower land moving vehicles. Doppler radars are systems with different transmitter and receiver frequencies. The function of the circulator may sometimes be exercised by a duplexer. A duplexer is a set of bandpass filters that share a common port. This common port is connected to the antenna while the remaining ports, required to have a level of isolation, are dedicated to the transmitter and receiver circuits.

Fig. 2 shows the receiver schematic of a frequency division multiplexed microwave radio. In this situation, a series of dropping filters individually select a channel from the received spectrum. This allows the effective use of broad-band communication signals at

microwave frequencies. Each channel is down-converted and then D-multiplexed together until the original signals are reconstructed at baseband. This illustrates some of the simplest tasks performed by selective filters in radars and communication systems.

Reconfigurable filters are classified by their functionality. The most common filters are tuned in frequency to achieve multi-band selection. Other filters adjust their fractional bandwidth to eliminate out-of-band noise components. The following criteria may be used to determine the performance of tunable filters: 1) Tuning range-defined as the difference between the lowest and highest center frequency achievable within acceptable limits of response degradation. 2) Tuning efficiency-this can be written as

$$\eta = \frac{f_2 - f_1}{X_2 - X_1} \quad (1)$$

where f_2 and f_1 are the center frequencies produced by the variables enforcing the tuning X_2 and X_1 , respectively. 3) Tuning speed-defined as necessary time to change the filter response from one state to the next. The states can be determined by a frequency shift or bandwidth. 4) Tuning linearity-the maximum deviation of the center frequency or fractional bandwidth versus the value of variable reactance producing the tuning. This can be a current, a voltage or a geometrical variation.

In both military and commercial platforms, design specifications can be asymmetrical in nature, where different sets of requirements exist on either side of the pass-band. Some applications additionally entail responses with incompatible selectivity and in-band group delay flatness, suggesting the need for more advanced structures.

This work presents a comprehensive study of the behavior of microwave resonators in single-mode and dual-mode operation. This investigation results in the creation of design techniques for microwave bandpass filters capable of tuning to different frequency bands, as well as varying their fractional bandwidth. The research also investigates advanced polynomial synthesis methods to create filters with prescribed transmission zeros. Filters that result from polynomial synthesis methods are able to meet most specifications, especially

in regards to response symmetry and in-band group delay flatness. The creation of filters capable of producing advanced frequency responses requires cross-coupled resonator topologies, and their physical implementation is mostly limited to waveguide technology. This analysis uses polynomial synthesis procedures to create reconfigurable planar filters with advanced asymmetrical responses.

CHAPTER 2

BACKGROUND

Up to date, most of the existent work in reconfigurable planar filters encompasses a proof-of-concept character. In recent years, the derivation of filters with tunable characteristics gained considerable attention since they provide potential solutions to many commercial and military applications. A modern trend in high frequency systems is the multi-band/multi-functional philosophy, which employs broadband receiver bandwidths that can simultaneously support multiple information channels. A pre-selective filter capable of tuning to different frequency bands, as well as varying its fractional bandwidth, accomplishes this versatile frequency behavior. A bandpass filter may be used to retain the desired signals within a predetermined frequency band of interest, while suppressing noise contributions and interference from outside the band. Reconfigurable filters produce more than one desired response in a controllable manner. Such filters can be classified by their frequency behaviors and applications. For example, filters with tunable center frequency are intended for multi-band selectivity, while filters capable of adapting their fractional bandwidth are essential to eliminate out-of-band noise and jamming spectral components.

The presentation of some of the first electronically tuned filters at microwave frequencies occurred during the late 1950's. In 1958, De Grassel [1] revealed that single-crystal yttrium iron garnet (YIG) behaves at microwave frequencies, much like a low-loss cavity resonator. Changing the applied DC magnetic field tunes the YIG resonator, which enables its use as an electronically tuned filter. In 1960, Carter [2] created tuned filters with more than one resonator by placing YIG spheres between overlapping waveguide or coaxial line structures. YIG tunable filters were extensively studied during the 1960s and early 1970s [2, 4].

Mechanically tuned waveguide filters were designed in the early 1960s. In this case,

varying the dimensions of the waveguide walls using tuning screws achieves tunability [5-7]. Other designs included the use of dipole resonances produced by a plasma discharge current. In this approach, the center frequency of the filter is varied. Several mechanically tuned filters were designed based on dielectric filled resonators in the 1970s. In such examples, a tuning screw that varies the air gap moves the dielectric filled resonators inside the waveguide walls. [10, 11]

In the 1970s and 1980s, the reconfigurable filter picture showed little novelty of some waveguide filters that used varactor diodes to vary the coupling between metal posts inside a waveguide [12]. This period produced variations of existing YIG, mechanical, and plasma filters that mostly concentrated in high power applications using structures such as waveguides, dielectric filled resonators, and coaxial line filters [13-16]. These structures are large, occupying up to several inches in all three dimensions.

Planar tunable filters using strip and microstrip configurations were of increasing interest in the 1980s. The majority of the early designs include strip configurations [17] and combline topologies [18, 19]. Varactor diodes were extensively used in this period to produce filters with continuous tuning. Other planar filters in the late 1990s utilized ohmic contact MEMS switches to achieve tunability in a discrete fashion.

Dual-mode resonators were first introduced around 1974 mostly using rectangular waveguides with perturbation screws inserted in the corner of the resonant cavities [25, 26]. In 1980, Cameron and Rhodes [27] derived more complete design guidelines for waveguides with asymmetrical configurations using dual-mode resonators. Some dual-mode dielectric filled resonators were introduced around 1982 [28] and several variations through out the years have been proposed [29, 30].

Curtis [31] introduced the first dual-mode resonator in planar form in 1981. His work introduced the fundamentals of microstrip dual-mode resonators of square and circular

shaped patches. Hong then presented the theory of microstrip square loop [32] and multilayer [33] dual-mode resonators for the creation of filters with more advanced characteristics. Several variations of these basic dual-mode filters have been presented through out the years [34, 35]. Hong [36] also introduced the triangular patch dual-mode resonator in 2003. However, this thesis presents for the first time reconfigurable filters based on dual-mode resonators.

Lastoria [52] reported triple-mode filters in 1998. Dielectric filled structures inside a resonant metal cavity make the triple mode resonance possible. This cavity is then perturbed using tuning and coupling elements, such as screws or metal rods. Chua [53] introduced a similar method in 2003. As mentioned before, dual-mode filters were successfully translated from waveguide to planar technology and have been available for years. Triple-mode filters, however, have not been presented in planar form prior to the work in this thesis.

Classical filter topologies, such as those based on capacitive coupled resonators, are capable of producing N transmission poles and $N-2$ finite frequency transmission zeros, where N is the filter order. Recent years have seen the development of several polynomial synthesis techniques, where topologies with cross-coupled resonators including input and output coupling have been used to design filters with prescribed transmission zeros. One great advantage of such techniques is the realization of fully canonical filter functions, where the limitation in possible transmission zeros is increased to N . Given that the transmission zeros can be prescribed anywhere in the complex s -plane, filter responses of any desired frequency characteristics are consequently possible. The global result of the filter synthesis is a coupling matrix that reveals the coupling coefficient between resonators and input/output ports. This design procedure was implemented using waveguide filters. The transition to planar circuit technology, such as microstrip or coplanar waveguide (CPW), is currently in its early stages.

Saito [37] first presented the polynomial synthesis method that resulted in a coupling

matrix in 1969. His approach required an unnecessarily large number of coupling elements raising inconveniences for the production of the filter. Rhodes' [38] unique approach reduces the number of couplings in order to form a realizable topology. In 1971 [39] and 1972 [40], Atia presented work on the design of waveguide filters using polynomial synthesis techniques that included cross-coupled resonators. These techniques have been refined through out the 1980s and 1990s [41-46].

Cameron and Amari developed two major techniques for the synthesis of filters with arbitrarily assigned transmission zeros. Cameron posited the general theory of a coupling matrix synthesis, and he proposed the application of a series of similarity transformations to a generic coupling matrix. This technique produced popular waveguide topologies, such as the folded form and cul-de-sac. Cameron's theory was first applied to filters with cross-coupled resonators [47] in 1999. The advanced synthesis technique that includes input and output coupling for canonical filter functions [48] was finally presented in 2003.

Amari proposed a different treatment of the coupling matrix synthesis by means of an optimization gradient. In his approach, topology constraints are included in the computation forcing the final coupling matrix to take the form of a predetermined topology. Amari introduced his optimization gradient technique in 1999 for cross-coupled resonator filters [49], and followed in 2002 with the comprehensive technique including input and output couplings [50]. Up to date, polynomial and coupling matrix synthesis has been applied mostly to waveguide and dielectric filled resonator structures. In 2001, Hong [51] presented the first planar technology realization of filters using cross-coupled resonators and/or input/output couplings. His work underlines the basic procedure to obtain electric and magnetic couplings between two microstrip open loop resonators. Tunable filters directly derived from these techniques have not been demonstrated today. Technological advancement has yet to produce tunable filters directly derived from these techniques.

CHAPTER 3

FRACTIONAL BANDWIDTH VARIATION TECHNIQUES

The study of microwave resonators with single and dual-mode characteristics, as well as their synchronously and asynchronously tuned configurations, has lead to the derivation of several bandpass filters with center frequency and bandwidth control. This section introduces a design methodology consisting of a coupling variation and length compensation technique. This technique is developed for filters seeking adaptable bandwidth tuning in a discrete manner. This chapter will also present tunable schemes to produce filter configurations with simultaneous control of bandwidth and center frequency. The remaining chapters will discuss the development of dual-mode topologies with asymmetrical characteristics, filters using ferroelectric materials and MEMS switches, and hybrid waveguide/multi-layer design synth

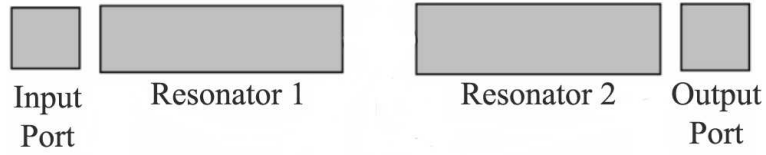


Figure 3. Conventional second order admittance inverter microstrip filter.

3.1 Coupling Variation and Length Compensation

The starting point for this research is an investigation of some important properties of classical microstrip filter topologies. Classical or conventional Nth order microstrip filters consists of N capacitive coupled resonators, where the coupling exists only between adjacent resonators and only the first and last resonator is coupled to the input and output port respectively. The simplicity of these topologies is ideal to identify some of the main properties that lead to a reconfigurable solution. Fig. 3 shows a second order admittance inverter filter. In this section, this topology will be used to derive some basic tunable functions.

As stated in chapter 2, little to no effort has been dedicated to derive filters with a variable fractional bandwidth. Hence, the effort is first focused in finding a solution for fractional bandwidth control. The reactance elements of main interest in a classical filter configuration are the input/output port couplings and the inter-resonator couplings. By definition [52], the admittance inverter filter is synchronously tuned as both resonators are identical in shape and size producing self resonant frequencies that are also identical. The location of the final resonant frequencies f_1 and f_2 is determined by the coupling strength that exists between both equal size resonators. The coupling factor k for synchronously tuned resonators [52] is given by

$$k = \frac{f_2^2 - f_1^2}{f_2^2 + f_1^2} \quad (2)$$

The coupling factor k is directly related to the spectrum range $f_2^2 - f_1^2$; it can be argued that the larger the spectral separation of the resonant frequencies f_1 and f_2 , the larger the pass-band width. From this discussion it follows that in order to achieve fractional bandwidth control, single-mode filter topologies with synchronously tuned resonators, require a reconfigurable scheme that allows the inter-resonator coupling factor k to vary in a controlled fashion. Moreover, bandwidth control can only be claimed if all resulting responses have different fractional bandwidths but the same center frequency f_0 . Keeping a fixed center frequency is one of the major obstacles in the creation of a bandwidth variable filter. The difficulty exists because the tunable reactant elements need to be introduced without perturbing the effective size of the resonators. The self-resonant frequencies are determined by the resonators effective lengths. For filter configurations with more than one resonator, the effective length inversely affects the filter's center frequency.

The last parameter to be discussed is the input/output coupling of the filter. It is seen that this coupling has a direct effect on the external resonator quality factor Q_e . From conventional design methodologies such as the insertion loss method, it follows that for every fractional bandwidth there exists a single coupling configuration that allows an optimal

pass-band flatness and roll-over rejection. This is particularly true for chebychev filtering functions such as those produced by classical topologies. This optimal condition is called critical coupling. While stronger or over coupling at the input/output ports may produce an acceptable in-band response with a flat characteristic, a decreased roll-off slope causes the filter to become less selective. On the other hand, higher roll-off can be accomplished with under-coupled input/output ports with the cost of an oversized passband ripple.

A tunable scheme requires the consideration of all the above mentioned factors. First, a variable reactant element is required to manipulate the coupling strength between adjacent resonators. Second, the effective length of the resonators needs to be kept constant in order to maintain a fixed center frequency. Finally, the coupling strength at the input/output ports needs to provide an acceptable response for all different configurations. The latter can be accomplished by varying the input/output coupling in such a way as to critically couple every response. However, acceptable responses may be accomplished with a fixed input/output coupling, producing a significant simplification in the tuning circuitry.

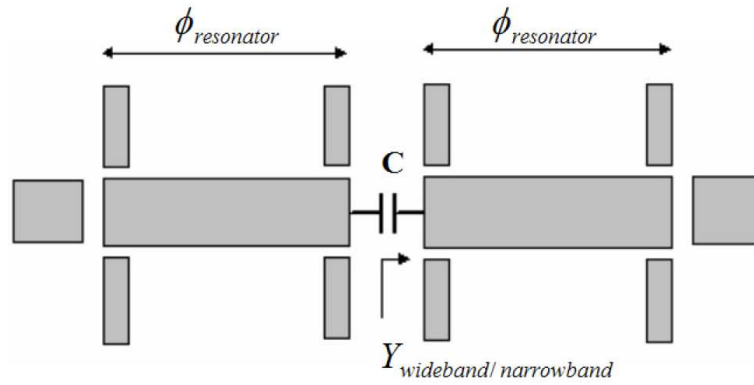


Figure 4. Second order filter with added tuning stubs for bandwidth tuning.

3.2 Reconfigurable Filter Design with Bandwidth Control at 5.8 GHz

The following filter is designed with a variable pass-band ratio of 2:1 and a fixed center frequency of $f_0 = 5.8$ GHz. The tuning mechanism is achieved discretely by p-i-n diode switches that directly manipulate the geometry of the filter in a controlled manner. Fig.4.

shows a second order filter designed for bandwidth variation. A set of eight tuning stubs have been added to both top and bottom producing a symmetrical design about a central horizontal line. The inner four stubs are placed along the inter-resonator coupling gap. These stubs vary the amount of coupling interaction between adjacent resonators. When the inner stubs are connected, the resonator coupling increases, causing the resonant frequencies f_1 and f_2 to move away from each other. This configuration results in the wideband state of the filter. When these stubs are disconnected, the resonant frequencies f_1 and f_2 are located at a closer spectral proximity resulting in the narrowband state. Moreover, disconnecting the inner stubs also causes the resonators to suffer a reduction in effective length. The outer four stubs are connected to compensate for the lost effective length and avoid a shift in center frequency. Formulas for the synthesis of a conventional admittance inverter filter of order $N=2$ are presented in [53]. The calculation of the inverter constant J , coupling susceptance B and coupling capacitance C between resonators is given by:

$$J = \frac{Y_0 \pi \Delta}{2 \sqrt{g_1 g_2}} \quad (3)$$

$$B = \frac{J}{1 - Z_0 J} \quad (4)$$

$$C = \frac{B}{2\pi f_0} \quad (5)$$

where Y_0 is the admittance related to the resonator's width, in a conventional design this is Z_0^{-1} , g_1 and g_2 are the element constants for a two pole filter prototype and Δ is the desired fractional bandwidth. Based on equations (1) and (2), equation (3) can be expressed as:

$$C = \frac{Y_0 \Delta \sqrt{g_1 g_2}}{f_0 (4 g_1 g_2 - \pi^2 \Delta^2)} \quad (6)$$

When the stubs at the inner gap are introduced the effective admittance at the edge of the resonator is modified. In order to reflect this, $Y_{\text{narrowband}}$ and Y_{wideband} represent the effective admittance added by the stubs in each state. The capacitance values associated with the

gap between resonators at both filter states (wideband and narrowband) can be determined when Y_0 is replaced by the respective admittances of each state. The resulting capacitance values now become:

$$C_{wideband} = \frac{Y_{narrowband} \Delta \sqrt{g_1 g_2}}{f_0 (4 g_1 g_2 - \pi^2 \Delta^2)} \quad (7)$$

$$C_{narrowband} = \frac{Y_{narrowband} \Delta \sqrt{g_1 g_2}}{f_0 (4 g_1 g_2 - \pi^2 \Delta^2)} \quad (8)$$

The resonator's electric length $\phi_{resonator}$ is determined by the following equations:

$$\phi_{resonator} = \pi + \frac{\theta_{inner-gap}}{2} + \frac{\theta_{outter-gap}}{2} \quad (9)$$

$$\theta_{outter-gap} = -\tan^{-1} \left(\sqrt{\frac{8\pi g_1}{2 g_1 - \pi \Delta}} \right) \quad (10)$$

$$\theta_{inner-gap} = -\tan^{-1} \left(\frac{\pi \Delta}{\sqrt{g_1 g_2}} \frac{4 g_1 g_2}{4 g_1 g_2 - \pi^2 \Delta^2} \right) \quad (11)$$

where $\theta_{inner-gap}$ and $\theta_{outter-gap}$ are the negative lengths that result from the admittance inversion at the transmission line discontinuities. The bandwidth is therefore tuned by the direct relation between the resonator edge admittances and the coupling strength. Since $Y_{wideband} > Y_{narrowband} > Y_0$ the coupling strength is directly affected depending on the size of the extended stubs at the inner gaps. On the other hand, the center frequency is kept constant when the parameters $\theta_{inner-gap}$ and $\theta_{outter-gap}$ are kept equal in effective length by the addition of the outer stubs.

The electronic switching was realized using MCE/ Metelics mesa beam lead p-i-n diodes. The S-parameters of the p-i-n diodes were first measured in both forward and reverse bias states. Lumped element models were created in order to match the S-parameters and simulate the effect of the p-i-n diodes on the topology. The forward or ON state of the diode from 3 to 8 GHz was equivalent to a 6 Ω resistor and produced an average insertion

loss of 0.51 dB. The reverse biased diode had an insertion loss of about 10 dB at the center frequency and the matching lumped element circuit consisted of a 0.1 pF capacitor.

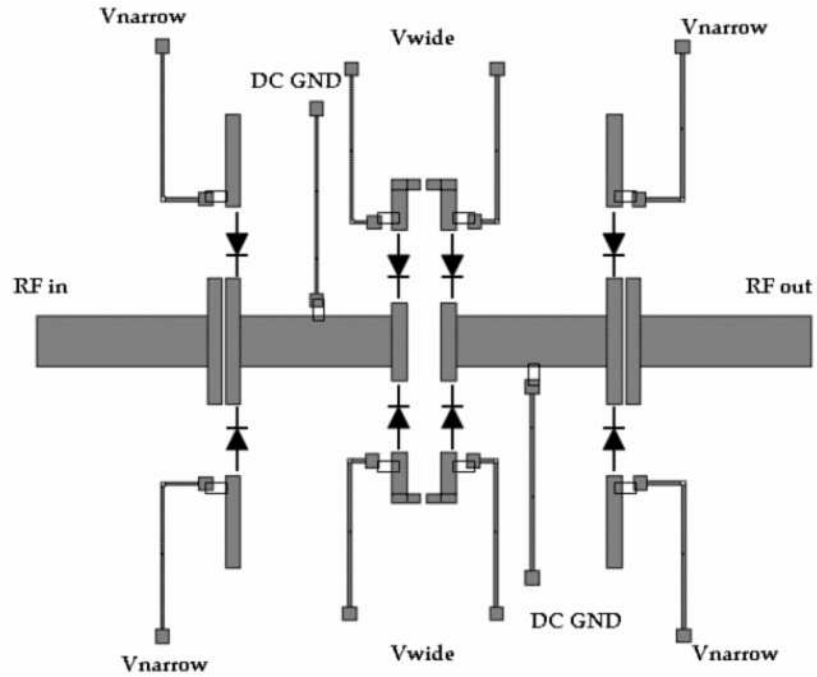


Figure 5. Layout of tunable filter with bias lines.

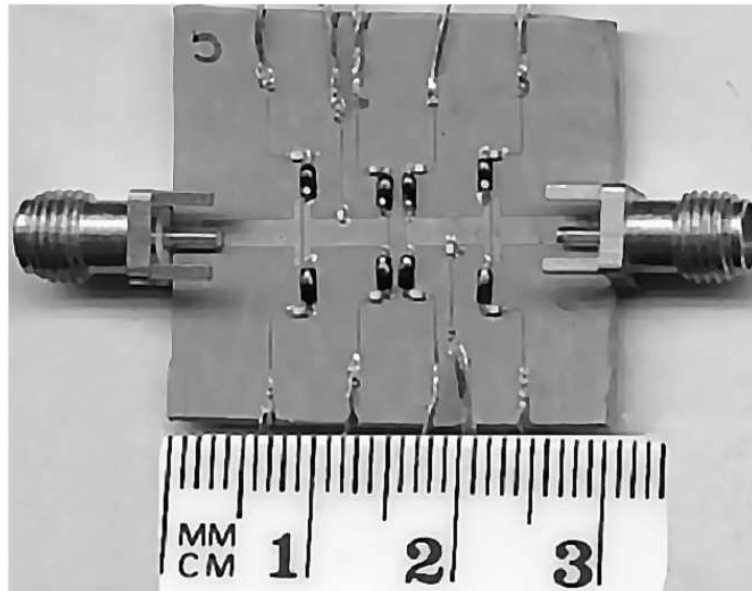


Figure 6. Picture of fabricated filter.

Fig. 5 shows the reconfigurable filter layout including bias lines. The bias network

consisted of a limiting resistor in series with the DC lines and a TDK inductor with self resonance frequency of 5.7 GHz and a nominal value of 5.7 nH. These inductors were used as RF chokes to minimize signal leakage. The DC lines were strategically placed to maintain the symmetry of the design. The current to each diode was limited to 20 mA in the forward bias state and the applied voltage was -10 V in the reverse bias state. The filter topology requires four forward biased diodes and four reversed biased diodes at all times to create the different passband configurations and avoid signal clipping.

The substrate used in this design was Rogers Duroid, with a dielectric constant of $\epsilon_r = 6.15$, $\tan\delta = 0.025$, substrate thickness of 1.25 mm with 0.5 OZ of copper metallization. The diodes used were mesa beam lead MBP-1034-B11 and the inductors were MLS 1005 by TDK. The layout including the DC bias lines, was fabricated using standard photolithography techniques. The connectors, inductors and the p-i-n diodes were fixed to the board using silver epoxy. A picture of the fabricated filter is shown in Fig.6.

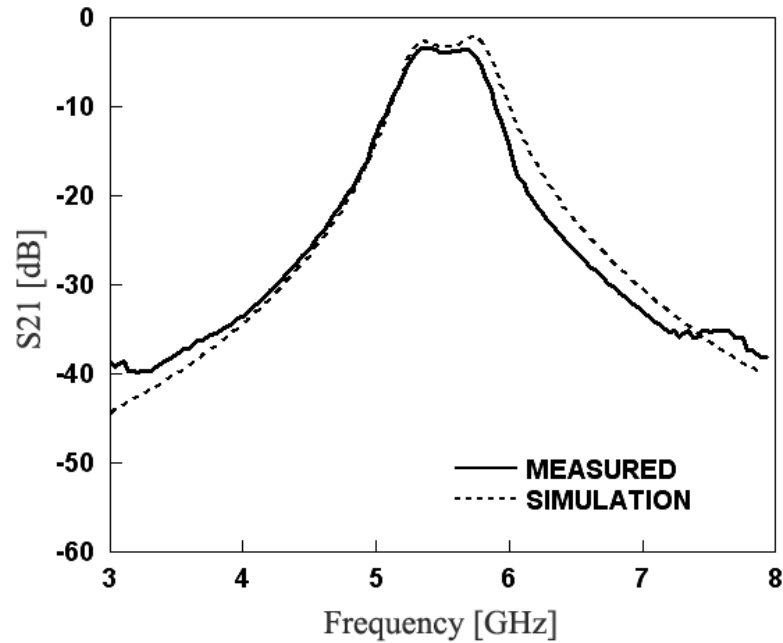


Figure 7. Measured and simulated S21 parameters of wideband state.

The S parameters of the filter in the wideband and narrowband states are shown in Fig. 7 through Fig 10. The microstrip topology was optimized using the software Agilent

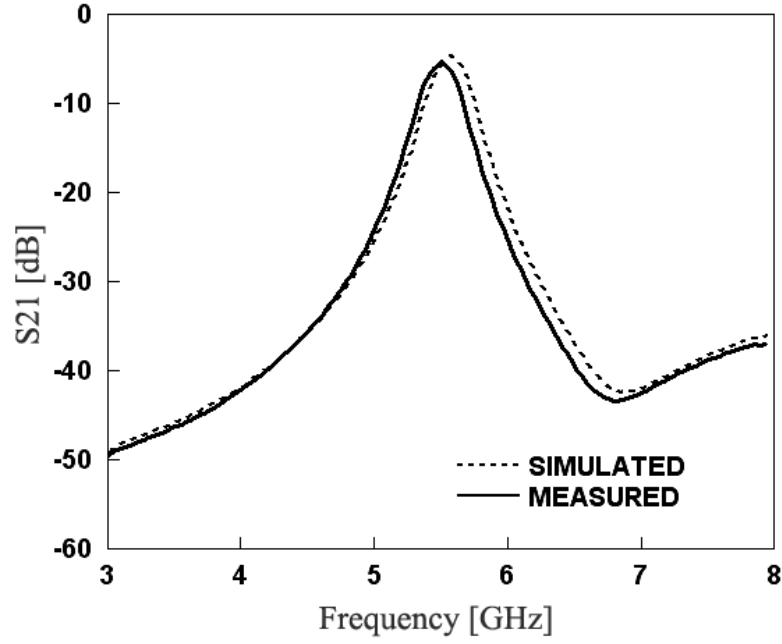


Figure 8. Measured and simulated S21 parameters of Narrowband state.

Momentum. The measured insertion loss of the filter in the wideband state was 3.95 dB, and the 20 dB attenuation points at the side bands were located at 4.95 GHz and 6.21 GHz. The narrowband configuration of the filter had an insertion loss of 4.73dB. The 20 dB attenuation points for the narrowband state were located at 5.29 GHz and 5.94 GHz. Also, the S-parameter measurements of the single diode resulted in an insertion loss of 0.51 dB. Given that 4 diodes are in the forward bias state on any given configuration, approximately 2dB of loss is caused by the diodes. Better insertion loss may be achieved by diodes with lower ON resistance than the present 6 Ω . The fractional bandwidth achieved at the wideband state was 10.12 %, while the bandwidth at the narrowband state was 5.43 %. This resulted in a 1 : 1.86 pass-band ratio.

Due to the nonlinearity of the p-i-n diodes it is important to measure the amount of signal distortion. Using a standard two-tone method [54], the intermodulation of the filter was measured around the center frequency of the filter f_0 . The intermodulation setup is shown in Fig. 11. First, two signals with frequencies $f_1 = f_0 - \Delta f/2$ and $f_2 = f_0 + \Delta f/2$ where combined with a coupler and kept at the same power levels. The signals frequency

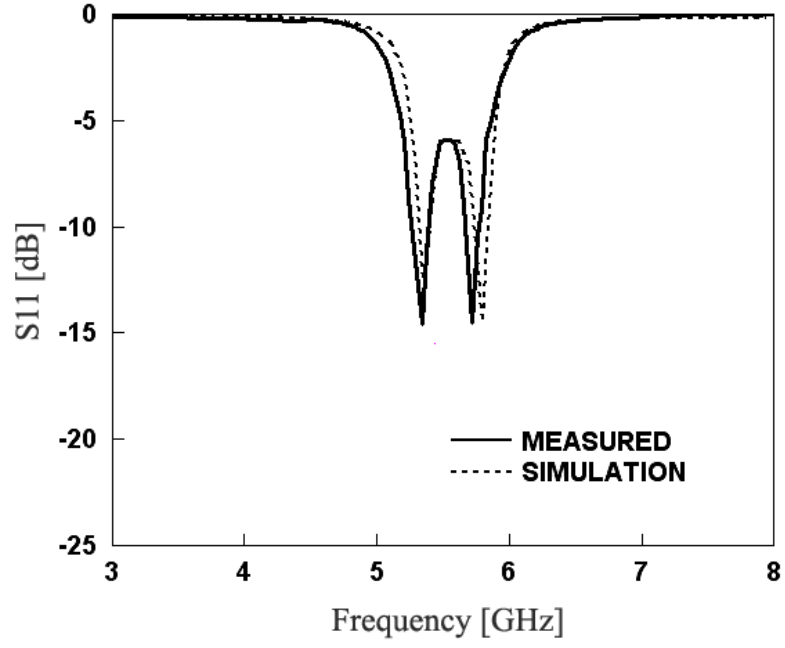


Figure 9. Measured and simulated S11 parameters of wideband state.

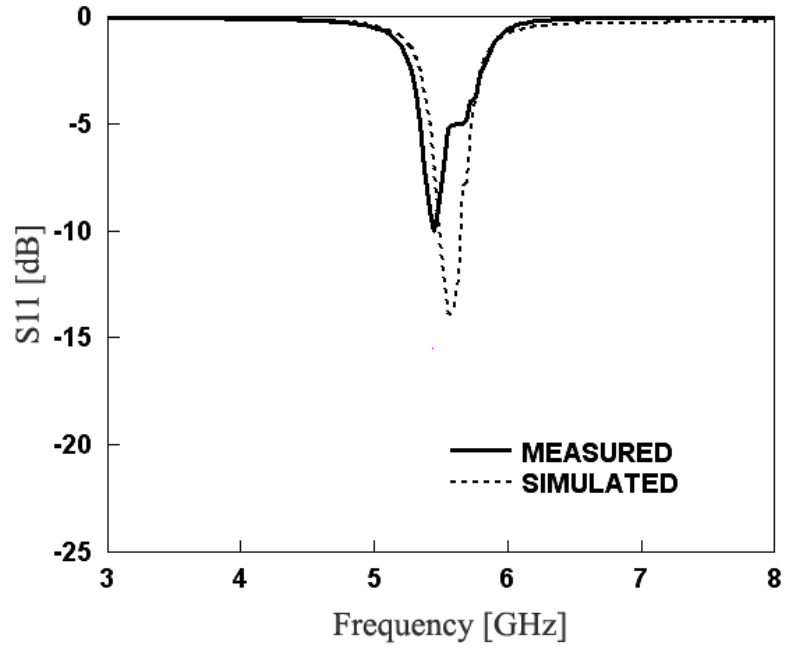


Figure 10. Measured and simulated S11 parameters of narrowband state.

separation was varied by amounts of $\Delta f = 50, 100, 200, 400, 600,$ and 1000 kHz. These two signals were then delivered to the input of the filter with power levels of $7.5, 5$ and 0 dBm. In this setup, the intermodulation products are observed at the output spectrum of the filter and can be found at the frequencies $f_1 - \Delta f$ and $f_2 + \Delta f$. The intermodulation components

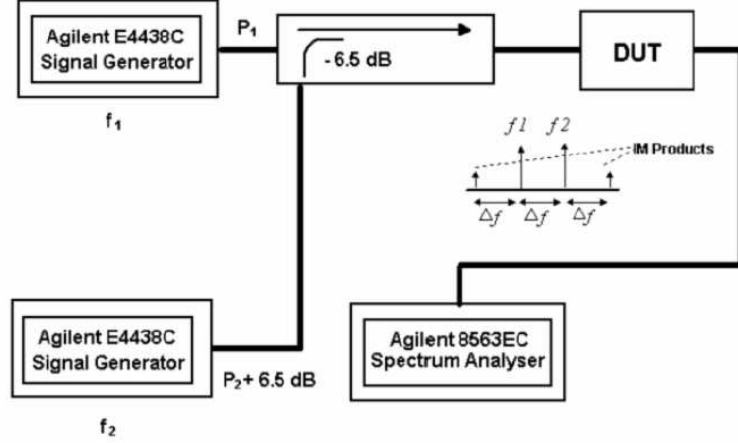


Figure 11. Intermodulation measurement setup.

were then translated to third-order intermodulation intercept points (IIP3). The narrowband produced an IIP3 greater than +43 dBm for $\Delta f = 1\text{ MHz}$ and an IIP3 greater than +25 dBm for $\Delta f = 50\text{ kHz}$. The wideband configuration resulted on slightly higher intercept points. For $\Delta f = 1\text{ MHz}$ the IIP3 was greater than +52 dBm and for $\Delta f = 50\text{ kHz}$ the IIP3 was greater than +29 dBm. Similar results are found in other filters using p-i-n diodes, (for example the filter in [61] $\text{IIP3} > 46\text{ dBm}$ for $\Delta f = 1\text{ MHz}$). Filters using MEMS switches typically have better linearity in which case the third-order intermodulation intercept point is expected to be higher. However, the filter presented here results in no significant signal distortion.

3.3 Six State All Tunable X-Band Filter

Multi-functional RF sub-systems that are reconfigurable in frequency can be accomplished by a pre-selective filter. As shown in Fig. 12, This pre-selective filter can consequently feed a wide-bandwidth antenna or antennas with radiation pattern tunability. This section presents a comprehensive study of a reconfigurable filter intended for tunable RF systems. The filter produces simultaneous frequency and bandwidth control representing an important tool to meet modern system requirements.

The following design is a six-state tunable band-pass filter. The topology was able to

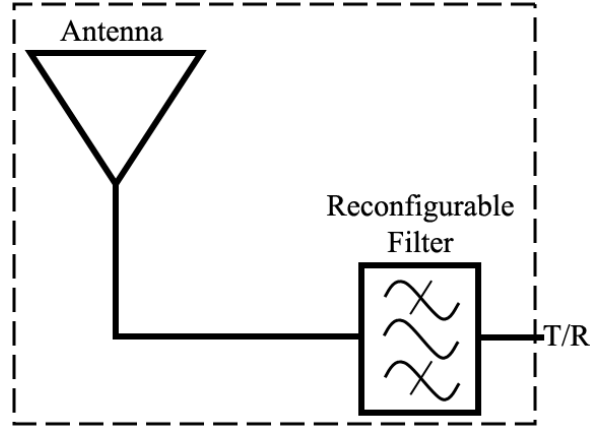


Figure 12. Antenna system with reconfigurable filter.

produce frequency responses of both narrowband and wideband characteristics with center frequencies of $f_0 = 9$ GHz, 10 GHz and 11 GHz. Simultaneous bandwidth and frequency control is successfully achieved by a tuning scheme that varies the coupling strength and effective length of the resonators. The resulting filter is also suitable for most commercial and military applications and represents a significant tool for reconfigurable communication systems allowing multiband selectivity and bandwidth control. As shown in the previous section, classical topologies based on single-mode resonators exhibit a dependency between bandwidth variation and frequency shifting. This represents a major obstacle in the efforts to design a filter with simultaneous frequency and bandwidth tuning. The design presented here, achieves independent bandwidth and center frequency control in a discrete manner using p-i-n diodes to connect or isolate specific filter sections. The filter produces two bandwidth configurations located at three different center frequencies for a total of six responses.

In general, bandwidth control is accomplished by the creation of a variable coupling scheme. In the present case, this is achieved by varying the effective coupling section size allowing the interaction between resonators to change. The center frequency is simply controlled by the resonator's effective length. The proposed filter topology is shown in Fig. 13. The tunable properties of the filter were made possible by three different geometrical manipulations: coupling stubs denoted as t_1 , compensation stubs t_2 , and shifting stubs t_3

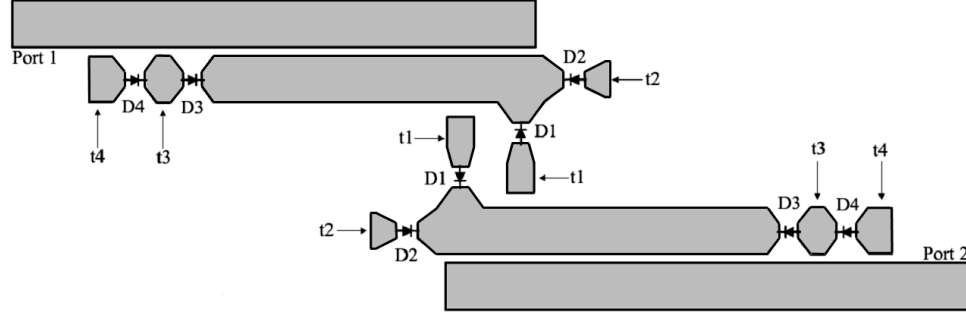


Figure 13. Proposed topology.

Table 1. Filter Responses Vs. Diode Biasing

Response Type	Center Frequency	D1	D2	D3	D4
Wideband	11 GHz	ON	OFF	OFF	OFF
Wideband	10 GHz	ON	OFF	ON	OFF
Wideband	9 GHz	ON	OFF	ON	ON
Narrowband	11 GHz	OFF	ON	OFF	OFF
Narrowband	10 GHz	OFF	ON	ON	OFF
Narrowband	9 GHz	OFF	ON	ON	ON

and $t4$. The topology was realized by making a simple modification to the conventional coupling scheme of a side-coupled resonator filter. First, the inter-resonator gap separation was increased and a 90° bend was added to the resonator ends. These bent sections, now $t1$, are in the vertical direction and allow for a larger variation range of the resonator coupling factor k . The coupling factor for synchronously tuned resonators [52] in terms of normalized split frequencies ω_1 and ω_2 is given by

$$k = \frac{\omega_2^2 - \omega_1^2}{\omega_2^2 + \omega_1^2} \quad (12)$$

Table 1 shows the six filter responses that result from the controlled biasing scheme of the diodes. The fractional bandwidth of the filter is controlled by the set of diodes D1 and D2. The wideband responses are produced when the diodes D1 are forward biased and D2 are reversed biased. The coupling stubs $t1$ are connected to the circuit reducing the relative distance between resonators and increasing the coupling factor k . When this strong

coupling between resonators is created, the separation of the resonant frequencies ω_1 and ω_2 results in fractional bandwidth ranging between 13.4 % and 14.7 %. The narrowband responses, on the other hand, are created when D2 is forward biased and D1 is reversed biased. In this situation, the stubs $t1$ are isolated creating a reduction in the effective length of the resonators. The stubs $t2$, now connected via diodes D2, are used to compensate for this effective length reduction. These length compensating stubs ($t2$) also cause a distance increase between resonators reducing their coupling strength. The narrowband configuration places ω_1 and ω_2 in a closer spectral proximity producing fractional bandwidths that range between 7.7 % and 8.5 %. The coupling scheme described here successfully achieves an approximate passband ratio of 1.73:1 at each of the desired center frequencies. The tuning stubs have been optimized with linear tapers to reduce signal transition loss around the diode connections.

The filter is designed to produce responses at the center frequencies of $f_0 = 9$ GHz, 10 GHz and 11 GHz. Center frequency control is achieved by the biasing configuration of the diodes D3 and D4. As shown in Table 1, responses with $f_0 = 11$ GHz are produced when both diodes D3 and D4 are reversed biased isolating the shifting stubs $t3$ and $t4$. Referring to Fig. 13, it is seen that this configuration results in the smallest resonator length of the design. Increasing the resonator length causes f_0 to shift to lower frequencies. Hence, responses with $f_0 = 10$ GHz are produced when the stubs $t3$ are connected via diodes D3. Responses with $f_0 = 9$ GHz are produced when both $t3$ and $t4$ are connected via diodes D3 and D4. In addition to frequency control, the shifting stubs ($t3$, $t4$) also play a fundamental role in the input-output (I/O) coupling of the filter. This I/O coupling has a direct effect on the external quality factor Q_e . In synchronously tuned resonators, inadequately high Q_e may cause an undesired large ripple at the passband formed between ω_1 and ω_2 [16]. With this in mind, the shifting stubs are realized by making the following manipulations to the conventional side-coupled resonator filter. First, the horizontal extension of the stubs $t3$ and $t4$ are set to produce the desired center frequency shifts. This mostly refers to the

size of t3 and t4 as they extend the resonator's effective length. In order to calculate the electrical lengths of these stubs, The guided wavelengths denoted $\lambda_0, \lambda_1, \lambda_2$ correspond to the center frequencies $f_0 = 11$ GHz, $f_1 = 10$ GHz, $f_2 = 9$ GHz. Equations (12) through (14) express these wavelengths in terms of the arbitrary chosen λ , which also corresponds to the highest frequency of operation $f_0 = 11$ GHz. Here, the wavelength scaling factor for each frequency is determined by the frequency ratios $r_1 = \frac{f_0}{f_1}$ and $r_2 = \frac{f_0}{f_2}$.

$$\lambda_0 = \lambda \quad (13)$$

$$\lambda_1 = r_1 \lambda \quad (14)$$

$$\lambda_2 = r_2 \lambda \quad (15)$$

The effective length of the half-wave resonator that constitute the image impedance filter can be expressed by equation (15) when $f_0 = 11$ GHz, (16) when the stub t3 is connected producing $f_1 = 10$ GHz, and (17) when both stubs t3 and t4 are connected to produce $f_2 = 9$ GHz.

$$\theta_0 = \frac{\lambda}{2} \quad (16)$$

$$\theta_1 = \frac{r_1}{2} \lambda = \theta_0 + \phi_3 \quad (17)$$

$$\theta_2 = \frac{r_2}{2} \lambda = \theta_1 + \phi_4 \quad (18)$$

The values ϕ_3 and ϕ_4 denote the electric lengths of stubs t3 and t4 and are expressed in terms of λ in equations (18) and (19), respectively. The procedure shown here is underlined for a three frequency state filter, however, the electric length calculation of shifting stubs for a higher number of frequency shifts can be completed by simply applying these equations recursively.

$$\phi_3 = \lambda \left(\frac{r_1 - 1}{2} \right) \quad (19)$$

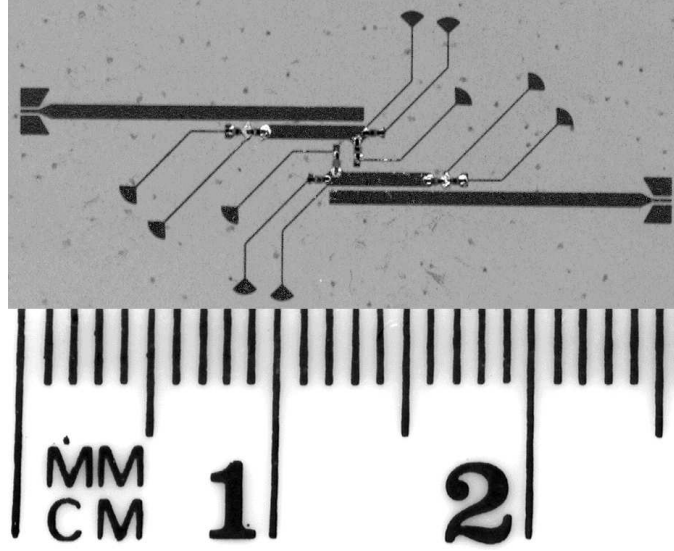


Figure 14. Picture of fabricated filter with diodes and bias lines.

Table 2. Measured Filter Characteristics

Response Type	Center Frequency	Insertion Loss	Bandwidth	Return Loss
Wideband	11 GHz	1.74 dB	1580 MHz 14.4 %	14.24 dB
Wideband	10 GHz	1.76 dB	1470 MHz 14.7 %	14.12 dB
Wideband	9 GHz	1.79 dB	1205 MHz 13.4 %	15.10 dB
Narrowband	11 GHz	1.84 dB	930 MHz 8.4 %	18.15 dB
Narrowband	10 GHz	1.87 dB	850 MHz 8.5 %	19.10 dB
Narrowband	9 GHz	1.92 dB	690 MHz 7.7 %	18.56 dB

$$\phi_4 = \lambda \left(\frac{r_2 - r_1 - 1}{2} \right) \quad (20)$$

The location of these stubs forces an increased interaction between the ports and the resonators. At this point, in order to avoid excessive I/O coupling, the stubs are designed with a narrower side located closer to the coupling sections. This I/O coupling scheme is set to produce flat passband responses in the wideband configurations. However, since the I/O coupling remains constant as the filter is switched between fractional bandwidths, the narrowband states exhibit a degree of overcoupling.

The substrate used in this design was Rogers Duroid, with a dielectric constant of $\epsilon_r = 10.2$, a substrate thickness of 25 mils, 0.5 OZ of copper metallization and $\tan\delta = 0.0025$.

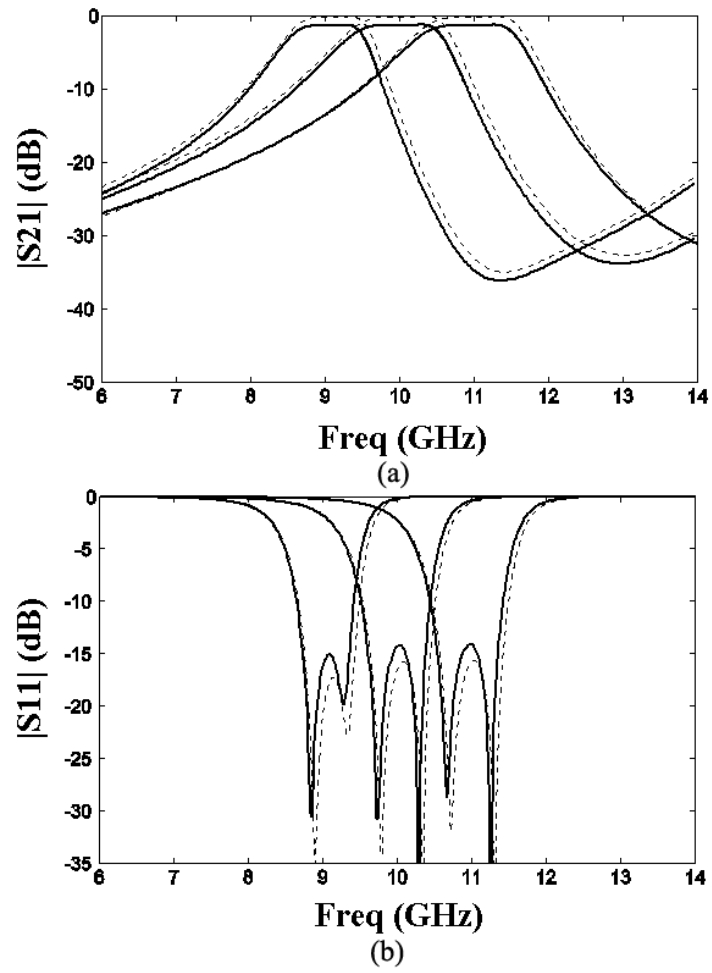


Figure 15. Wideband measurement results (solid line), simulated results (dashed line). (a) Transmission loss. (b) Return loss.

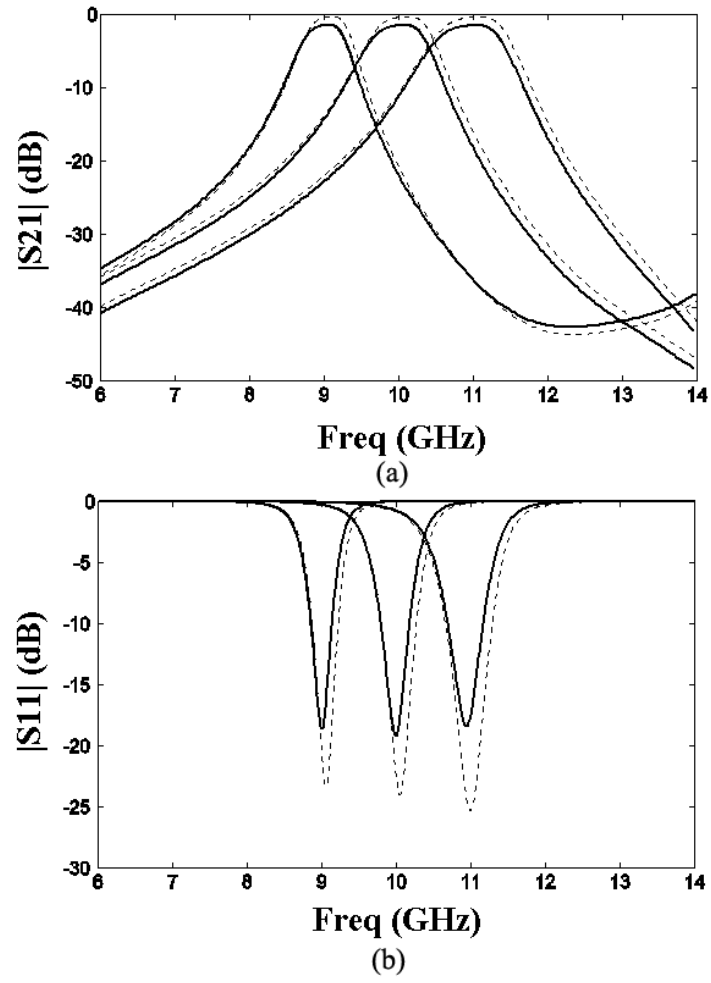


Figure 16. Narrowband measurement results (solid line), simulated results (dashed line). (a) Transmission loss (b) Return loss.

The diodes used were ASB 8000 by ASI. The filter was fabricated using standard photolithography techniques. The p-i-n diodes were fixed to the board using silver epoxy. A picture of the fabricated filter is shown in Fig.14. The effective filter size excluding the CPW to microstrip transitions, for on wafer probing, is about 15 mm x 15 mm. The DC bias lines are designed as RF chokes and consist of a high impedance transmission line terminated in an open radial stub, for a total effective length of $\lambda/2$. The biasing was realized using an Agilent 66000 power supply and single contact DC probes, placed at the center of the radial stubs. The forward bias current was limited to $I_f = 30$ mA and the reverse bias voltage was $V_r = -10$ V.

The simulated and measured transmission and return loss of the wideband and narrow-band states of the filter are shown in Fig.15 and Fig.16, respectively. The passband insertion loss IL , return loss RL and fractional bandwidth for all six responses are summarized in Table 2. The measured pass-band ratio between wideband and narrowband states was 1.75:1, 1.73:1 and 1.70:1 for $f_0 = 9$ GHz, 10 GHz and 11 GHz, respectively. As expected, the narrowband configurations have slightly higher insertion losses ranging from 1.84 dB to 1.92 dB. The wideband configurations resulted in insertion losses ranging between 1.74 dB and 1.79 dB. A very good agreement with respect to general frequency characteristics is observed between simulated and measured results. The discrepancy in insertion loss, however, is attributed to some simplifications included in the simulation procedure. The filter was simulated using the software Agilent Momentum. This full wave simulation was realized using a perfect conductor topology and incorporated the diodes as perfect short and open sections of transmission lines. During the filter design, these simplifications were included in order to expedite the simulation process. In all, six frequency responses involving six different structures had to be simulated with a sense of synchronization. The only allowed difference between these six structures is the location of the opens and shorts representing the diodes.

The fabricated structure was measured using a TRL calibration to exclude the loss from

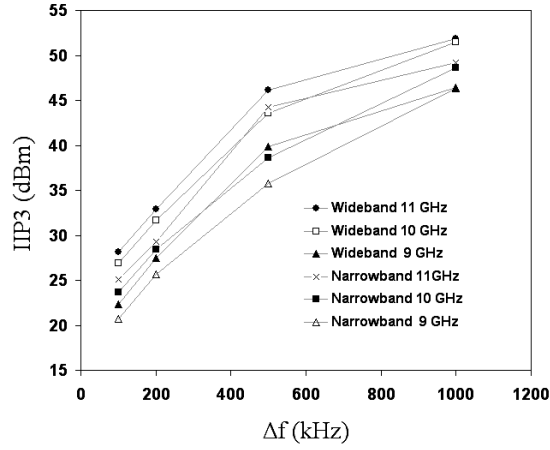


Figure 17. Measured intermodulation third order intercepts IIP3.

the RF probes. The p-i-n diode is characterized by a $3\ \Omega$ series resistance for the forward biased state and 0.025 pF capacitance for the isolation state. The diode loss increases slightly with frequency and it is approximately 0.24 dB at 10 GHz. Finally, the microstrip conductor loss is estimated by a simulation that includes the copper metallization information at 10 GHz. This simulation, not shown, exhibits 0.46 dB of passband loss. The diodes produce a combined loss of 0.96 dB at 10 GHz for a total calculated filter loss (diodes + conductor) ~ 1.42 dB. The average losses of the measured filter is 1.80 dB.

Signal distortion was investigated using a two-tone method. The intercept points vs. tone separation Δf are shown in Fig. 17. The 9 GHz narrowband response produced the lowest IIP3 of 21 dBm for $\Delta f = 100$ kHz and 48 dBm for $\Delta f = 1$ MHz. The 11 GHz wideband configuration resulted in the highest intercept points. For $\Delta f = 100$ kHz the IIP3 was greater than 27 dBm and for $\Delta f = 1$ MHz the IIP3 was greater than 52.9 dBm. As indicated by the intercept points, the intermodulation measurement results show that no significant signal distortion is added by the p-i-n diodes used.

The design of higher order filters may not be apparent using this technique. The question on the treatment of tunable intermediate resonators still remains. A solution may imply a series connection of tuning stubs. Fig. 18 shows an example of a third order filter layout for discussion purposes. The location of the three types of tuning stubs is provided as a

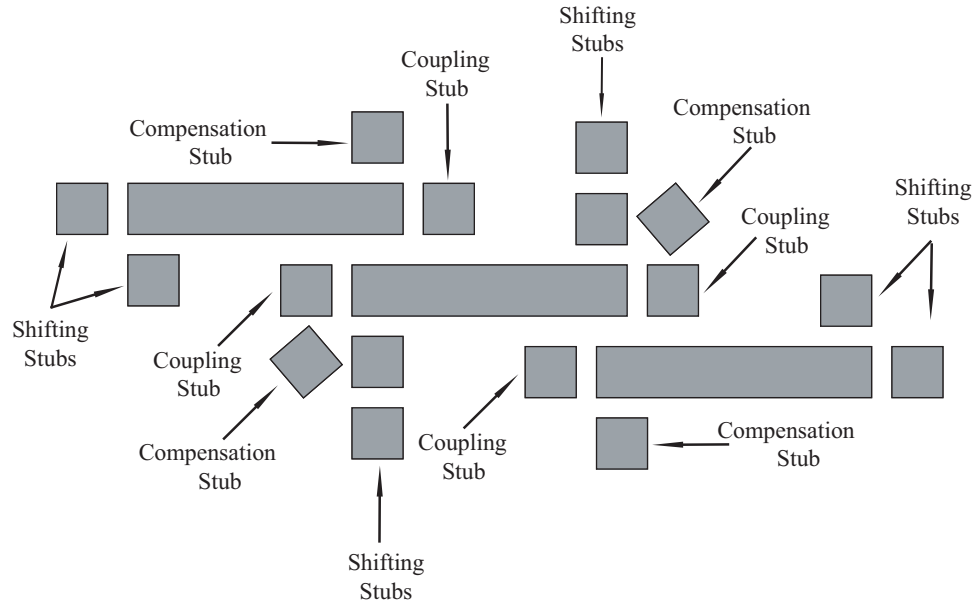


Figure 18. Conceptual treatment of intermediate resonators in higher order tunable filters.

way to generalize the design technique. As shown here, the intermediate resonator uses four shifting stubs, two coupling stubs and two compensation stubs to keep the symmetry. This is twice the number of tuning stubs needed for the outer resonators. Also, the coupling stubs in this example only extend in the horizontal direction. This may be enough to produce the desired passband ratio in higher order filters due to the additional number of poles. However, larger bandwidth variation can always be achieved by projecting the coupling stubs in the vertical direction as it was shown in the second order filter layout.

3.4 Chapter Summary

A reconfigurable filter technique has been derived for filters with capacitive coupled resonators. From this technique two filter prototypes were designed and demonstrated. The first prototype is an electronically switchable bandpass filter with two discrete bandwidths at 5.8GHz. The topology has been designed on duroid, a low cost organic substrate intended for system-on-package (SOP) applications. Moreover, the filter presented here is comparable in size to a conventional filter with the same center frequency, which makes it an attractive component for wireless and other RF applications. The use of p-i-n diodes as

switching elements has proven successful. The two distinct bandwidths produced by the filter were 10.12 % with an insertion loss of 3.95 dB and 5.43 % with an insertion loss of 4.73 dB. Nonlinear effects of the diodes in the structure were also studied and measured. The measurements yielded a third order intercept point of $IIP3 > 43$ for tones separated by 1 MHz. This indicates a high level of linearity for the structure.

The second prototype presented in this chapter is a a six-state all tunable band-pass filter. The filter has great potential for applications in modern communication and antenna systems with tunable requirements. The topology was able to produce frequency responses of both narrowband and wideband characteristics with center frequencies of $f_0 = 9$ GHz, 10 GHz and 11 GHz. Simultaneous bandwidth and frequency control has been successfully achieved by a tuning scheme that varies the coupling strength and effective length of the resonators. The circuit produces no significant signal distortion resulting in third-order intermodulation intercept points ($IIP3$) greater than 48 dBm for tones separated by 1 MHz around the center frequencies. The resulting filter is suitable for most commercial and military applications and represents a significant tool for reconfigurable communication systems allowing multiband selectivity and bandwidth control.

CHAPTER 4

DUAL-MODE RECONFIGURABLE FILTERS

Classical microstrip band-pass filters are for the most part designed using single-mode resonators. In recent years, dual-mode resonators have been increasingly used in wireless communication systems and other RF applications for their low loss, and high selectivity characteristics. Because of their double resonant behavior, a dual mode band-pass filter of a certain order requires half as many resonators when compared to a classical topology. Based on the same reasoning it is possible to demonstrate that a dual-mode reconfigurable filter also requires a reduced number of switching elements. Fig. 19 shows some typical resonator topologies used for dual-mode operation. These topologies possess a pair of degenerate modes whose resonant frequencies are split when a perturbation element is strategically introduced. This section shows reconfigurable filter designs achieved by controlling the resonant frequencies and transmission zeros produced by the resonator in dual-mode operation.

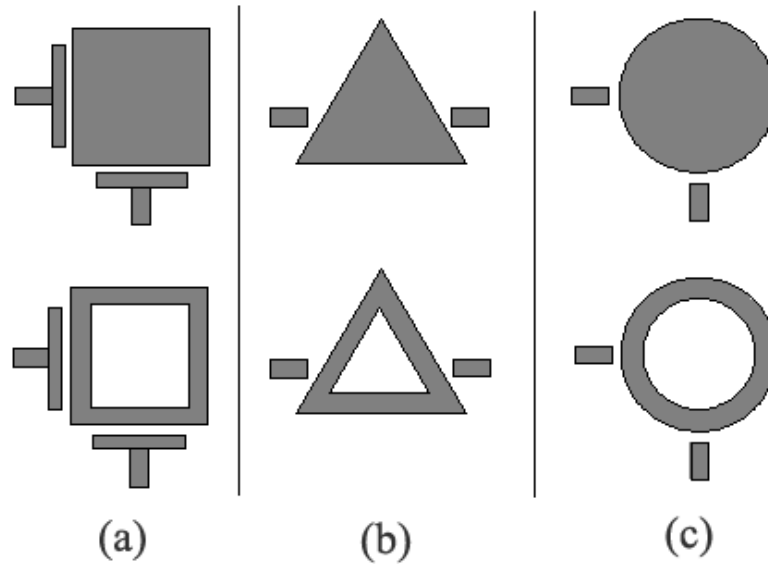


Figure 19. Microstrip loop and patch resonator topologies for dual-mode operation (a) square shape (b) triangular shape (c) circular shape

4.1 Square Loop Topology with Bandwidth Control

A microstrip square loop resonator is capable of producing filter responses with transmission zeros at the real axis of the complex s -plane ($s = j\omega$ where ω is the normalized angular frequency), as well as responses with transmission zeros at real frequencies [55,56]. In this section, a reconfigurable bandpass filter with tunable bandwidth is demonstrated using a dual-mode microstrip square loop resonator. The filter is switched between different perturbation arrangements using two strategically placed p-i-n diodes. This topology results in a 2:1 tunable passband ratio at a fixed center frequency of 10 GHz. The work shown in [57] demonstrates a single-mode reconfigurable filter capable of switching the bandwidth by manipulating the coupling between resonators. Typically, a classical reconfigurable filter requires a set of coupling and compensation stubs to achieve bandwidth variation [58]. Previous investigation of degenerate modes in a square loop suggests that a perturbation size determines not only the type of response but also the bandwidth [59]. In this work we present a single topology capable of switching between a narrowband response with transmission zeros in real frequency and a wideband response with transmission zeros in the real axis of the complex s -plane. It is worth noting that the narrowband state has a more selective "elliptic like" characteristic response while the wideband state has a "Chebyshev like" response.

The proposed microstrip square loop circuit is shown in Fig. 20. The inner side dimension L of the square loop is approximate $\lambda/4$ at 10 GHz, the perturbation cut is about $P = \lambda/16$ and the loop width W corresponds to the characteristic impedance $Z_0 = 50 \Omega$. The PIN diodes D1 and D2 are used to switch between the narrowband and wideband configurations. Perturbations in this topology are placed either in corners B or D and can be made in the form of a stub (positive perturbation) or in the form of a cut (negative perturbation). Once a perturbation is in place, the type of response produced depends on the relative size of the perturbation shape with respect to the reference elements located at the remaining three corners. For example, if one is to place a perturbation in corner B, the

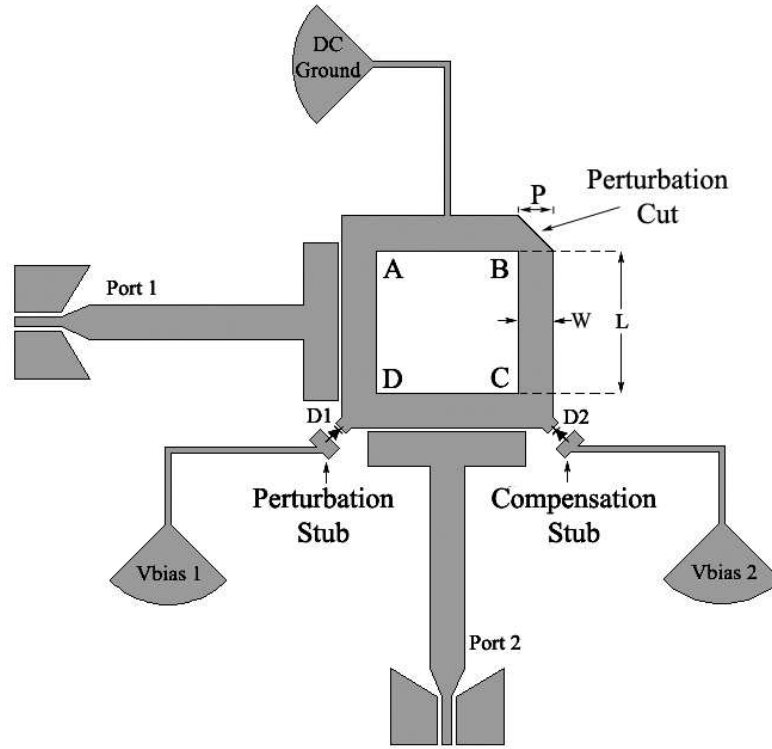


Figure 20. Reconfigurable dual-mode square loop topology

remaining corners A, C and D are reference elements and the relative difference in size between reference and perturbation elements determines whether the transmission zeros will be in the real or imaginary axis of the complex s -plane. The present circuit contains three fundamental elements to control the fractional bandwidth. A permanent perturbation cut located in corner B, a switchable perturbation stub located in corner D and a switchable compensation stub located in reference corner C.

The narrowband state is produced when D1 is forward biased and D2 is reversed biased. In this situation, the perturbation stub is connected producing a capacitive or positive excitation between degenerate modes. The response in this configuration has two transmission zeros located at frequencies on either side of the passband. As mentioned before, corners B and D are the perturbation sections of the square loop. When the perturbation stub is connected to the circuit both corners B (permanent cut) and D (connected perturbation stub) have perturbation shapes. However, the size of the perturbation stub in corner D

has been adjusted via computer optimization to be larger and more dominant than the negative perturbation produced by the cut in corner B. This configuration yields a 5% narrow bandwidth. The wideband state is produced when D1 is reversed biased and D2 is forward biased. In this case, the perturbation stub in corner D is released allowing the permanent cut element located in corner B to become the dominant perturbation element. Consequently, a negative or inductive excitation of the degenerate modes produces a response with zeros in the real axis of the complex s-plane. At this point, the effective size of the square loop has suffered a reduction caused by the isolation of the perturbation stub. This translates to a higher center frequency shift. In order to keep the same center frequency, a reference stub located in corner C is now connected using the diode D2 to compensate for the previously lost effective size. The size of both perturbation and compensation stub was optimized including a lumped element model of the diodes. Both stubs have a length of approximately $\lambda/16$. Because the compensation stub is located in one of the reference corners, the perturbation size with respect to the reference elements is still negative and the effective size of such perturbation is large enough to achieve a 10% bandwidth.

The electric field distribution of the fundamental mode is shown in Fig. 21(a). The fundamental mode of the square loop resonator occurs when no perturbation is present. In this case, the two electric field maxima are located along the left and right edges of the square loop resonator while the two electric field minima are located at the top and bottom edges. When the filter is in the narrowband state, the electric field pattern is rotated 45° in the counter clockwise direction. In this case, the electric field maxima is located along the perturbation corners B and D as shown in Fig. 21(b). On the other hand, the wideband state of the filter produces a field pattern rotation of 45° in the clockwise direction where the electric field maxima are now located along reference corners A and C as shown in Fig. 21(c).

The substrate used in this design was Rogers Duroid, with a dielectric constant of $\epsilon_r = 10.2$, a substrate thickness of 25 mils with 0.5 OZ of copper metallization and $\tan\delta =$

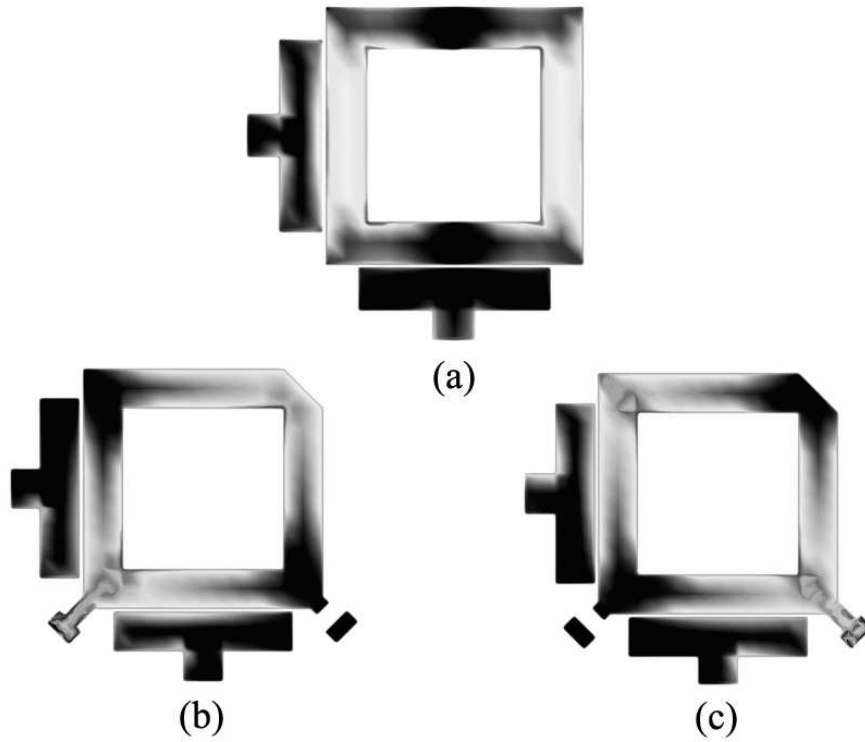


Figure 21. Electric field distribution at the center frequency. (a) Electric field distribution of a single mode (topology without perturbations) (b) Narrowband state. (c) Wideband state. Dark sections represent electric field minima. Light sections represent electric field maxima.

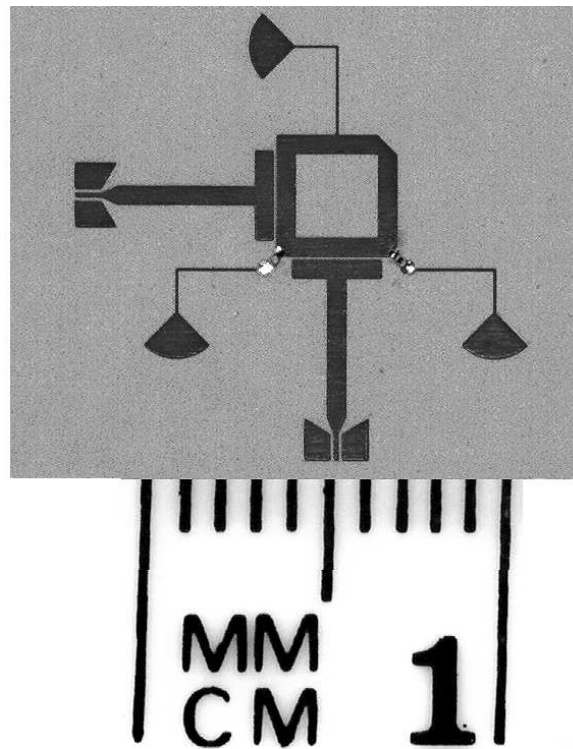


Figure 22. Picture of fabricated filter with DC bias lines

0.025. The diodes used were ASB 8000 by ASI. The filter was fabricated using standard photolithography techniques. The PIN diodes were fixed to the board using silver epoxy. A picture of the fabricated filter is shown in Fig. 22. The effective filter size excluding the CPW to microstrip transitions, for on wafer probing, is about 1 cm x 1 cm. The DC bias lines are designed as RF chokes and consist of a high impedance transmission line terminated in an open radial stub for a total effective length of $\lambda/2$. The PIN diode was modeled and added to the simulations as a $3\ \Omega$ resistor for the forward biased state and 0.025 pF capacitor for the isolation state. The forward bias current was limited to $I_f = 30$ mA and the reverse bias voltage was $V_r = -10$ V. The transmission and return loss of the wideband and narrowband states of the filter are shown in Fig.23 and Fig.24, respectively. Excellent agreement can be observed between the measured and simulated results. The measured insertion loss of the filter in the wideband state was 1.70 dB, while the insertion loss of the filter in the narrowband state was 2.56 dB. This loss is partially attributed to the diodes, and as expected the narrow band responses had slightly higher insertion loss than the wideband responses. The narrowband response has transmission zeros located at 9.2 GHz and 11.8 GHz and a bandwidth of 4.45%. The wideband state had a bandwidth of 10.4% for a 2:1 tunable passband ratio.

Signal distortion was also investigated using a two-tone method similar to the one used in section 3.1. The intercept points vs. tone separation Δf are shown in Fig. 25. The narrowband response produced the lowest IIP3 of 19 dBm for $\Delta f = 100$ kHz and 47 dBm for $\Delta f = 1$ MHz. The wideband configuration resulted in the highest intercept points. For $\Delta f = 100$ kHz the IIP3 was greater than 22 dBm and for $\Delta f = 1$ MHz the IIP3 was greater than 56 dBm.

Higher order filters can be designed by appropriately cascading several dual-mode resonators. Fig. 26(a) shows a standard four-pole configuration. The ports and the edges of the coupled resonators determine the line of symmetry. Fig. 26(b) shows a four-pole cross coupled configuration using non resonant nodes. These nodes relocate the line of symmetry

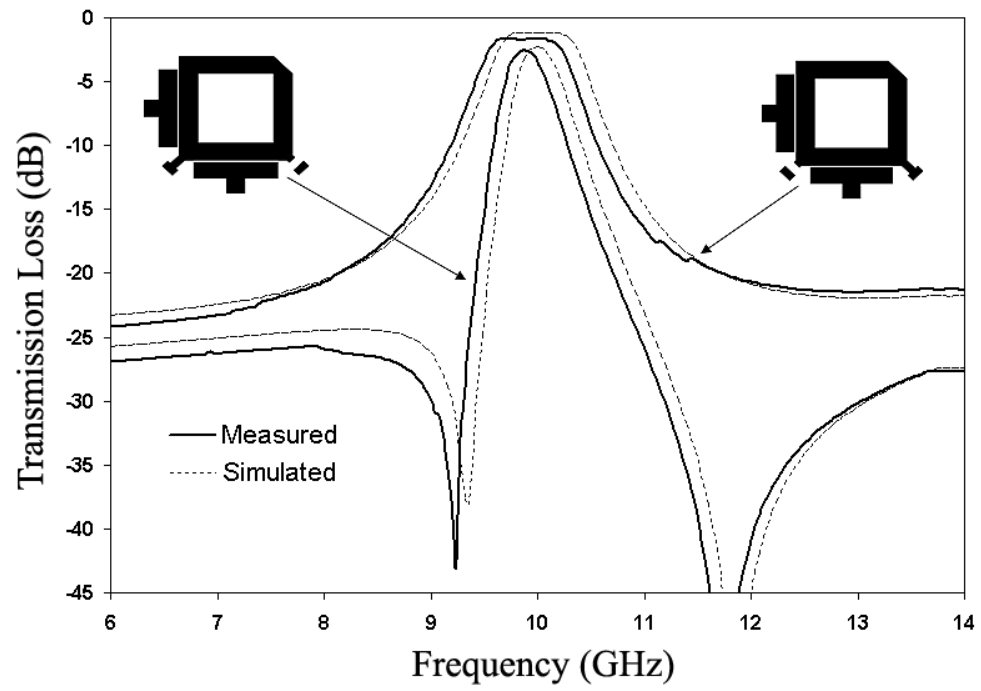


Figure 23. Measured and simulated S21 parameters of the wideband and narrowband state

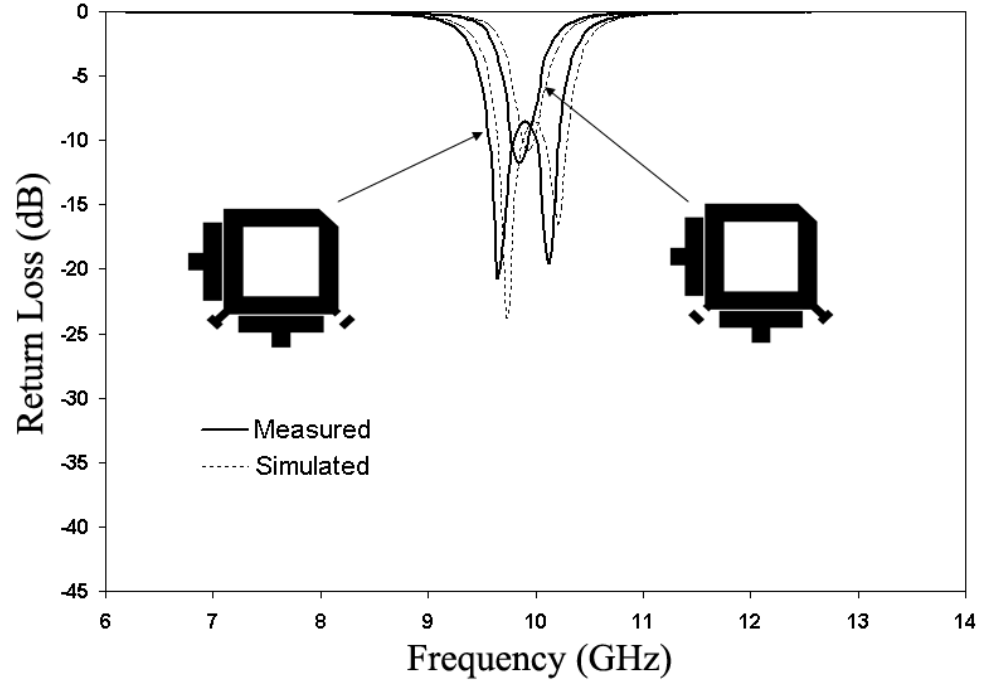


Figure 24. Measured and simulated S11 parameters of the wideband and narrowband state

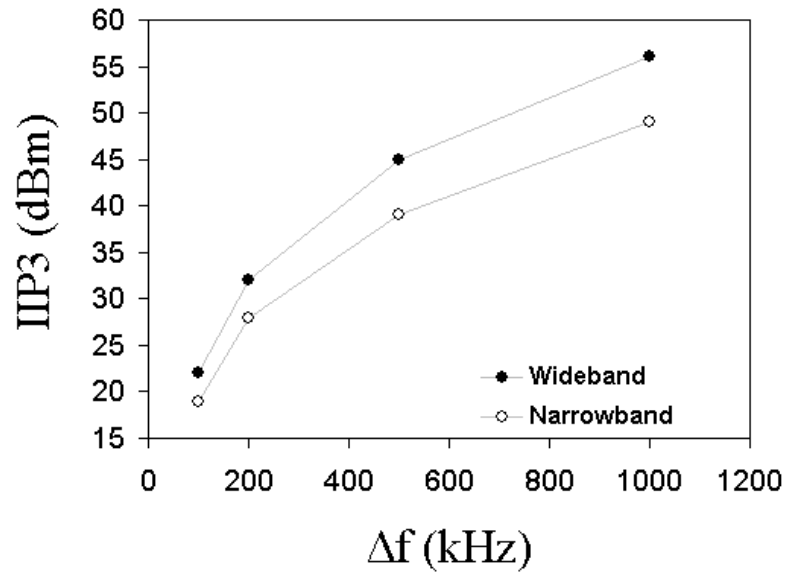


Figure 25. Measured intermodulation third order intercepts IIP3

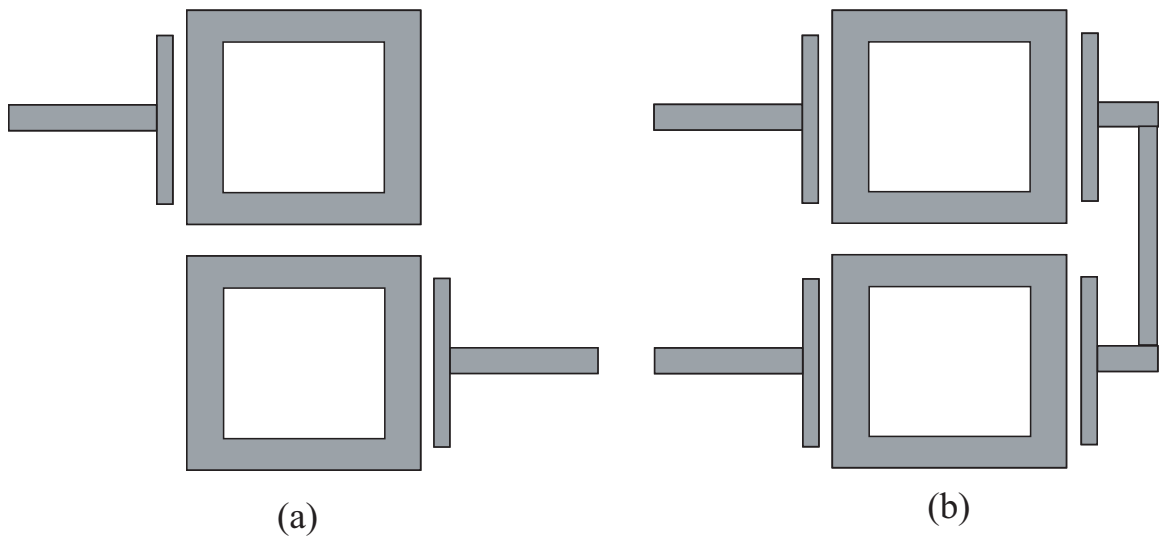


Figure 26. Higher order filters using dual-mode square loops. (a) Four pole filter configuration. (b) Four pole filter with non resonant nodes

and allow extra mode couplings, hence producing extra transmission zeros. This procedure can be used to increase the even number of poles produced by dual-mode resonators; the perturbations are located according to the symmetry of the filter.

4.2 Single Switch Triangular Patch Topology

A reconfigurable bandpass filter is demonstrated using a dual-mode microstrip triangular patch resonator. The proposed circuit uses a single switch to control its fractional bandwidth while keeping a fixed center frequency of 10 GHz. The switching mechanism is accomplished by a p-i-n diode that connects and isolates a tuning stub from the rest of the circuit. The on and off state of the diode effectively controls the resonance frequencies of the two poles produced by the dual-mode behavior of the resonator. The filter achieves a measured 1.9:1 tunable passband ratio. The circuit presented here represents the first single switch bandwidth reconfigurable filter that requires no size compensation to maintain a fixed center frequency.

One of the main reasons for the extra complexity found in bandwidth variable designs is the dependency that exists between the filter's bandwidth and center frequency. In conventional filters, the bandwidth is varied by changing the capacitance between coupled resonators. It is a difficult task to independently vary this capacitance without affecting the resonator size. In general, single mode filters use extra switches and stubs to keep constant resonator lengths and fix the center frequency. In dual-mode filters, the size of the perturbation determines the bandwidth [55,60]. However, as seen in the square shape topology, only one of the resonant poles produced by the dual-mode behavior can be controlled [36,59]. Moving the spectral location of only one of the resonant poles results in bandwidth variation with an inherent frequency shift that requires the introduction of length compensation. This particular characteristic eliminates the possibility of designing a bandwidth variable filter by simply changing the perturbation size in a conventional dual-mode topology. In this work we present a circuit capable of producing a narrowband and a wideband response

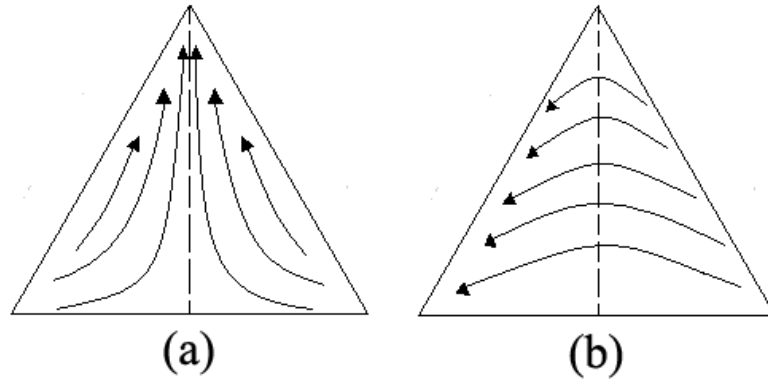


Figure 27. Current distributions of the degenerate modes in a microstrip triangular patch (a) Even mode (mode 1). (b) Odd mode (mode 2).

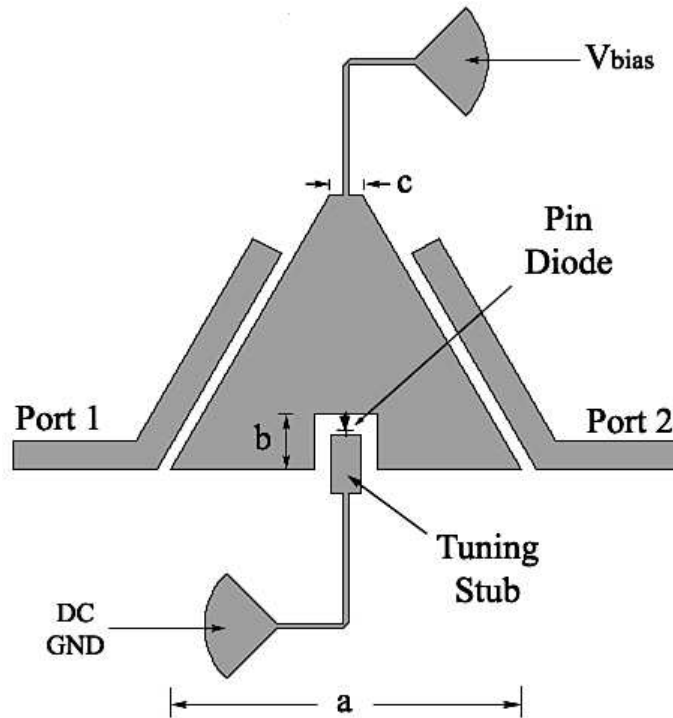


Figure 28. Proposed reconfigurable filter.

at the selected center frequency of 10 GHz. The filter requires no size compensation and the tunability is accomplished by a single switch.

The circuit presented here is closely related to the dual-mode microstrip triangular patch resonator. For this reason, it is worth mentioning some key characteristics about the conventional triangular patch topology. The current distributions of the degenerate modes in a triangular patch are shown in Fig. 27. These current distributions exhibit an even (mode 1)

and an odd (mode 2) symmetry with respect to the vertical symmetrical plane [36]. These degenerate modes are split when a perturbation is introduced in the form of a cut to the top vertices of the equilateral triangular patch. It is also known that when this cut is present, the mode 1 resonance is located at a slightly higher frequency than mode 2 [62]. As mentioned before, changing the perturbation cut size, changes the bandwidth by manipulating the resonance frequency of one of the modes, in this case mode 1. Although this resonance variation yields a change in the fractional bandwidth, the center frequency does not remain fixed. The main goal is to find a manipulation that would simultaneously change the resonance frequency of both modes, placing them at an equal spectral distance on either side of the center frequency. This simultaneous control of the resonant poles should also achieve a wideband characteristic where the poles exhibit some predetermined spectral separation and a narrowband characteristic where the resonant poles are placed closer together.

The proposed 2-pole filter topology is shown in Fig. 28. The side dimension of the equilateral triangular patch is $a = 6$ mm, approximately $\lambda/2$ at 10 GHz. The filter responses are achieved by making three fundamental perturbations. The first perturbation consists of a small cut of size $c = \lambda/20$ placed on the top vertex. This results in the conventional split of the degenerate modes. A second perturbation consists of a square cut of side dimension $b = \lambda/10$ centered at the base of the triangle. This new perturbation is introduced in order to simultaneously change the resonant frequencies of the degenerate modes. The final perturbation is a tuning stub placed inside the square cut. The effective length of the stub is 1.6 mm, approximately $3\lambda/20$. This stub is isolated or connected to the circuit using the p-i-n diode as a switch. Two discrete states are produced depending on the biasing of the diode. When the diode is reversed biased and the tuning stub is isolated the wideband state is produced with a fractional bandwidth of 8.6 %. On the other hand, when the diode is forward biased connecting the tuning stub to the triangular patch, a narrowband state is produced with a fractional bandwidth of 4.5 %. The DC bias lines are designed as RF chokes and consist of a high impedance transmission line terminated in an open

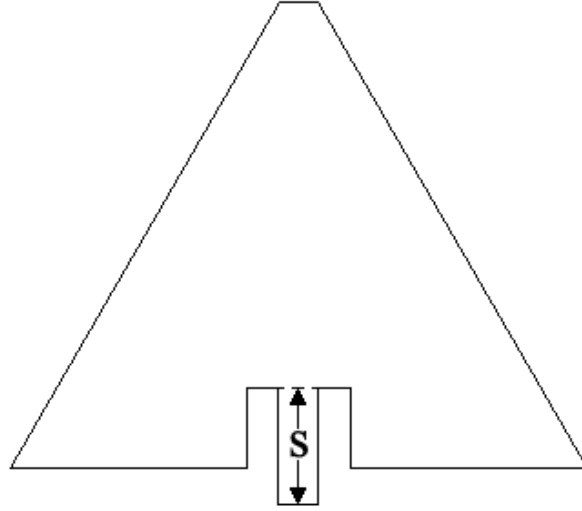


Figure 29. 2-pole filter with weakly input/output coupling and variable tuning stub length S .

radial stub for a total effective length of $\lambda/2$. The dimensions of this filter were found via computer optimization using the full wave simulator Agilent momentum. Although the present design is intended for X band applications, the topology may be scaled for use in other frequency bands.

In order to better understand the functionality of the proposed design, it is worth observing the pole locations produced by a filter with the three types of perturbations mentioned above, and a weakly input/output coupling. Using the topology shown in Fig. 29, the tuning stub length S will be varied using dimensions $S = 0$ mm, 1 mm, 1.4 mm and 1.8 mm. The simulated pole locations produced by the different stub lengths are shown in Fig. 30. When $S = 0$ mm the resonant poles are located at 9.4 GHz and 10.6 GHz. This can be considered the "wideband state" of the filter with a center frequency of 10 GHz. When $S = 1$ mm the new pole locations are 9.6 GHz and 10.4 GHz resulting in a reduced fractional bandwidth with the same center frequency of 10 GHz. When S is further increased, mode 2 remains constant at 9.6 GHz while mode 1 is placed at lower frequencies. Hence, for some small perturbation variation in this case $S = 0$ mm to $S = 1$ mm the filter is capable of changing the bandwidth and keep a fixed center frequency without the need of a size compensation. It is worth noting that this simultaneous pole manipulation, where modes 1

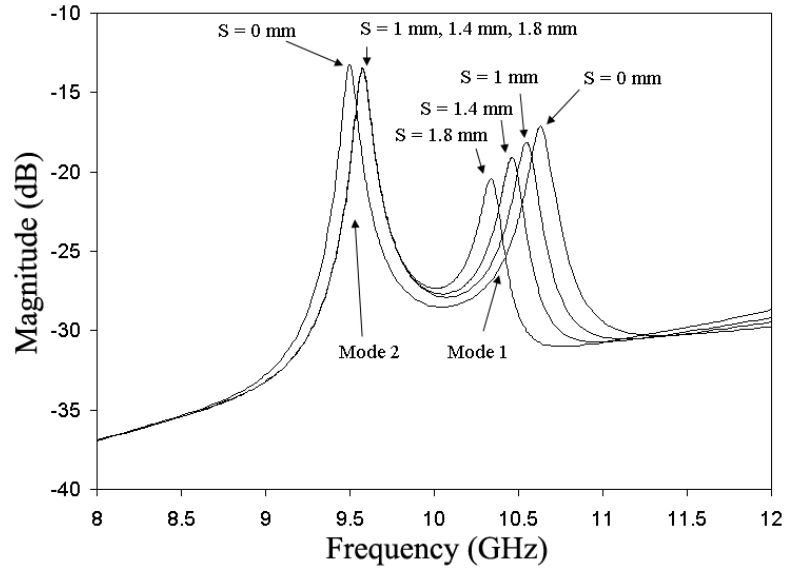


Figure 30. Simulated frequency location of the resonant poles produced by the filter in Fig. 29.

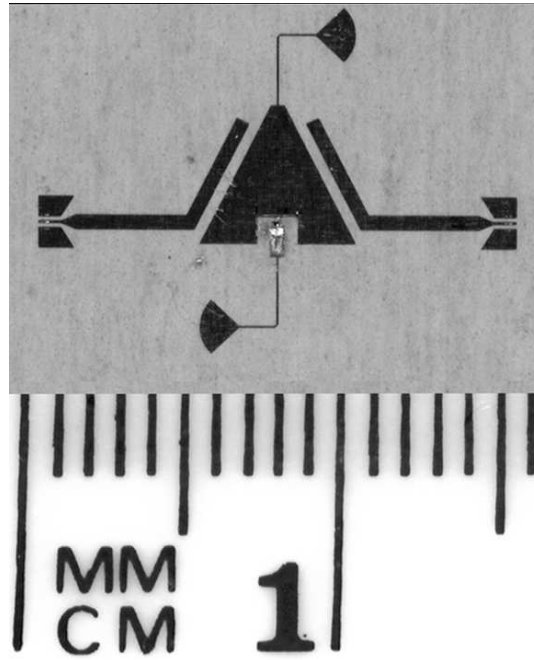


Figure 31. Picture of fabricated filter.

and 2 are placed closer in frequency to each other ($S = 1 \text{ mm}$) and away from each other ($S = 0 \text{ mm}$) can not be accomplished without the presence of the the square cut centered at the base of the triangle. In other words, if one is to use a conventional triangular patch and attach the tuning stub to the base of the triangle, only the resonant frequency of mode 1 is controlled.

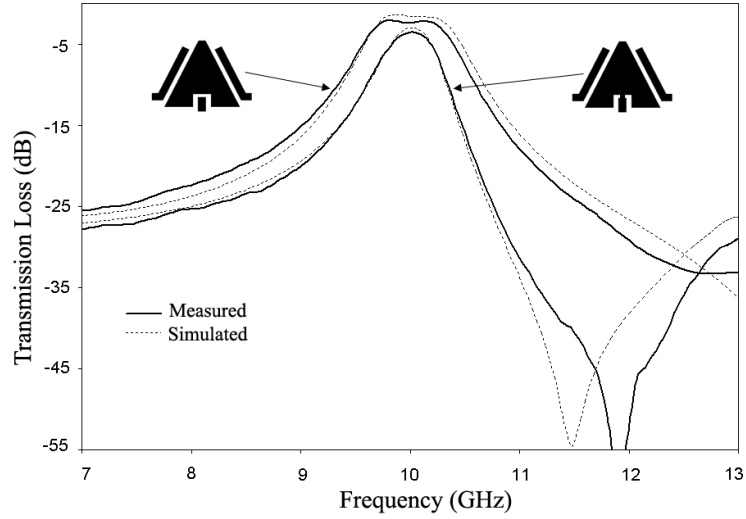


Figure 32. Measured and simulated transmission loss.

The substrate used in this design was Rogers Duroid, an organic material with a dielectric constant of $\epsilon_r = 10.2$. The substrate thickness is 25 mils with 0.5 OZ of copper metallization and a loss tangent of 0.025. The diode used was ASB 8000 by ASI. The filter was fabricated using standard photolithography. The p-i-n diode was fixed to the board using silver epoxy. A picture of the fabricated filter is shown in Fig.31. The size of the circuit excluding the CPW to microstrip transitions, for on wafer probing, is about 7 mm x 10 mm. A lumped element model of the diode was included in the simulations as a 3 Ω resistor for the forward biased state and 0.025 pF capacitor for the isolation state. The forward bias current was limited to $I_f = 30$ mA and the reverse bias voltage was $V_r = -10$ V. The transmission and return loss of the wideband and narrowband states of the filter are shown in Fig.32 and Fig.33, respectively. Excellent agreement can be observed between the measured and simulated results. The measured insertion loss of the filter in the wideband state was 2.17 dB at 10 GHz, while the insertion loss of the filter in the narrowband state was 3.25 dB, also at 10 GHz. The narrowband response exhibits a transmission zero located 11.9 GHz and a bandwidth of 450 MHz (4.5 %). The wideband state produced a bandwidth of 860 MHz (8.6 %) for a measured 1.9:1 tunable passband ratio.

Signal distortion was again investigated using the standard two tone measurement set

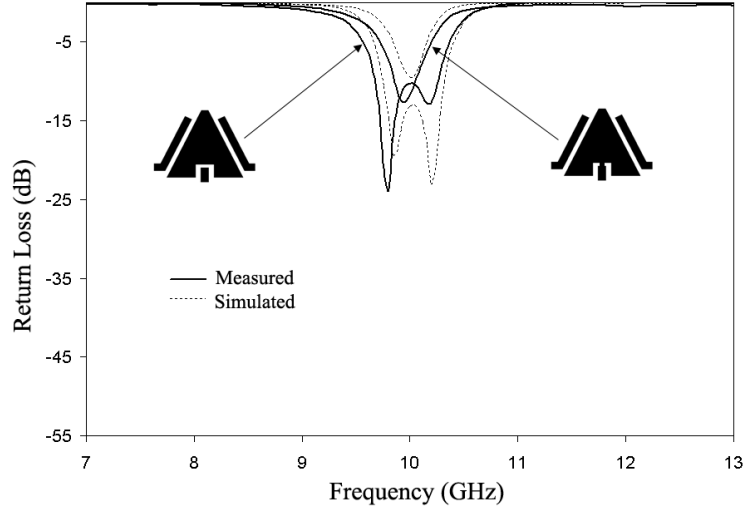


Figure 33. Measured and simulated return loss.

Table 3. Third Order Intercept Points

Δf (kHz)	Wideband IIP3 (dBm)	Narrowband IIP3 (dBm)
100	21	20
200	30	28
500	42	39
1000	57	55

up. The intercept points vs. tone separation are summarized in Table 3. The measured results indicate that the filter behaves linearly with intercept points higher than 55 dBm for signals separated by $\Delta f = 1000$ kHz and 39 dBm for $\Delta f = 500$ kHz. The linearity levels achieved by the single switch filter makes the design suitable for many RF front end applications.

Tunable filters with triangular shape can be designed with higher order by cascading the dual-mode resonators. Fig. 34 conceptually shows a higher order configuration for the tunable triangular patch. The standard symmetrical method is again used in this case. It is worth to notice that the capacitive coupling created by the gaps may require the introduction of extra tunable schemes to control the coupling between resonators.

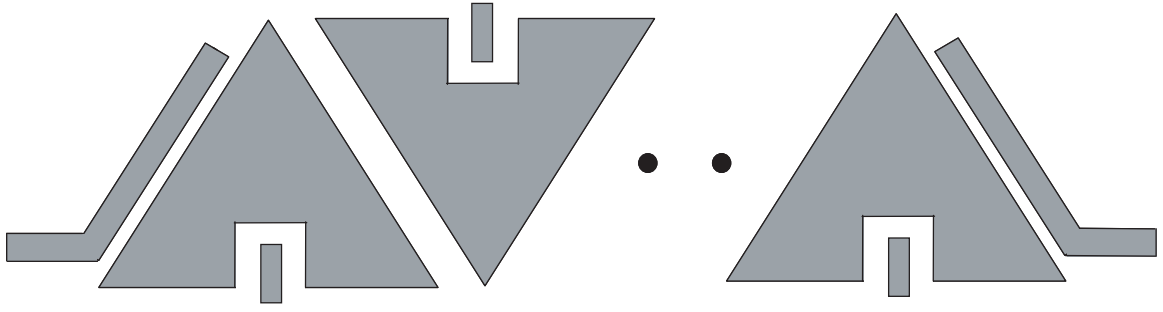


Figure 34. Standard cascaded configuration to produce higher order filters using dual-mode triangular patch resonators

4.3 Chapter Summary

This chapter explored the use of dual-mode resonators to create tunable filters. The second order degeneracy produced by these resonators allow direct access and control to multiple resonant poles. This provided an effective way to reduce the number of tuning elements and circuit complexity when compared to single-mode reconfigurable filters. The first prototype demonstrated a reconfigurable bandpass filter with tunable bandwidth using a dual-mode microstrip square loop resonator. The topology was able to produce frequency responses of both narrowband and wideband configurations with a center frequency of 10 GHz. The filter was switched between different perturbation arrangements using two strategically placed p-i-n diodes. This topology results in a 2:1 tunable passband ratio at 10 GHz. The dual mode operation of the filter allows for a compact reconfigurable design.

The first tunable filter that uses a single switch to control its fractional bandwidth was also presented in this chapter. The switching mechanism made possible the simultaneous control of the resonant frequencies of the degenerate modes produced by the microstrip triangular patch resonator. This frequency control of degenerate modes eliminated the use of the size compensation scheme otherwise needed to keep the responses fixed at a center frequency. The topology was able to produce frequency responses of both narrowband and wideband configurations with a measured tunable passband ratio of 1.9:1. Intermodulation measurements indicated that the filter exhibits a linear behavior with no significant distortion for signals with frequency separation greater or equal to 500 kHz. Also, using the

standard coupling scheme for triangular patch resonators, the design can be expanded for multi-pole reconfigurable filters.

CHAPTER 5

FILTERS WITH ASYMMETRICAL RESPONSES

In general, dual mode filters produce symmetrical responses with chebychev or elliptic characteristics. In this work, a new type of dual-mode resonator is introduced. This resonator produces asymmetrical responses that can be implemented to meet specifications with uneven sideband requirements. Filters with asymmetric frequency responses are favored over symmetrical filters in cases of close assignment transmit and receive bands. These type of filters can meet selective requirements in one side of the passband and reduce the filter order, thus lowering the in-band insertion loss. The topology presented here consists of a microstrip loop that has been shaped as an equilateral triangle. Four basic topology variations that result from the perturbation forms and location are described. These perturbations successfully accomplish the rotation and superposition of the fundamental mode creating the dual-mode behavior of the resonator. It is well known that microstrip patches possess an advantage in terms of insertion loss over the microstrip loop versions; however, it is also true that microstrip loop resonators are inherently smaller in size. The search for more compact topologies with dual-mode characteristics has led to the realization of the microstrip triangular loop resonator.

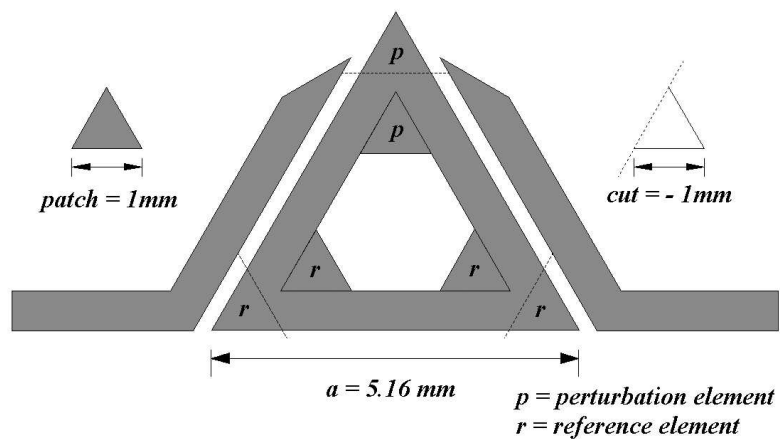


Figure 35. Proposed topology

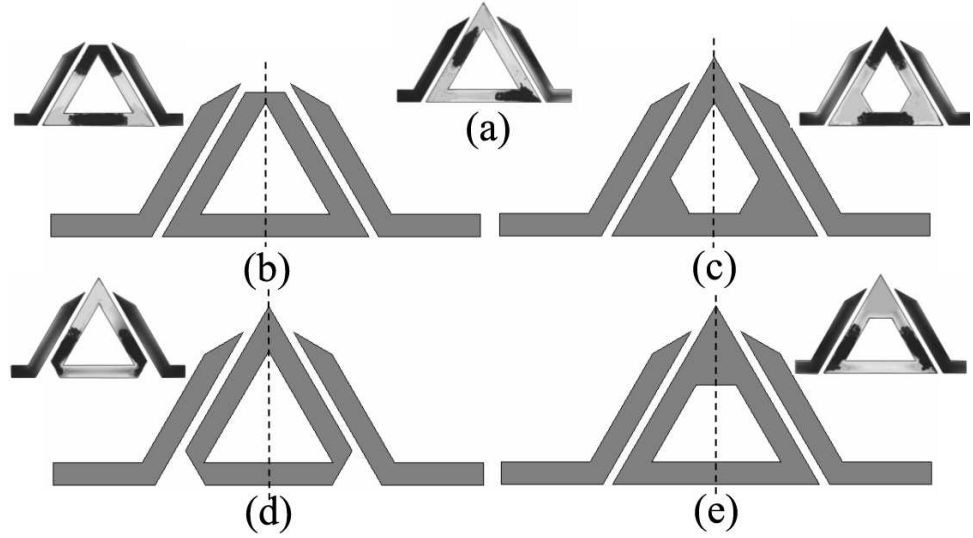


Figure 36. Topology configuration with respective simulated electric field pattern. (a) $p = r = 0$. (b)-(c) $p < r$. (d)-(e) $p > r$. Lighter sections indicate field's maxima. Darker sections indicate field's minima.

5.1 Asymmetrical Response of the Dual-Mode Triangular Loop Resonator

The triangular loop filter is shown in Fig. 35. The circuit is designed for X-band applications, but it can be implemented in other frequency bands. The side dimension of the loop is $a = 5.16$ mm which is approximately $\lambda/2$. The top corner of the triangle is the perturbation section with perturbation size p . The left and right lower corners are the reference sections with reference element size r . These element/perturbation sizes determine the bandwidth of the resonator [4]; in the present case it was found via computer optimization that a 8 % bandwidth is obtained with cut and patch sizes of -1 mm and 1 mm, respectively ($\sim \lambda/10$). Hence, perturbation to these type of topologies can be made in a form of a patch (positive perturbation) represented by $p = 1$ mm, cut (negative perturbation) given by $p = -1$ mm or a corner without perturbation $p = 0$ mm. Both lower left and right reference corners have the same type of reference element per design either positive (patch) $r = 1$ mm, negative (cut) $r = -1$ mm or unchanged $r = 0$ mm.

When the condition $p < r$ is met, a filter response is produced with one transmission zero on the positive real axis and one on the positive imaginary axis of the complex s -plane ($s =$

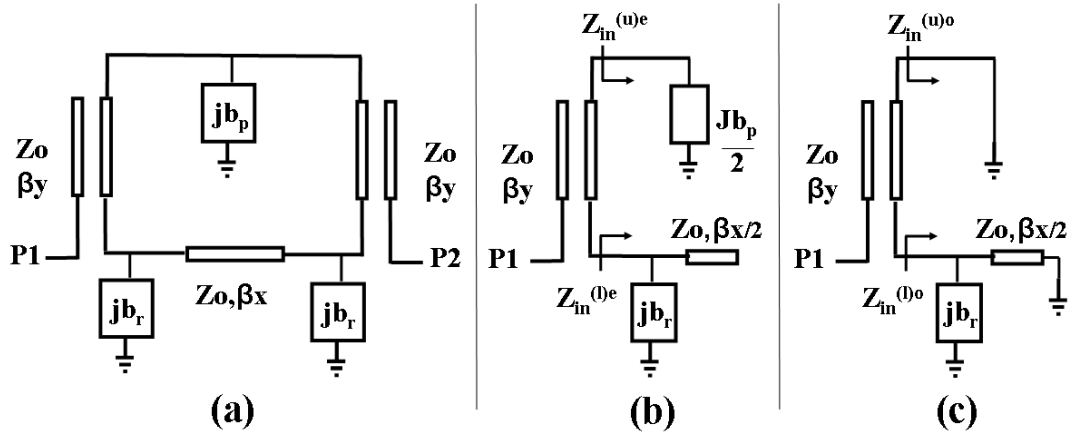


Figure 37. (a) Transmission line model (b) Model with magnetic wall for even mode (b) Model with electric wall for odd mode.

$j\omega$ where ω is the normalized angular frequency). Two perturbation arrangements can be used to achieve this condition. Fig. 36(b) shows a configuration with a perturbation size of $p = -1$ mm and reference elements with a size of $r = 0$ mm. In this case the zeros are located at $s = 6.53$ and $j15.21$. Fig. 36(c) shows a second arrangement that produces the same type of response. In this case, $p = 0$ mm while $r = 1$ mm. The zero locations are $s = 5.47$ and $j16.38$. A response with transmission zeros at the negative imaginary and negative real axis of the complex s -plane is created when $p > r$. This condition is satisfied by setting $p = 0$ mm and $r = -1$ mm as shown in Fig. 36(c). The zeros in this case are located at $s = -j6.53$ and -15.21 . Also, an equivalent filter can be produced when $p = 1$ mm and $r = 0$ mm, see Fig. 36(d) the zeros are located at $s = -j5.47, -16.38$. The relative distance from the ports to the perturbation/reference elements as well as the input/output side coupling represent the main differences between the present design and the loop resonators of square or circular shape. These differences have proven nontrivial producing the unique zero placing behavior described above. The circuit possesses a greater variety of perturbation arrangements over the triangular patch and as expected it is also smaller in size than the dual mode patch resonators.

The electric field patterns computed with the EM full-wave simulator HFSS are shown in Fig. 36. A triangular loop with both perturbation and reference elements sizes set to

Table 4. Resonant Frequencies and Coupling Factor

Topology	f ₁ GHz	f ₂ GHz	f ₀₁ GHz	f ₀₂ GHz	k
Fig.36(b)	10.22	10.01	9.98	9.52	0.0424
Fig.36(c)	10.26	10.13	10.14	9.61	0.0522
Fig.36(d)	9.77	10.24	9.11	9.72	0.0455
Fig.36(e)	9.85	10.29	9.31	9.41	0.0371

zero, $p = r = 0$ mm is shown in Fig. 36(a). Two electric field maxima and minima form the depicted pattern at the center frequency of 10 GHz. The field's maxima are observed in the lower left corner as well as in the right edge of the triangle while the field's minima are located in the lower right corner and in the left edge of the triangular loop. When the condition $p < r$ is met, the electric field pattern is rotated in the clockwise direction by 60° as shown in Fig. 36(b) and (c). The field's minima are now located in the top corner and in the lower edge of the loop. Similarly, when $p > r$ the electric field pattern undergoes a 60° rotation in the counterclockwise direction as depicted in Fig. 36(d) and (e). In this case the field's minima are located in the lower section of the left and right edges of the loop.

The transmission line model of the resonator is shown in Fig. 36(a). For topologies with $p = 0$ the relative lengths are $x = 3\lambda/8$ and $y = 5\lambda/16$. When $p \neq 0$ $x = 5\lambda/16$ and $y = 3\lambda/8$. The parameters bp and br are related to the perturbation/reference type and can be capacitive $-1/\omega C$ or inductive ωL [4]. The models in Fig.37(b) and (c) result when a magnetic or electric wall is respectively placed along the line of symmetry. From Fig.37(b) it is easily seen that $Z_{in}^{(u)e} = jbp/2$ and from Fig.37 (c) $Z_{in}^{(u)o} = 0$. The lower arm input impedances are given by

$$Z_{in}^{(le)} = \frac{-j(-br + Z_0 \cot(1/2\beta x))}{Z_0 \cot(1/2\beta x) br} \quad (21)$$

$$Z_{in}^{(lo)} = \frac{-j(-br + Z_0 \tan(1/2\beta x))}{Z_0 \tan(1/2\beta x) br} \quad (22)$$

The input impedance at port 1 is found by simply writing the currents and voltages of the coupled line section including the input impedance for each arm. for example, the system

of equations described in (3) consists of matrices $\in \mathbb{C}^{4 \times 4}$ and vectors $\in \mathbb{C}^4$.

$$\begin{bmatrix} Z & -I \\ C & D \end{bmatrix} \begin{bmatrix} i \\ V \end{bmatrix} = \begin{bmatrix} 0 \\ e_1 \end{bmatrix} \quad (23)$$

where Z is the impedance matrix of the coupled line section, I is the identity matrix, C is a diagonal matrix specifying the input impedances with entries $C_{11} = C_{44} = 1$ and $C_{22} = Z_{in}^{(l)e,o}$ and $C_{33} = Z_{in}^{(u)e,o}$. D contains the excitation parameters with $D_{22} = D_{33} = -1$ and zeros elsewhere. The vector i contains the currents at the 4 ports of the coupled lines while V contains the voltages. e_1 contains all zeros with a one on the first entry and it is placed under a zero vector. The total input impedance can be found by solving the system where $V_1 = i_1 Z_{in}^{e,o}$ and $i_1 = 1$ as specified by matrices C and D . At resonance $Y_{in}^{e,o} = 1/Z_{in}^{e,o} = 0$. With the electric and magnetic wall placed along the line of symmetry, the even and odd self resonant frequencies are ω_{01} and ω_{02} . When the electric or magnetic wall is removed the resonant frequencies of the resonator are represented by ω_1 and ω_2 . The degenerate modes in this topology are asynchronously tuned with $\omega_{01} \neq \omega_{02}$ and also coupled with $\omega_1 \neq \omega_{01}$ and $\omega_2 \neq \omega_{02}$. The resonant and self resonant frequencies of all 4 configurations are summarized in table I. The coupling factor k is given by [6].

$$k = \frac{1}{2} \left(\frac{\omega_{02}}{\omega_{01}} + \frac{\omega_{01}}{\omega_{02}} \right) \sqrt{\frac{(\omega_2^2 - \omega_1^2)^2}{(\omega_2^2 + \omega_1^2)^2} - \frac{(\omega_{02}^2 - \omega_{01}^2)^2}{(\omega_{02}^2 + \omega_{01}^2)^2}} \quad (24)$$

Referring to the transmission line model in Fig.37(a), the impedance matrix of the upper arm $Z^{(u)}$ (excluding the coupled lines) has jbr in all its entries. The impedance matrix for the lower arm $Z^{(l)}$ is given by (5) and (6)

$$Z_{11}^{(l)} = Z_{22}^{(l)} = \frac{j(Zo \sin(\beta x) + \cos(\beta x) br) br Zo}{2 \cos(\beta x) br Zo - \sin(\beta x) br^2 + Zo^2 \sin(\beta x)} \quad (25)$$

$$Z_{12}^{(l)} = Z_{21}^{(l)} = \frac{jZo br^2}{2 \cos(\beta x) br Zo - \sin(\beta x) br^2 + Zo^2 \sin(\beta x)} \quad (26)$$

using a similar analysis as in (3), the total transmission admittance from port 1 to port 2 can be calculated and the zeros will occur when $Y_{21}^{(t)} = 1/Z_{21}^{(t)} = 0$. The location of the zeros can

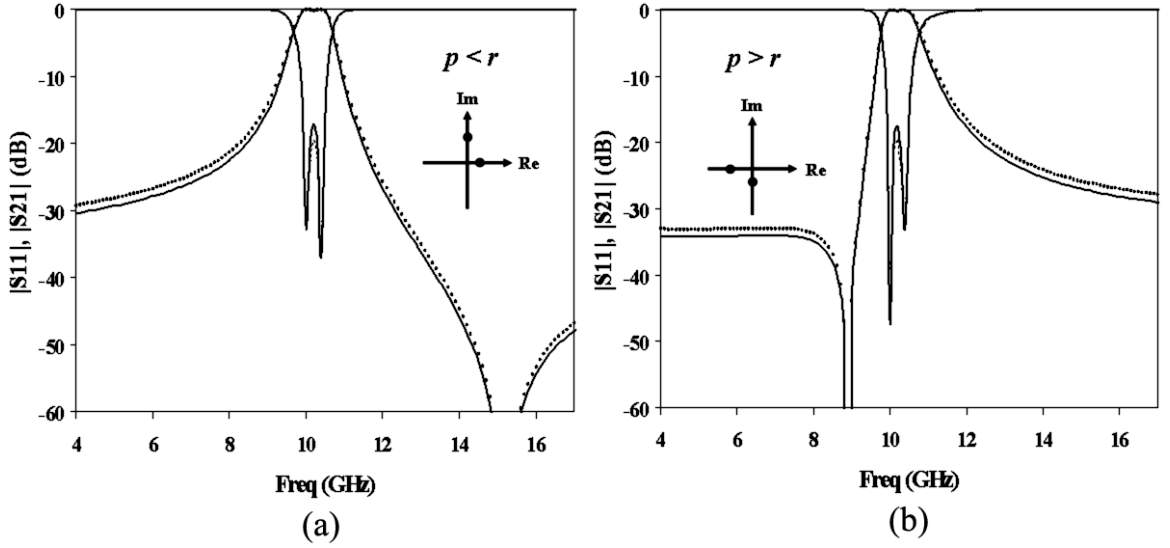


Figure 38. Transmission line model response (solid line) Vs. Chebyshev filtering function (dotted line) with (a) zeros at $s = 6.53$ and $j15.21$ (b) zeros at $s = -j6.53$ and -15.21

be verified by making a direct comparison between the chebyshev filtering function and the filter's frequency response [7]. This comparison is shown in Fig. 37 where an excellent agreement is observed. The chebyshev filtering function of order N is given by [8]

$$C_N(\omega) = \cosh \left(\sum_{n=1}^N \cosh^{-1}(x_n) \right) \quad (27)$$

where $x_n = (\omega - 1/\omega_n)(1 - \omega/\omega_n)^{-1}$ and ω_n is the n^{th} zero location. The theoretical frequency response can be obtained using (7) and $S_{21}^2 = \left(1 + \epsilon^2 C_N^2(\omega)\right)^{-1}$, where $\epsilon = (10^{RL/10} - 1)^{-1/2}$ is the normalizing constant with return loss RL in dB.

The substrate used in this design was Rogers Duroid, with a dielectric constant of $\epsilon_r = 10.2$, a substrate thickness of 25 mils, 0.5 OZ of copper metallization and $\tan\delta = 0.025$. The filter was simulated using the EM solver Agilent Momentum. The measured transmission and return loss of the filter meeting the perturbation condition $p < r$ is shown in Fig. 38(a). The insertion loss at the center frequency was 1.4 dB and both filters yield a bandwidth of 8%. The filter responses with $p > r$ are shown in Fig.38(b). In this case the insertion loss at the center frequency was 0.82 dB The bandwidth of these two filters was also 8%. These designs exhibit center frequency shifts due to the effective size added or subtracted when the perturbation elements are included. This frequency shift can be compensated by

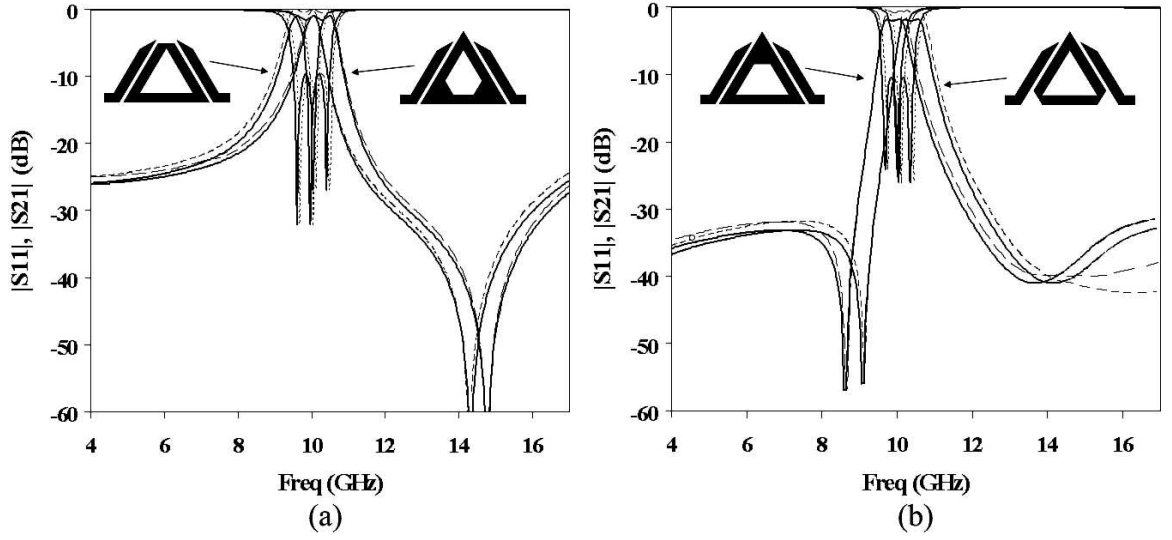


Figure 39. Measurement results (solid line), EM simulation results (dashed line). (a) Configurations with $p < r$. (b) Configurations with $p > r$.

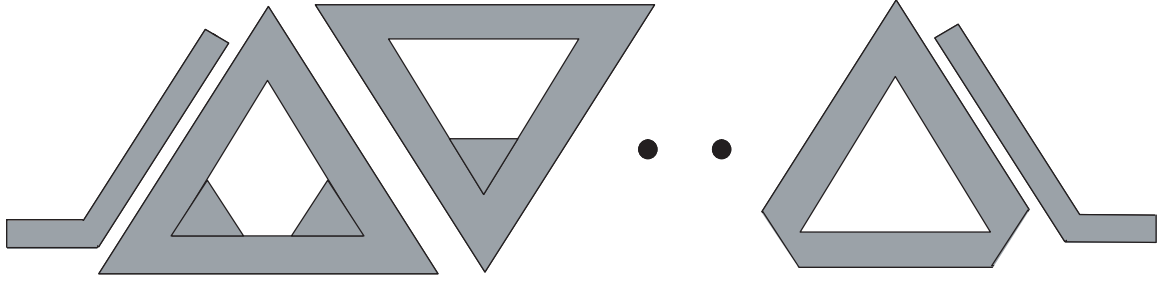


Figure 40. Higher order realizations using triangular loop resonators

simply reducing or increasing the size of the loop. However, it was interesting to observe the shifting tendency of each topology when the ring was kept at a constant size. The arrangements with $r > 0$ always exhibit a higher frequency shift. It can be argued that both the patches and cuts added when $r = 1$ mm and $r = -1$ mm make the effective size of the inner loop smaller. Also, since the self resonant frequencies of the degenerate modes $\omega_{01} > \omega_{02}$ when $p < r$ and $\omega_{01} < \omega_{02}$ when $p > r$ higher order filters may be designed by coupling the resonators as demonstrated in [5].

Higher order realizations may be possible using the standard configuration for triangular shaped resonators. Fig. 40 shows the standard configuration for resonators with triangular shape. The properties of dual-mode triangular loops allows filters with more complex placement of zeros in both imaginary and real axis of the s -plane.

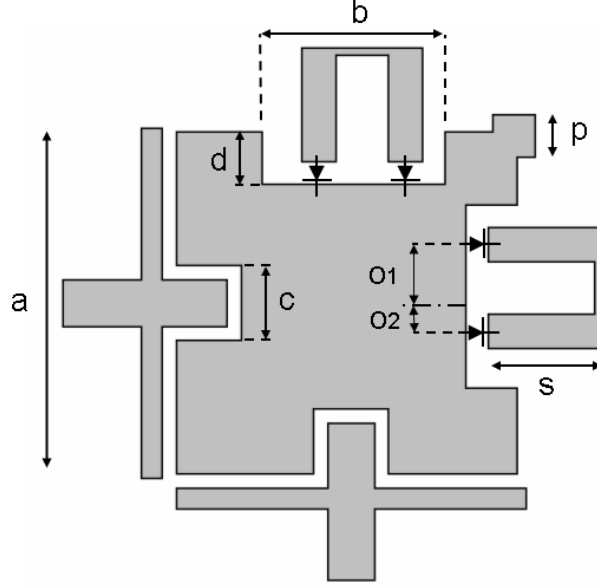


Figure 41. Proposed reconfigurable filter topology.

5.2 Topology with Asymmetrical Control of Transmission Zeros

In this section, a reconfigurable bandpass filter with asymmetrical responses is demonstrated using a dual-mode microstrip resonator. The proposed topology introduces several fixed and switchable perturbations to control the center frequency and the location of the transmission zeros of the filter. The tuning mechanism consists of capacitively loading the edges of a modified square patch resonator, in order to manipulate the current distribution of the degenerate modes. This operation results in asymmetrical responses with center frequency tuning ratio of 10% at X band, and angular transmission zero displacement of $\Delta\omega_z = 3.5$ rad/sec or greater in both lower and higher side of the passband.

The proposed dual-mode filter topology is shown in Fig. 41. This design is intended for advanced filtering applications at X band. However, a broader range of applications may be possible by simply scaling the filter to operate at other frequency bands. The goal is to produce two frequency responses with discrete tuning. The first filter response has a center frequency of $f_0 = 10$ GHz and asymmetrically placed transmission zeros at $f_{z1} = 11.4$ GHz and $f_{z2} = 9.3$ GHz. The second response, has a center frequency of $f_1 = 9$ GHz, and transmission zeros at $f_{z3} = 9.4$ GHz and $f_{z4} = 7.9$ GHz. The location of the transmission zeros

is dictated by the inductive and capacitive nature of the side perturbations. An inductive perturbation places one transmission zero closer to the lower side of the passband, while a capacitive perturbation places a transmission zero closer to the higher side of the passband. Also the spectral separation of the transmission zeros can be increased by moving the loading capacitive stubs closer to the upper right corner of the resonator. In this design, the fractional bandwidth is kept fixed at 4%. The tuning mechanism is accomplished by introducing switchable loading capacitors along the upper and right edge of the square patch. These capacitors are connected and isolated from the circuit via p-i-n diodes. The starting point of the design is a dual-mode microstrip square patch resonator with side dimension $a = 4 \text{ mm}$ ($\approx \lambda/4$). The first modification consists of a square cut of side dimension $c = 0.86 \text{ mm}$ ($\approx \lambda/20$), introduced at the left and lower sides of the patch to accommodate inserted ports for stronger couplings. A conventional patch perturbation with dimension $p = 0.5 \text{ mm}$ ($\approx \lambda/32$) is also introduced at the upper right corner causing the resonant frequencies of the degenerate modes to split. The next modification is a rectangular cut of sides $b = 2.1 \text{ mm}$ ($\approx \lambda/8$) and $d = 0.6 \text{ mm}$ ($\approx \lambda/26$), introduced on the upper and right sides of the patch. Sets of two switchable loading stubs are then placed inside the rectangular perturbation with length $s = 1.34 \text{ mm}$ ($\approx \lambda/12$) and with offset connecting points $o_1 = 0.68 \text{ mm}$ ($\approx \lambda/25$) and $o_2 = 0.33 \text{ mm}$ ($\approx \lambda/50$) measured from the center line of the patch. A set of four p-i-n diodes in series configuration connect and isolate these loading stubs, allowing the sides of the square to switch between an inductive and a capacitive type of perturbation. The high band state with center frequency $f_0 = 10 \text{ GHz}$ is produced when the diodes are off and the loading stubs are isolated. The low band state with $f_1 = 9 \text{ GHz}$ is produced when the diodes are forward biased. Symmetrical placement of transmission zeros is possible when the reactance of the inductive side cuts ($b \times d$) equals the reactance of the capacitive tuning stubs s . Although this state will not be implemented in this design, it is worth noting that this condition is met when $s = 0.95 \text{ mm}$ ($\approx \lambda/16$), and it produces a symmetrical response at 9.5 GHz .

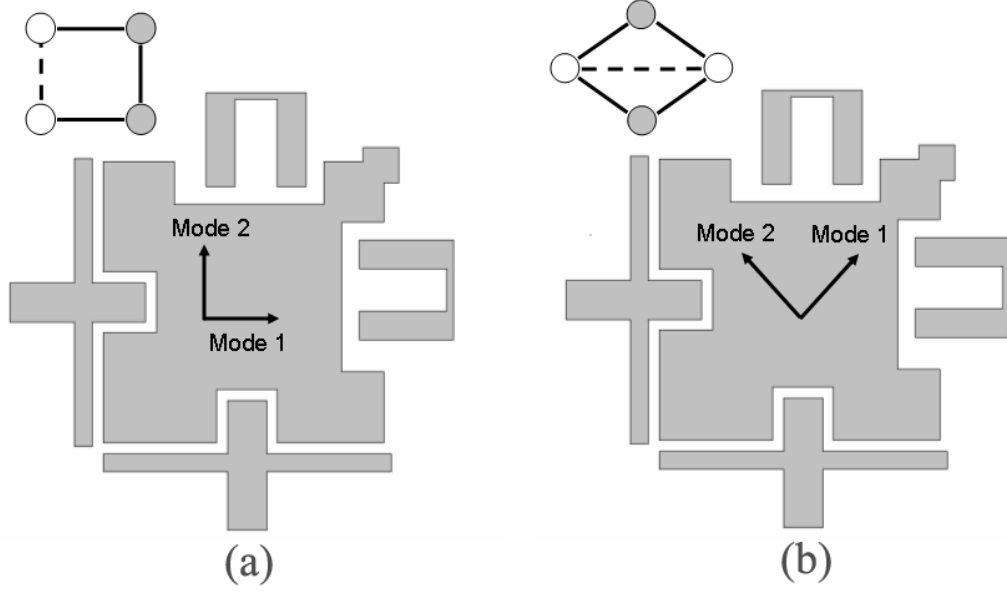


Figure 42. Polarization of degenerate modes. (a) conventional coupling scheme (b) coupling scheme with cross coupling

The conventional coupling scheme of a square patch topology is shown in Fig. 42a. The polarization of the modes in such arrangements means that the input is coupled to mode 1 while the output is coupled to mode 2. This conventional configuration shows no cross-coupling, and given the symmetry of the topology, asymmetric placement of transmission zeros is difficult if not impossible. On the other hand, if the modes are interpreted as having a 45° rotation as shown in Fig. 42b, a more appropriate coupling scheme is produced where the input and output ports are coupled to both modes. This coupling scheme was first pointed out in reference to a dual-mode square loop resonator [55]. Using such configuration the coupling matrix can be calculated analytically [50]. In such synthesis the transmission zeros are prescribed to meet the simulated response with an in-band return loss of 13 dB. The coupling matrix of each asymmetrical configuration using such results is given by

$$M_0 = \begin{bmatrix} 0 & 0.6252 & -0.5455 & 0.0352 \\ 0.6252 & -1.0200 & 0 & 0.6252 \\ -0.5455 & 0 & 1.0200 & 0.5455 \\ 0.0352 & 0.6252 & 0.5455 & 0 \end{bmatrix} \quad (28)$$

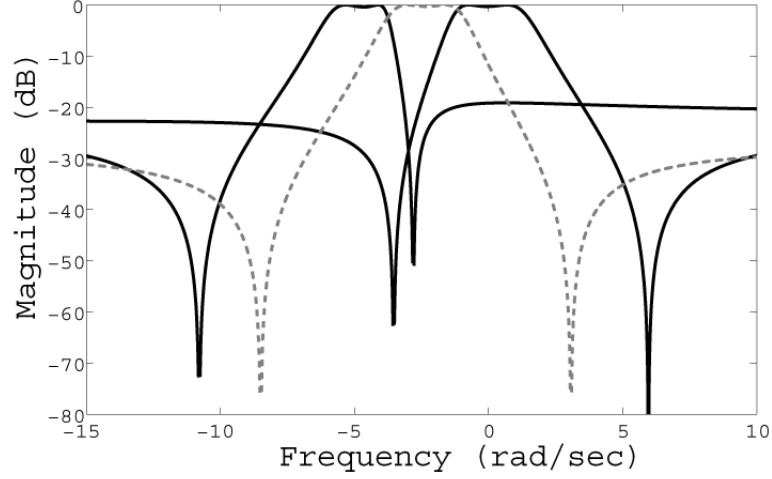


Figure 43. Frequency responses from coupling matrices M . Dotted line with symmetrical placement of zeros ($s = .95$ mm), M_0 ($s = 0$ mm) and M_1 ($s = 1.34$ mm) vs. angular frequency normalized to $f_0 = 10$ GHz

$$M_1 = \begin{bmatrix} 0 & 0.4370 & -0.5860 & 0.0380 \\ 0.4370 & 3.8012 & 0 & 0.4370 \\ -0.5860 & 0 & 5.8030 & 0.5860 \\ 0.0380 & 0.4370 & 0.5860 & 0 \end{bmatrix} \quad (29)$$

where M_0 corresponds to the high-band state ($f_0 = 10$ GHz) and M_1 corresponds to the low band state ($f_1 = 9$ GHz). The transmission and return scattering parameters for a fully canonical filtering function can be expressed in terms of a coupling matrix M [50] as shown in equations (3) and (4)

$$S_{21} = -2j[-jR + \omega W + M]_{4,1}^{-1} \quad (30)$$

$$S_{11} = 1 + 2j[-jR + \omega W + M]_{1,1}^{-1} \quad (31)$$

where $R \in \mathfrak{R}^{4 \times 4}$ is a zero matrix except for $R_{1,1} = R_{4,4} = 1$. $W \in \mathfrak{R}^{4 \times 4}$ is also a zero matrix except for $W_{2,2} = W_{3,3} = 1$. Fig. 43 shows the responses produced by the coupling matrices normalized with respect to $f_0 = 10$ GHz.

Loading the sides of the resonator walls produces a shift in the resonant frequencies of the two modes. This frequency displacement can be seen between $M_0(2,2)$ and $M_1(2,2)$

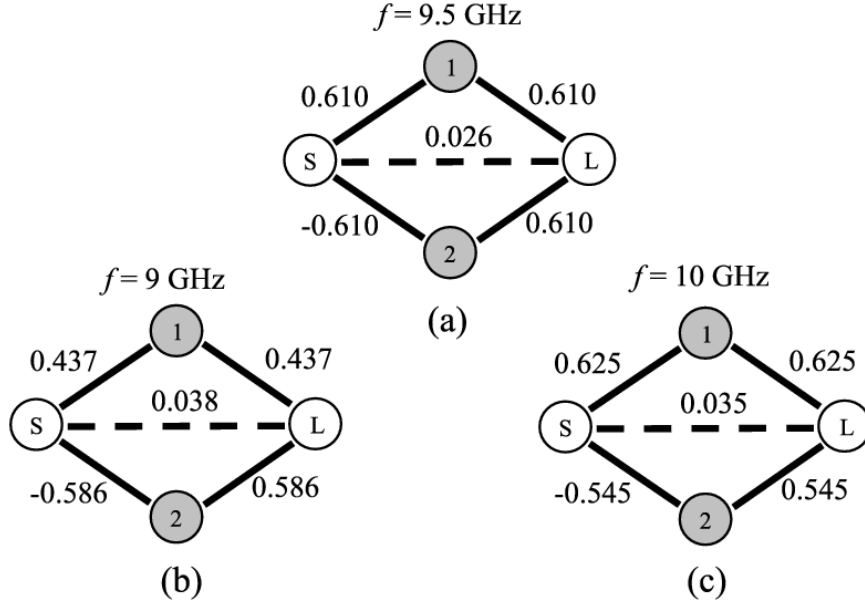


Figure 44. Coupling matrix schematic (a) Symmetrical placement of zeros with $s = .95$ mm and $M(2, 2) = 1.32$, $M(3, 3) = 3.42$. (b) M_1 with $s = 1.34$ mm. (c) M_0 with $s = 0$ mm.

for mode 1, and between $M_0(3, 3)$ and $M_1(3, 3)$ for Mode 2. Also, a constant fractional bandwidth is achieved by optimizing the perturbation size p , and meeting the condition $M_0(2, 2) - M_0(3, 3) \approx M_1(2, 2) - M_1(3, 3)$. Referring to the coupling schematics in Fig. 44(a), it is seen that symmetrical placement of transmission zeros is achieved with equal magnitude coupling coefficients between resonators and ports. Fig. 44(b), and Fig. 44(c), show that the coupling between mode 2 to both the source $M_0(1, 3)$ and load $M_0(3, 4)$ remained approximately constant. On the other hand, the coupling from mode 1 to the source and load port decreases when the tuning stubs are connected to the resonator. This can be seen in $M_1(1, 2) < M_0(1, 2)$.

The substrate used was Rogers Duroid, with $\epsilon_r = 10.2$ and $\tan \delta = 0.0025$. The substrate thickness is 25 mils with 0.5 OZ of copper metallization. The diodes are ASB 8000 by ASI. The filter was fabricated using standard photolithography. A picture of the fabricated filter is shown in Fig.45. The size of the circuit including the CPW to microstrip transitions, for on wafer probing, is about 15 mm x 15 mm. The DC bias lines are designed as RF chokes and consist of a high impedance transmission line terminated in an open radial stub

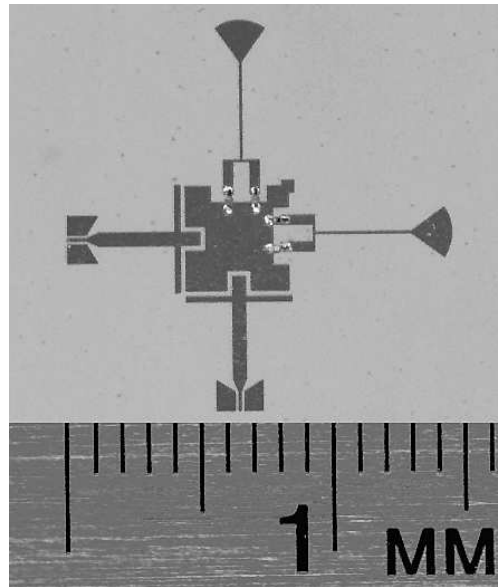


Figure 45. Picture of Fabricated Filter.

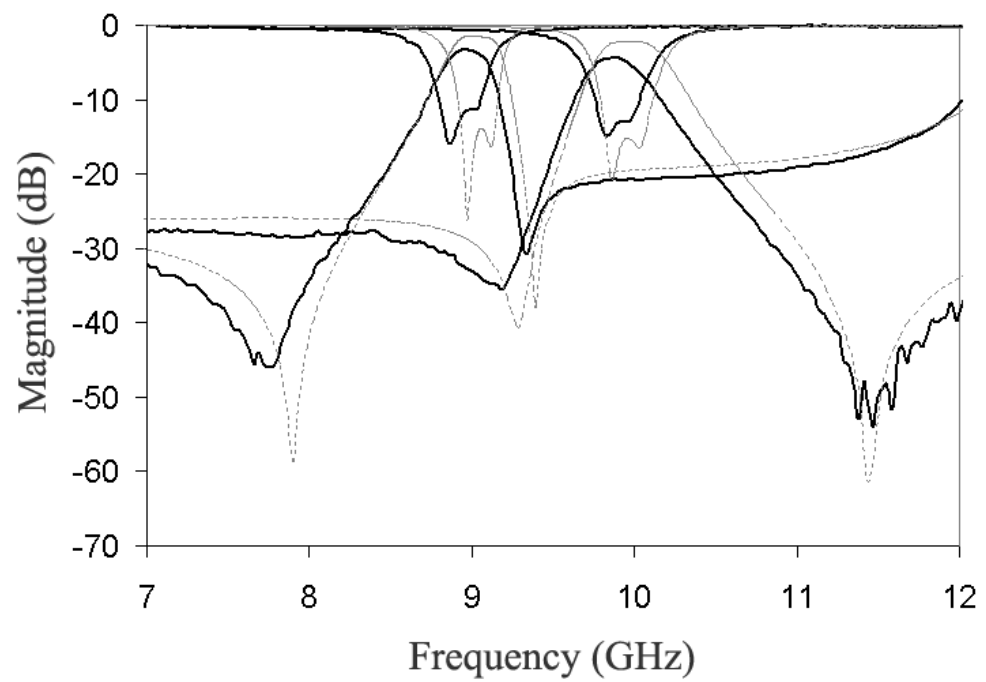


Figure 46. Measured (solid line) and simulated (dotted line) S21 and S11 parameters .

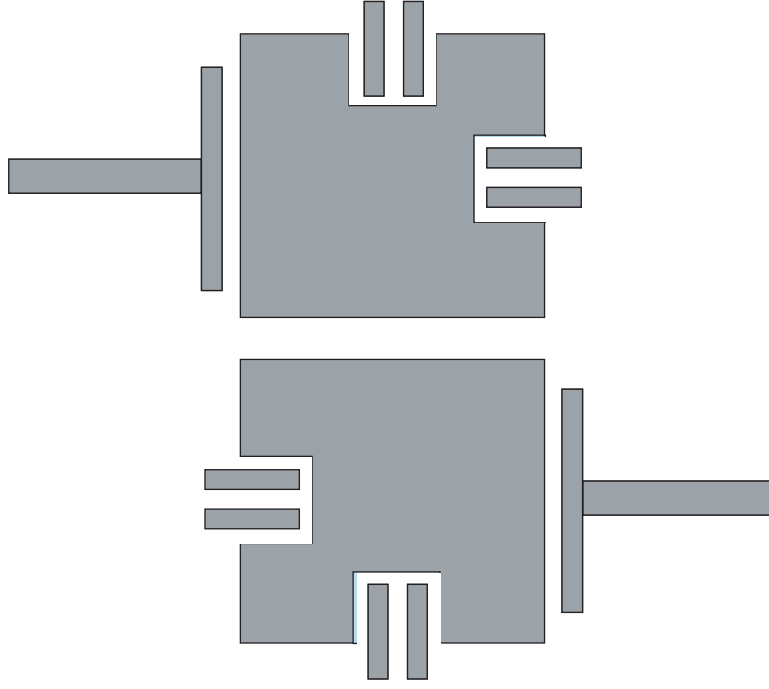


Figure 47. Resonator configuration for higher order tunable filter realizations

for a total effective length of $\lambda/2$. A lumped element model of the diode was included in the simulations as a $3\ \Omega$ resistor for the forward biased state and $0.025\ \text{pF}$ capacitor for the isolation state. The forward bias current was limited to $I_f = 30\ \text{mA}$ and the reverse bias voltage was $V_r = -10\ \text{V}$. Full wave simulations were conducted using the software packages Agilent Momentum and Sonnet 10.52. The simulated and measured S21 and S11 parameters of the filter are shown in Fig.46. Very good agreement can be observed between the measured and simulated frequency profile of the filter. The measured insertion loss of the low band state was $3.25\ \text{dB}$ with center frequency of $8.92\ \text{GHz}$, while the insertion loss of the filter in the high band state was $3.65\ \text{dB}$, with center frequency of $9.87\ \text{GHz}$.

It is worth noting that $M_1(1, 2) < M_0(1, 2)$ suggests a degree of over coupling between mode 1 and the input/output ports of the high band state. This condition forces a lower resonator quality factor Q_e yielding a higher insertion loss in the filter with $f_0 = 10\ \text{GHz}$. The loss introduced by the $3\ \Omega$ series resistance of the diodes mainly affects the low band state. However, it is well known that parallel resistive combinations, caused by the side to side placement of the diodes, reduce resistive loss in the on state and increases parasitic

capacitances in the off state. The frequency shifts are within fabrication tolerances and are partially attributed to parasitic capacitances introduced by the p-i-n diodes. The fractional bandwidths remained approximately constant with 3.74 % for the low band stated, and 3.89 % for the high band state. The measured transmission zeros are located at $f_{z1} = 11.4$ GHz, $f_{z2} = 9.1$ GHz and $f_{z3} = 9.3$ GHz and $f_{z4} = 7.7$ GHz.

Filters with higher order are also possible using the standard cascaded configurations. Fig.47 shows a conceptual four pole reconfigurable filter. It is worth noting that as the order of the filters increases, the placement of the transmission zeros will also become more difficult to control. Some applications may required higher order tunable filters to increase the isolation between different frequency channels.

5.3 Chapter Summary

A bandpass filter design using a dual-mode microstrip triangular loop resonator was successfully demonstrated. The circuit produces frequency responses with one real finite frequency transmission zero and one imaginary finite frequency zero on either side of the passband. Depending on the perturbation arrangement, the nature of the coupling between degenerate modes causes the zeros to exchange their axis locations from real to imaginary and from imaginary to real while keeping their magnitude. This behavior results in frequency responses that are suitable for applications with asymmetrical requirements. Results show 8% bandwidth filters with insertion loss ranging from 0.82 dB to 1.4 dB at 10 GHz. Advantages in size reduction and design flexibility are demonstrated when the triangular loop is compared to other dual-mode resonators.

Tunable filter topologies capable of producing asymmetrical responses where also presented in this chapter. A prototype filter topology was designed with several fixed and switchable perturbations to control the center frequency and the location of the transmission zeros. The tuning mechanism consists of capacitively loading the edges of a modified square patch resonator, in order to manipulate the current distribution of the degenerate

modes. This operation results in asymmetrical responses with center frequency tuning ratio of 10% at X band, and angular transmission zero displacement of $\Delta\omega_z = 3.5$ rad/sec or greater in both lower and higher side of the passband.

CHAPTER 6

FERROELECTRIC FILTERS AND MEMS SWITCHES

This chapter reports a hybrid tunable filter topology in mm-wave range that combines ferroelectric capacitors and MEMS switches. Ferroelectric materials such as the Barium Strontium Titanate (BST) presented here show high controllable characteristics making them an attractive technology and a major factor in the future generation of tunable components. This work also demonstrates for the first time, a bandwidth tuning scheme that uses MEMS cantilevers to control inter-resonator coupling in a coplanar wave guide (CPW) configuration.

6.1 Continuous Tuning using Ferroelectric Capacitors

Schematics of the proposed second and third order filters are shown in Fig. 48(a). and Fig. 48(b). respectively. The filters are designed using a CPW end coupled resonator topology, with a system impedance $Z_0 = 50 \Omega$. Given the single plane for signal and ground, this

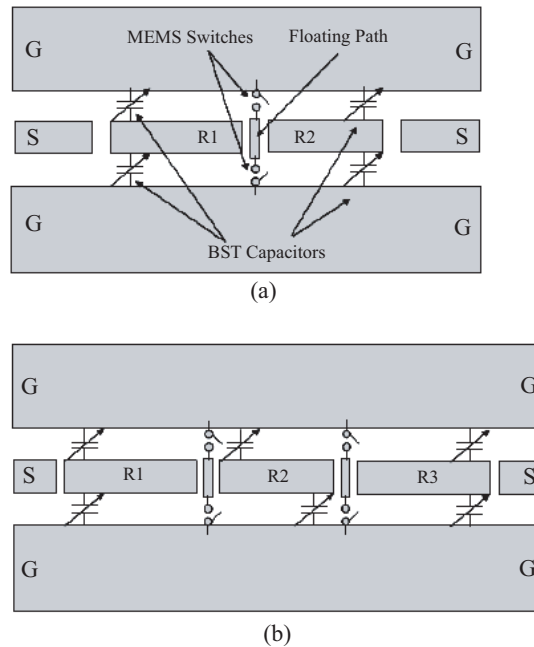


Figure 48. Proposed filter schematic. (a) 2pole filter. (b) 3-pole filter.

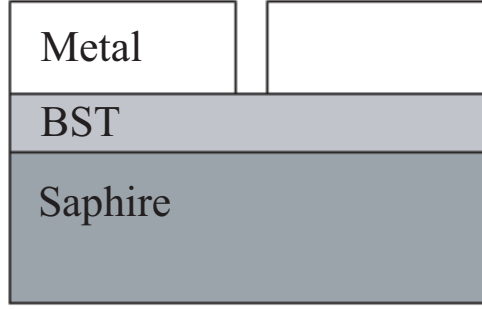


Figure 49. Cross section of a BST gap capacitor (not to scale).

topology avoids the need of via holes and greatly facilitates the introduction of tunable elements such as loading BST capacitors and MEMS switches. The resonator lengths are approximately $\lambda_g/2$ where λ_g is the guided wavelength at the design center frequency $f_0 = 40$ GHz. The goal is to produce a chebychev bandpass filter with continuously tunable center frequency and adjustable fractional bandwidth.

Initially, the filter is analyzed with unloaded resonators. The absence of BST loading capacitors produces the conventional resonant poles with a center frequency, $f_0 = 40$ GHz, and resonator length, $L = \lambda_g/2$. Frequency control is achieved when the shunt variable BST capacitors are added at the resonator ends. These capacitors effectively increase the electrical length of the resonators causing a frequency shift in the resonant poles to approximately $f_{Min} = 30$ GHz with a zero bias voltage ($V_{bias} = 0V$). Consequently, when the capacitors are biased, the center frequency shifts to higher frequencies, $f_{Max} = 35$ GHz, until a saturation voltage point at $V_{bias} = 40V$. Hence, the loading capacitor values are strategically varied when an applied DC voltage ($V_{bias} = 0V - 40V$) changes the dielectric constant of the BST film. This tuning procedure changes the center frequency of the filter in a continuous fashion.

The BST capacitors were designed using a planar configuration, i.e. metallization was carried out after the BST deposition, see Fig. 49. The planar configuration requires fewer lithography steps and enables thicker metal to be deposited for lower metal losses. Most importantly, epitaxial BST thin films can be grown on single crystal substrates ensuring

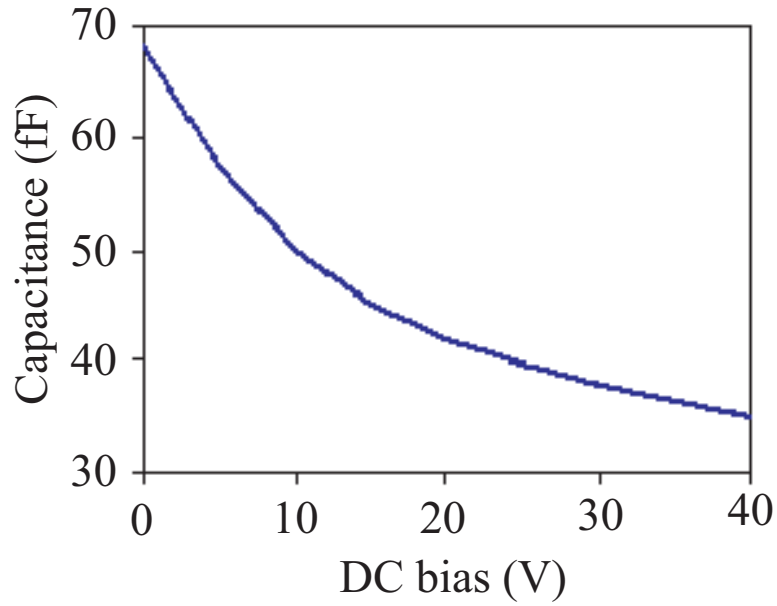


Figure 50. Capacitance versus bias voltage of a BST gap capacitor.

lower dielectric losses. In order to reduce the DC bias voltage, the recently developed interdigitated capacitor structures [78] were employed at a 1 micron separation. The tuning voltage can be reduced by decreasing the separation. In these structures, the DC bias line is separated from the RF signal by using a highly resistive thin layer of material (e.g., Indium Tin Oxide or ITO).

Important characteristics of a thin film BST capacitor include tunability, Q , and dielectric constant of the BST. Studies have shown that these electrical properties are strongly affected by crystalline structure, microstructure, dopants, composition, and its thickness of the BST films, as well as electrode material and thickness. Numerous groups have attempted different growth techniques to improve BST film quality, such as pulsed laser deposition [79], metal-organic chemical vapor deposition [80], sputtering [81], and sol-gel [82]. nGimat has developed its proprietary Combustion Chemical Vapor Deposition (CCVD) process [83] for depositing epitaxial BST films on sapphire that provide the building blocks for a host of and the loss tangent $\tan \delta$ was better than 0.05. The tunability of the capacitor was recorded at 1 MHz using a precision LCR meter, as illustrated in Fig. 50.

The capacitance at zero bias is 68 fF, which reduces to 35 fF at 40 V. By varying the capacitor lengths and gap widths, one can achieve different capacitances and tunability, which will yield filters with various tunable frequency ranges.

6.2 Bandwidth Control using MEMS Switches

The spectral separation of the resonant poles in edge coupled resonator filters is directly related to the inter-resonator coupling strength. The coupling between adjacent resonators is due almost entirely to the fringing electric field produced at the resonator edges. A mechanism to control the interresonator coupling is achieved by a switchable structure that effectively changes the amount of electric field energy coupled from one resonator to the next. This procedure is equivalent to a waveguide adjustable iris and it is demonstrated in a CPW configuration for the first time.

The tuning structure consists of a conductive path placed between adjacent resonators. As shown in Fig. 51, this conductive path is connected or isolated to the ground planes using a set of MEMS switch cantilevers. Fig. 52 shows the simulated responses of the 2-pole filter in the wideband and narrowband states. The tuning mechanism is analyzed here at $f = 42.5$ GHz corresponding to a pole location in the wideband response and a 10 dB rejection at the narrowband response. A full wave simulation is conducted using *Sonnet* 10.52. The simulation emulates the down state of the MEMS switches using a perfect short, and the up state of the MEMS switches using a perfect open. Fig. 53 shows the current densities of the 2-pole filter at $f = 42.5$ GHz, in both the wideband state (MEMS switches up), Fig. 53a, and narrowband state (MEMS switches down), Fig. 53b. When the conductive path is isolated, it functions as a floating metal having little to no effect in the electric field coupling between resonators; this can be seen in Fig. 53a, where the floating path shows a near zero current density while the resonators show a high current density. This configuration produces the highest inter-resonator coupling strength which translates into a wideband state. A wideband filter characteristic is achieved when the resonant poles

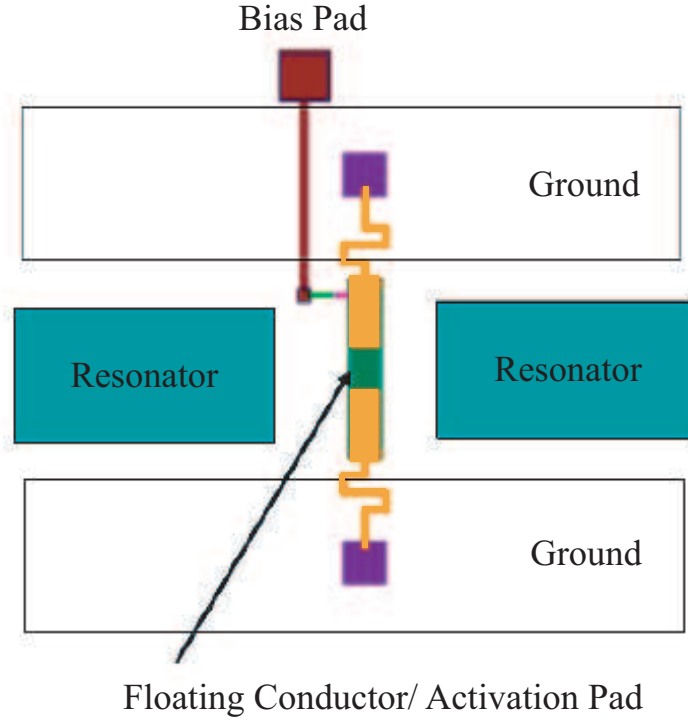


Figure 51. Layout of MEMS tuning mechanism for bandwidth control.

are placed farther away from each other producing a broader inband frequency profile. The second configuration of the filter is produced when the MEMS cantilever are in the down state. At this point, the conductive path is grounded as it is connected to the CPW ground planes. This grounded conductive path effectively contains the amount of electric field energy at the resonator edges reducing the inter-resonator coupling. Fig. 53b shows a higher current density at the conductive path and an attenuated current density at the resonators. This configuration produces the narrowband state of the filter by grouping the resonant poles closer together across the passband. A fractional bandwidth of the filters can be adjusted to a tuning ratio of 2:1 for 2nd order filters and 2.5:1 for 3rd order filters.

The pull-in voltage of MEMS switch can be calculated from the effective spring constant of the membrane support as:

$$V_{pull-in} = \sqrt{\frac{8K_{eff}g^3}{27A\epsilon_0}} \quad (32)$$

where K_{eff} is the effective spring constant of the membrane, g is the initial gap between the

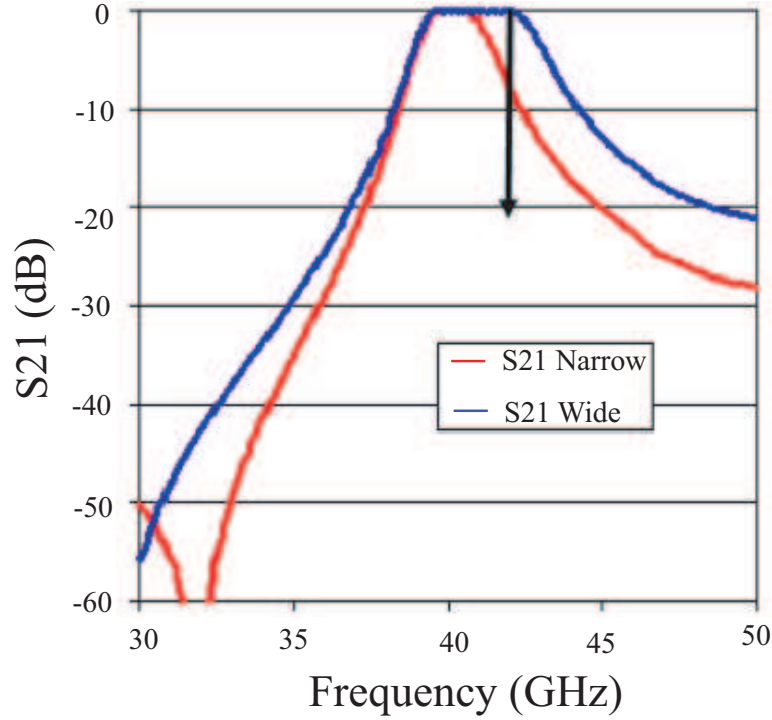


Figure 52. Simulated response. Marker at 42.5 GHz corresponds to a pole location in the wideband response and a 10 dB rejection in the narrowband response.

switch and the bottom electrode, A is the area of the membrane, and ϵ_0 is the permittivity of air. When designing for low actuation voltage, choice of the membrane material and support design is critical. In order to lower the pull-in voltage of the structure, three different ways can be used: (1) increasing the area of membrane, (2) diminishing the gap between the switch and bottom electrode, and (3) designing a structure with low spring constant. In the first case, the area can only be increased by so much before device size becomes a prevailing issue. In the second case, the return loss associated with the RF signal restricts the value of the gap. The third case is the one with the most flexibility since the design of the springs does not considerably impact the size, weight, and/or RF performance of the circuit. To reduce the actuation voltage, MEMS cantilevers in this paper were designed with a meander shape support. The effective spring constant of a meander shaped structure as shown in Fig. 54 is given by:

$$K_{eff} = \frac{E_w \left(\frac{t}{L_c}\right)^3}{1 + \frac{L_s}{L_c} \left[\left(\frac{L_s}{L_c}\right)^2 + 12 \left(\frac{1+\nu}{1+(\frac{w}{t})^2}\right) \right]} \quad (33)$$

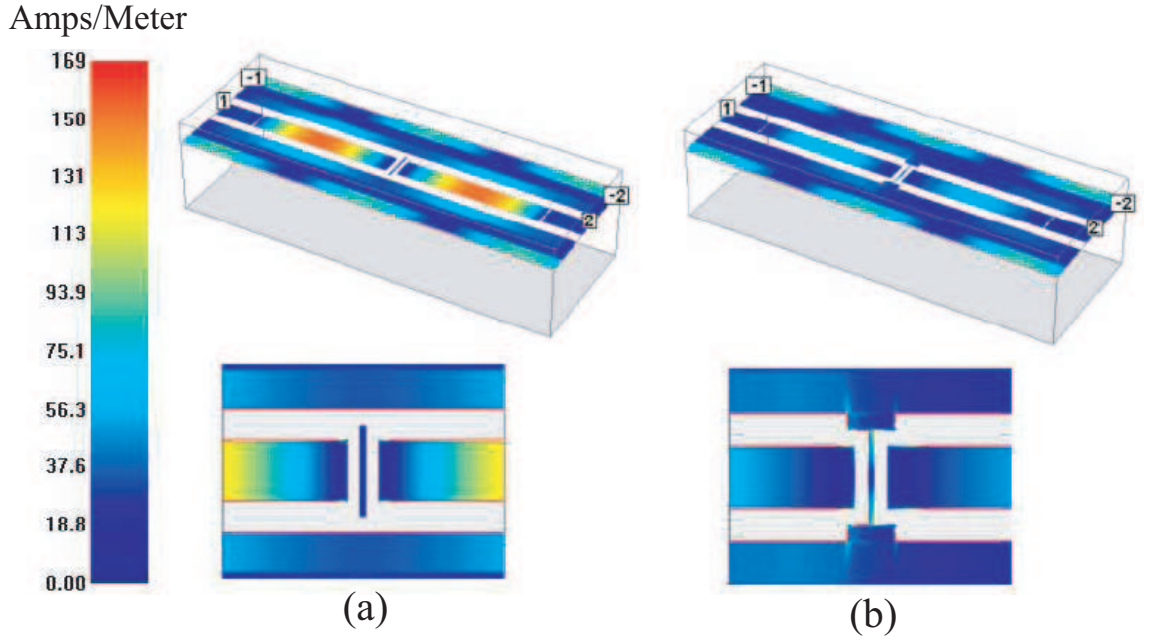


Figure 53. Current density distribution at 42.5 GHz (a) Wideband state. (b) Narrowband state.

where E and ν are the Young's modulus and the Poisson's ratio, respectively. The spring constant for N of such structures connected in series and parallel are K_{eff}/N and NK_{eff} respectively. For switches that use gold for the cantilever material the expected pull-in voltages are in the range of 20-30 V. In addition, actuation voltage simulation for the designed switch with the meander shape support is also done using FEMLAB, and the result showed that the actuation voltage was around 30V.

The BST films were epitaxially grown on r-plane sapphire substrates using nGimats proprietary CCVD process [84],[85], After CCVD deposition, the BST films were patterned using a diluted HF solution, following which high resistive bias lines were deposited and patterned by wet etching. Metallizations were then carried out using a lift-off process to form the capacitors, the CPW lines, and the activation pads for the MEMS switches. A Ti/Cu/Au metal stack was used with a total thickness of $2\ \mu\text{m}$ for the former two structures and $0.8\ \mu\text{m}$ for the latter. The filter was later passivated using BCB photosensitive polymers. The last step before MEMS fabrication was a metal layer forming the bias pads and lines, which were on top of the BCB layer. For the MEMS switches, a 300 nm thick

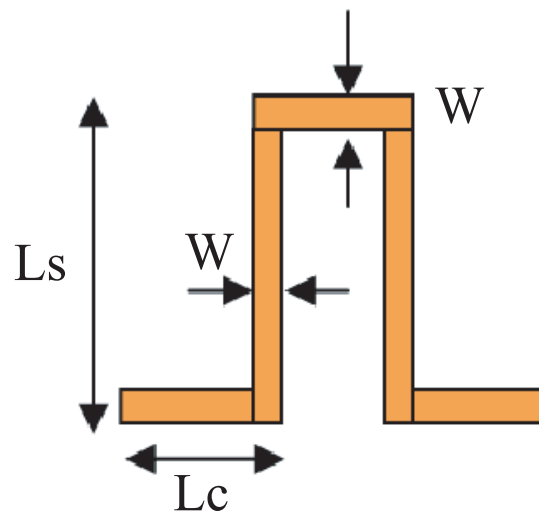


Figure 54. Geometry of the meander-shaped support.

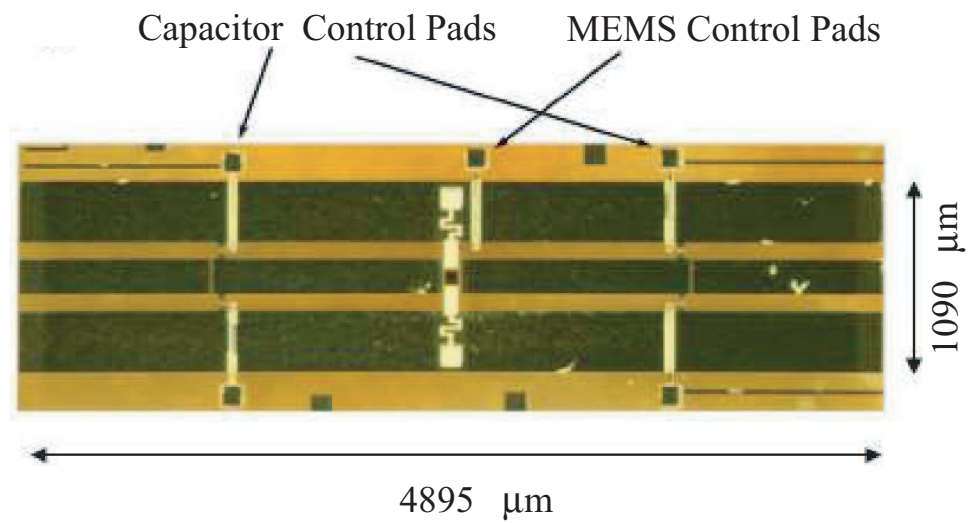


Figure 55. Picture of fabricated filter.

Si_3N_4 layer was first deposited using PECVD, patterned and etched with RIE between the membrane and the signal line. Then a $1.8\ \mu\text{m}$ thick photoresist 1813 was spin coated and patterned to create the air-gap. Ti/Au/Ti ($300\ ^\circ\text{A}/3000/300\ ^\circ\text{A}$) seed layer was then evaporated and patterned and electroplated to a thickness of $3\ \mu\text{m}$ to form the switch membrane. Finally, after removing the sacrificial photoresist layer with a resist stripper, a critical point drying process was used to release the switches. Fig. 55 shows a picture of the fabricated 2-pole filter.

Conventionally, a capacitive coupled resonator filter would require different critical coupling at the ports. This can be accomplished with a design that includes a variable capacitor connecting the input port to the first resonator and the output port to the N^{th} resonator. This option requires an added degree of complexity and it has been avoided in this design. Since the port couplings are fixed, a simulation has been conducted to model the deterioration of the response due to port mismatch and due to the loss of the BST capacitors. The BST loss tangent varies from $\tan\delta=0.05$ at ($V_{\text{bias}} = 1\text{V}$) and capacitance of 68 fF to $\tan\delta=0.005$ at ($V_{\text{bias}} = 40\text{V}$) and capacitance of 35 fF. A full wave simulation was conducted on the 2 pole filters including these capacitor characteristics. Fig. 56 shows the passband and return loss degradation for the lower frequency cases.

The filters were measured using an Agilent HP 8510 vector network analyzer. An on-wafer short, open, load, and through (SOLT) standard was used for calibration. The wideband and narrowband 2-pole filter measured results are shown in Fig. 57 through Fig. 60. The insertion loss of the wideband state ranges from 9 dB ($V_{\text{bias}} = 1\text{V}$) to 2.7 dB ($V_{\text{bias}} = 40\text{V}$). The mid-band return loss was 4 dB for biasing voltages below 5V and 8 dB or better for the remaining cases. The narrowband state yielded an expected higher loss ranging from 16 dB ($V_{\text{bias}} = 1\text{V}$) to 5 dB ($V_{\text{bias}} = 40\text{V}$). The return losses ranged from 7 dB for biasing voltages below 5V and 15 dB or better for higher voltages. The fractional bandwidth of the 2-pole filter averaged 9.6 % for the wideband state and 4.8 % in the narrowband state. The bandwidth of the 3-pole filters resulted in 7.8 % and 3.1 % for the

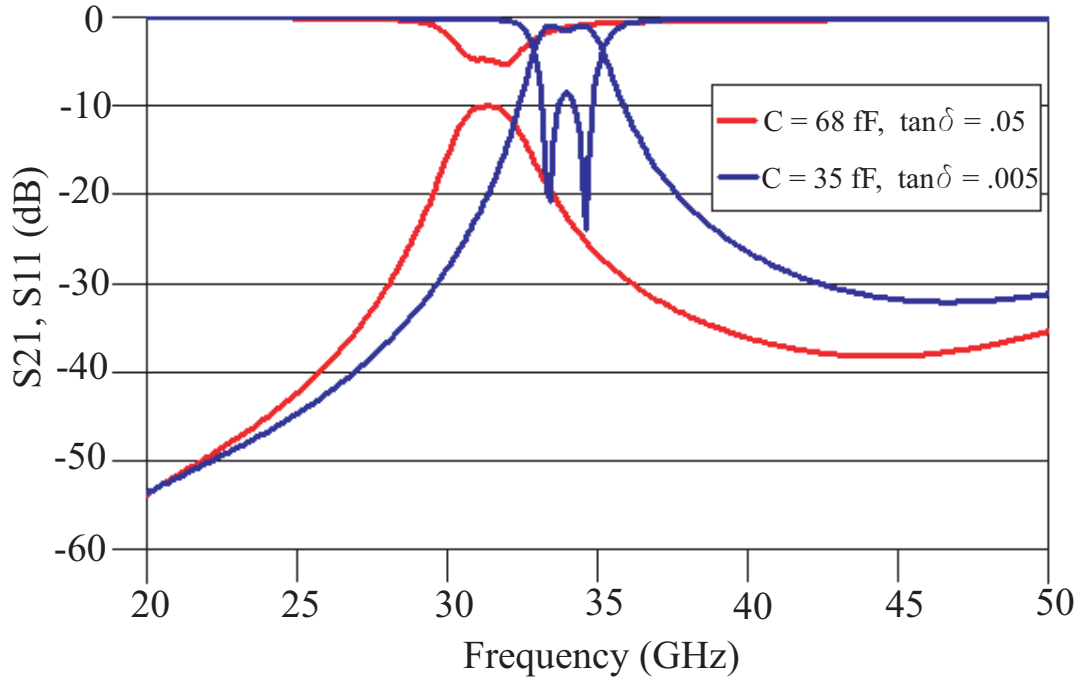


Figure 56. Effect of fixed input/output coupling and BST loss on filter response.

wideband and narrowband respectively. The third order filter wideband and narrowband measurement results are shown in Fig. 61 through Fig. 64. The wideband state yielded an insertion loss of 16 dB ($V_{bias} = 1V$) and 6 dB ($V_{bias} = 40V$). The return loss was better than 7 dB for all voltage cases. The narrowband state resulted in insertion losses of 19 dB ($V_{bias} = 1V$) and 8 dB ($V_{bias} = 40V$). The return loss was 8 dB or better for all biasing voltages. As discussed before, the high insertion and return loss is attributed to conductor losses, fixed input/output port couplings and the thin film BST loss at the different biasing voltages. In order to reduce loss and improve performance of tunable devices, efforts have been made to explore novel materials such as Bismuth Zinc Niobate [86] and optimize the electrode structure of BST capacitors [87]. Also, the filter loss could be further reduced if a better return loss is achieved.

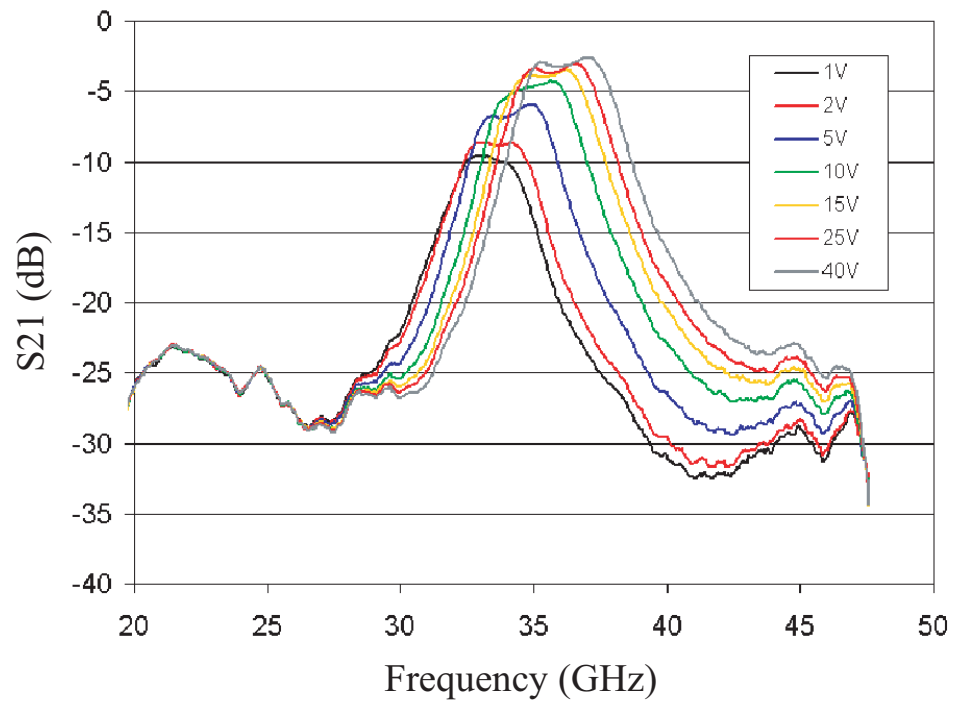


Figure 57. Transmission loss of 2-pole filter measured wideband state (MEMS switches up).

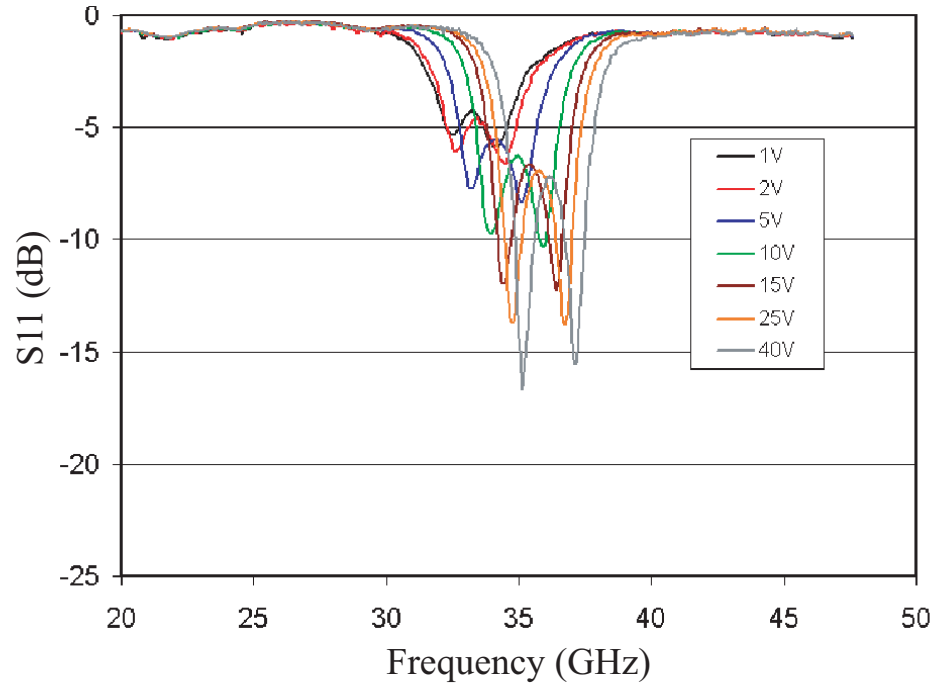


Figure 58. Return loss of 2-pole filter measured wideband state (MEMS switches up).

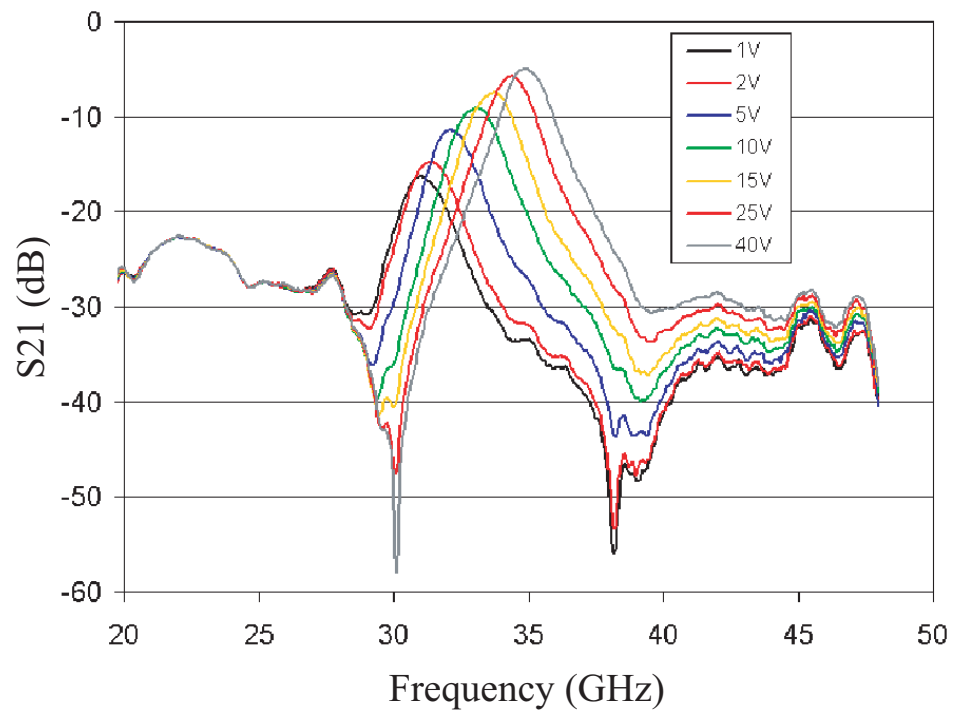


Figure 59. Transmission loss of 2-pole filter measured narrowband state (MEMS switches down).

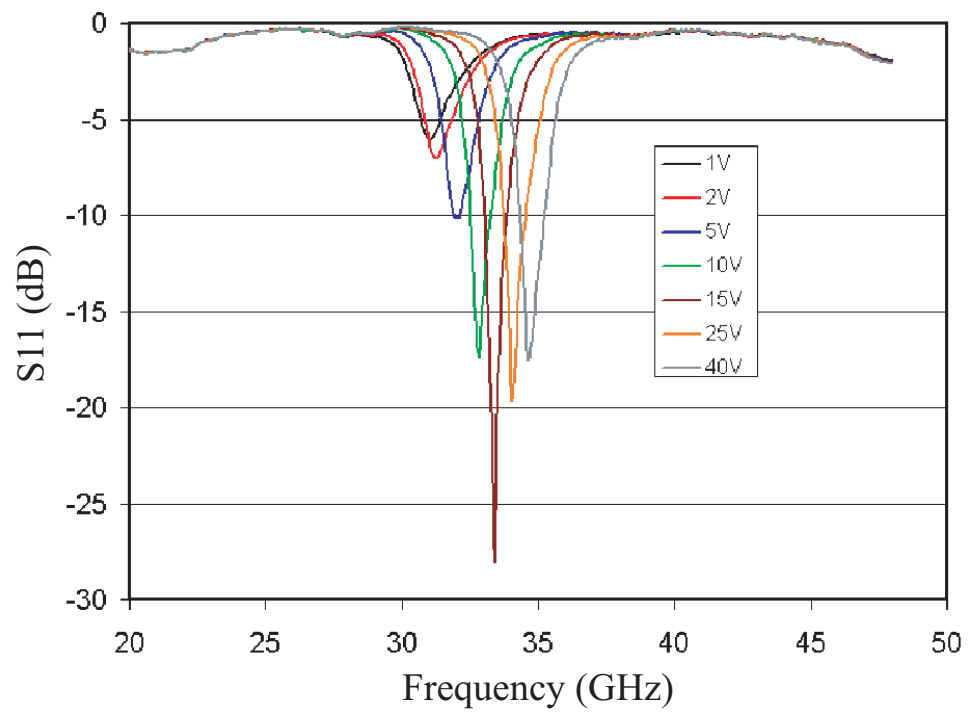


Figure 60. Return loss of 2-pole filter measured narrowband state (MEMS switches down).

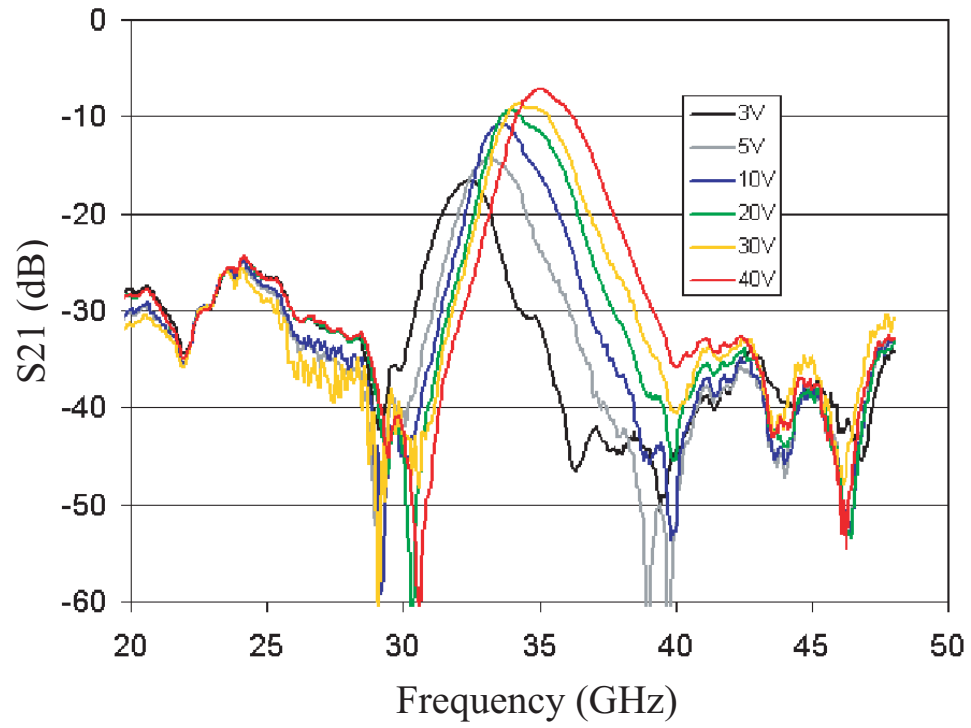


Figure 61. Transmission loss of 3-pole filter measured wideband state (MEMS switches up).

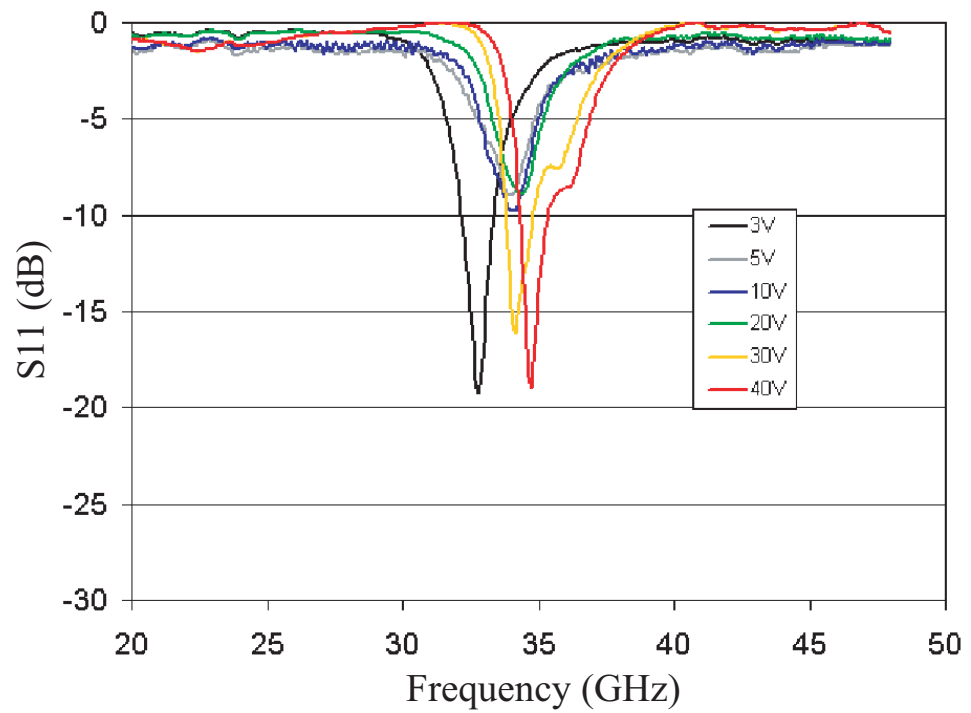


Figure 62. Return loss of 3-pole filter measured wideband state (MEMS switches up).

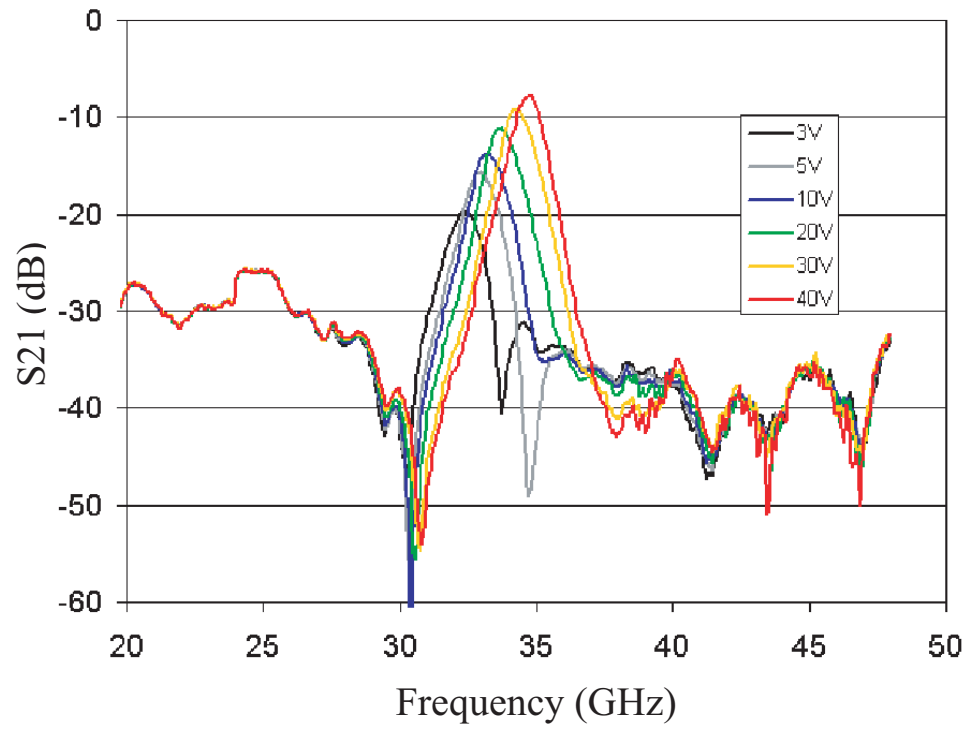


Figure 63. Transmission loss of 3-pole filter measured narrowband state (MEMS switches down).

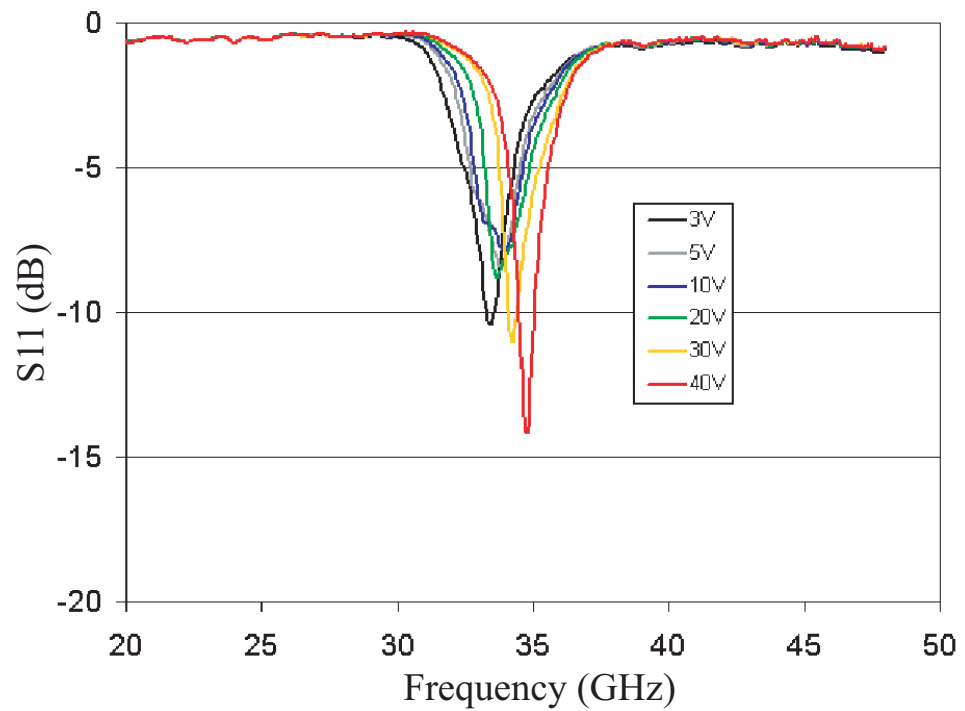


Figure 64. Return loss of 3-pole filter measured narrowband state (MEMS switches down).

6.3 Chapter Summary

This chapter reports the first tunable bandpass filter with simultaneous frequency and bandwidth control using a combination of ferroelectric Barium Strontium Titanate (BST) capacitors and cantilever MEMS switches. The center frequency of the filter was tuned in a continuous fashion from 30 - 35 GHz with insertion loss ranging from 10 to 2.7 dB. Also the fractional bandwidth of the filter can be independently controlled by a tuning scheme that uses MEMS switches to vary the inter-resonator coupling. The 2 pole filter prototypes resulted in fractional bandwidths of 9.6 % (wideband configuration), and 4.8 % (narrowband configuration) for a tuning ratio of approximately 2:1. The third order filters resulted in bandwidths of 7.8 % (wideband configuration) and 3.1 % (narrowband configuration) for a passband tunable ratio of approximately 2.5:1.

CHAPTER 7

PLANAR REALIZATION OF A TRIPLE-MODE FILTER

For years, multi-mode resonators have been used in filter synthesis for their ability to reduce the number of resonating elements. Waveguide dual-mode filters have been extensively designed for satellite applications [89] and cellular base stations [90]. Multi-mode attractive characteristics include, high performance in response selectivity, inherent size reduction, and advanced elliptic or quasi-elliptic responses with asymmetrical characteristics. Triple-mode filters have been reported using dielectric filled waveguide resonators of rectangular and cylindrical shape. For the most part, triple mode operation is achieved by a dielectric filled structure inside a resonant metal cavity. This cavity is then perturbed using tuning and coupling elements such as screws or metal rods [91]. Mode degeneracy occurs when different cavity modes resonate at the same frequency. In this situation, it is necessary for each mode to produce a distinct field pattern. This allows the coupling elements to interfere with the field paths differently from mode to mode and produce a split in the resonant frequencies.

The modes TM_{101} , $TM_{10\delta}$, TE_{101} , $TE_{10\delta}$ and the hybrid $HEM_{10\delta}$ have been used extensively in the past [90]-[93]. The electromagnetic problem of dual-mode resonance has been successfully translated from waveguide realizations to planar technology. This has produced a range of microstrip patches and loops of circular [63], square [55] and triangular shapes [52]. However, one disadvantage in planar dual-mode resonators is their loss. This is attributed to conductor loss, radiation loss, and excitation feed coupling. Despite efforts to improve dual-mode performance [94], single-mode resonators usually result in lower loss (about 2 dB in some cases) [95]. This leaves selectivity and size reduction as the sole advantage in planar dual-mode filters. A triple mode resonator is difficult to realize in planar form. This is due to all of the inherent three dimensional requirements. For example, the tuning and coupling elements used for modal coupling are for the most part, required

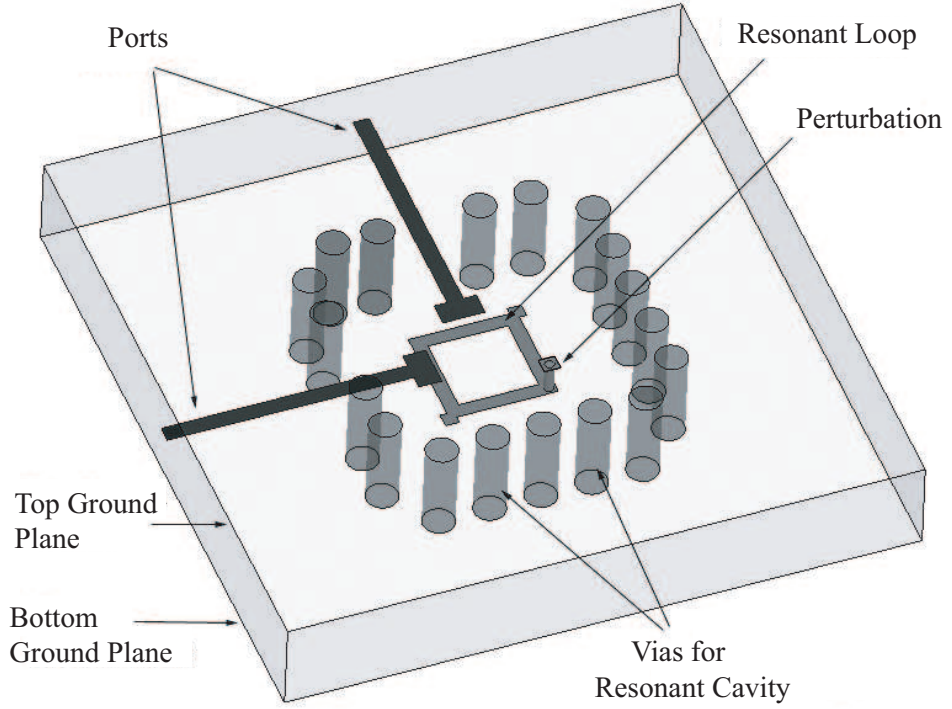


Figure 65. Proposed topology.

to exist at angles that perturb the modes in all three dimensions. For this reason, triple mode filters have only been accomplished in waveguide form. In this work, a multilayer approach is proposed for the first time to produce a triple mode resonator. To the best of our knowledge, this filter represents the first triple mode filter in planar configuration. The resulting prototype approaches the performance of waveguide filters in terms of loss, while keeping a compact size profile comparable to standard planar filters.

7.1 Multilayer Approach for Third Order Degeneracy

The proposed topology is shown in Fig. 65. The main resonant element consists of a square loop resonator placed inside a resonant metal cavity. The resonant loop closely follows the conventional design of a microstrip dual-mode square loop resonator [55] with side dimensions of $\lambda_g/4$ where λ_g is the guided wavelength at the resonant frequency f_0 . The input/output ports are placed at a 90° excitation angle with line width corresponding to a strip transmission line with characteristic impedance $Z_0 = 50 \Omega$. Fig. 66 shows the side

view and the different layers of the filter. The filter was designed using 4 dielectric layers ($\epsilon_r = 10.2$) of various thickness constituting the different horizontal levels $z = 0$ mil, 50 mil, 75 mil, 100 mil, and 150 mil. The metal layer ($z = 0$ mil) corresponds to the bottom ground plane. The resonant loop is located at $z = 50$ mil and the ports are placed at $z = 75$ mils. A set of perturbations are introduced in all three dimensions by placing a square patch on a higher layer ($z = 100$ mil) with dimensions extending in the x-y direction. This patch is then connected to the resonant loop using a metal via extending vertically between layers $z = 50$ mil and $z = 100$ mil. As it will be discussed in detail, this set of perturbations are responsible for the split in resonant frequencies of three degenerate modes.

The initial cavity dimensions are calculated using the eigenmode solver in the software package HFSS. The eigenmode frequencies of the dielectric filled cavity alone (without resonant loop or ports present) are investigated with dimensions $z = 150$ mil (total layer thickness) and $x = y$. The wave number k_{mnl} and resonant frequency f_{res} for a lossless rectangular waveguide cavity with resonant modes TE_{mnl} and TM_{mnl} are given by

$$k_{mnl} = \sqrt{\left(\frac{m\pi}{x}\right)^2 + \left(\frac{n\pi}{y}\right)^2 + \left(\frac{l\pi}{z}\right)^2} \quad (34)$$

$$f_{res} = \frac{ck_{mnl}}{2\pi\sqrt{\epsilon_r}} \quad (35)$$

c is the speed of light. In this first analysis we seek the dimensions x and y that produce the lowest resonant mode at a frequency of $f_0 = 5.8$ GHz. Planar resonant square loops are treated as waveguide cavities with dual mode operation expanded by the degenerate modes T_{mn0}^z , where z is perpendicular to the ground plane.

A natural choice for the cavity dimensions is to find the dominant resonant mode TM_{110}^z . Setting $f_{res} = f_0$ in equation (2) with $m = 1, n = 1, l = 0$ the dimensions of the cavity are found to be $x = y = 450$ mil. This initial calculation has no dependency on z or total height H of the cavity. The z dimension is deliberately chosen to be $z = \lambda_g/4$ and an appropriate solution is found for the triple mode operation. As will be shown later in the discussion,

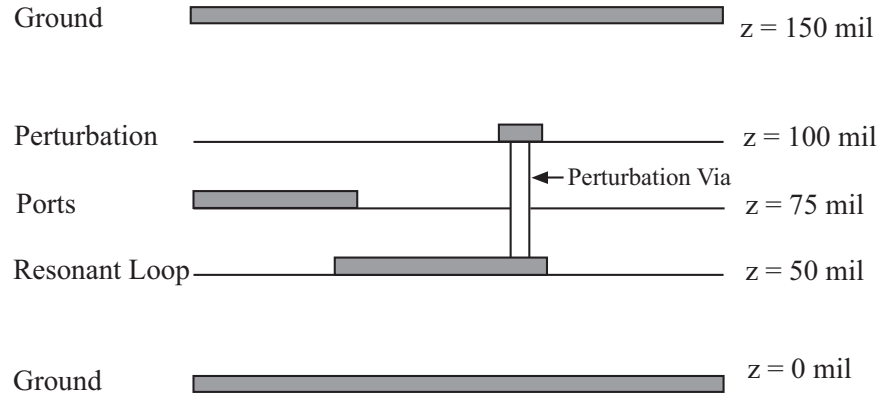


Figure 66. Filter cross-section.

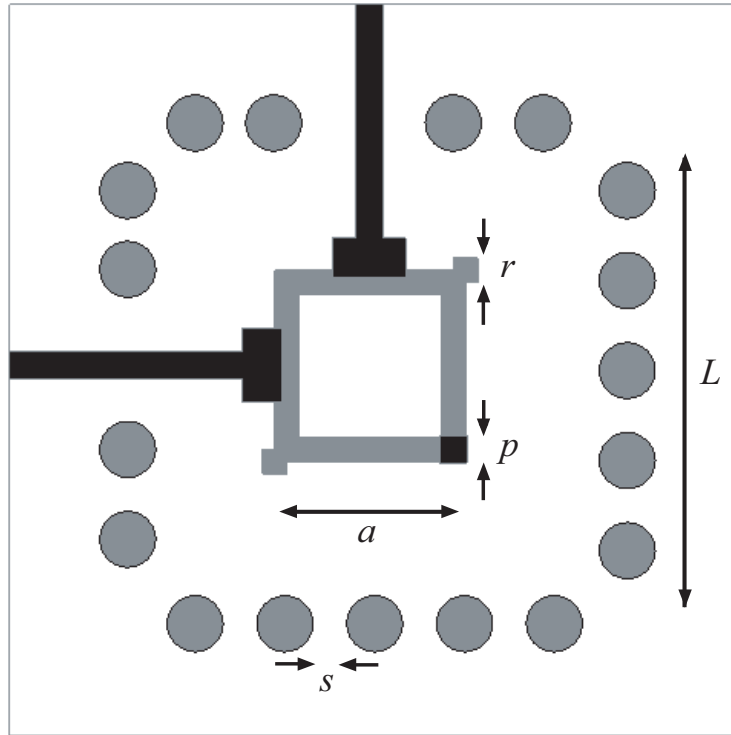


Figure 67. Top view of proposed resonator including cavity with periodic via walls.

these initial dimensions require little to no adjustment to obtain the final response. Fig. 67, shows the top view of the resonator with the cavity walls replaced by metal vias. The corner patches r are introduced to adjust the resonant frequencies produced by the square loop.

In planar dual-mode resonators with square loop topologies, the TM_{mn0}^z modes are split

when a perturbation patch or cut is introduced at any of the corners located along the symmetrical plane [55]. The electric field distributions seen in the 2D case, undergoes a natural rotating behavior. For example, in the absence of perturbation elements (corner patches, or cuts), the orthogonal modes are related to the cavity modes TM_{100}^z with source excitation at port 1, and TM_{010}^z with source excitation at port 2 [32]. These modes with identical resonant frequency are orthogonal and produce electric field patterns with two maxima located along the top and bottom loop arms (TM_{100}^z) or along the side arms (TM_{010}^z). When a perturbation is introduced the electric field maxima migrate to the corners with highest capacitance. In the case of square loop resonators, this corresponds to the perturbation patch along the plane of symmetry and the opposite corner.

In the present design, a three dimensional characteristic is added with the introduction of the resonant cavity. Also, the perturbation placed along the symmetrical plane occurs in a three dimensional fashion by the existing via connection between the perturbation patch (level $z = 100$ mil) and the resonant loop (level $z = 50$ mil). The resonator is now expanded by the resonant loop modes TM_{100}^z , TM_{010}^z and the cavity mode TM_{110}^z . A third order degeneracy is forced when both the square loop and resonant cavity are designed with equal resonant frequencies. This condition is met at the design stage given that the loop arm length $a = \lambda_g/4$ at f_0 , and the x,y,z cavity dimensions are found with $f_{res} = f_0$ in equation (2). The introduction of the patch elements p, r and the perturbation via, causes a resonant frequency split between degenerate modes TM_{100}^z , TM_{010}^z , and TM_{110}^z .

The electric field distribution inside the metal cavity undergoes a set of rotations similar to the 2D case. One noticeable difference, however, is that the 3D resonator presented here produces field maxima and minima that are not always located along the xy plane. Fig. 68 shows the different (minima/maxima) electric field planes with normal vectors N_1, N_2 and N_3 produced for each resonant frequency f_{01}, f_{02} and f_{03} . The normal vectors are described using a spherical coordinate system located in the center of the cavity at $z = H/2$. Fig. 69 shows the electric field intensity patterns. For this analysis, a full wave simulation is

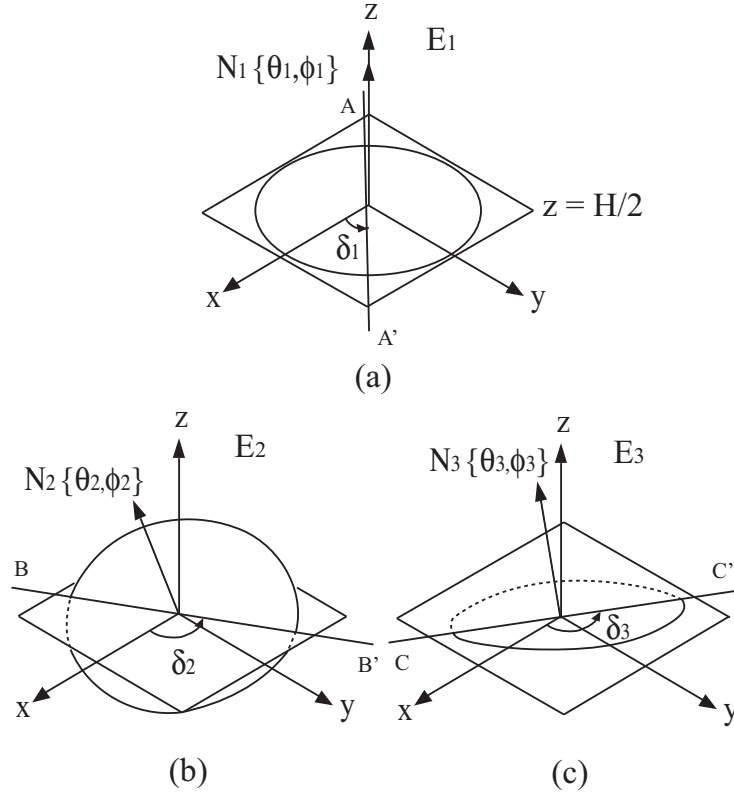


Figure 68. Rotations of planes with minima and maxima electric field, (a) E_1 at $f_{01} = f_0$, symmetrical plane with normal $N_1 = z$ ($\theta_1 = 0$ and $\phi_1 = 0$), (b) E_2 at $f_{02} > f_0$ plane with normal N_2 ($\theta_2 = 345^\circ$, $\phi_2 = 19.65^\circ$), (c) E_3 at $f_{03} < f_0$ with normal vector N_3 ($\theta_3 = 375^\circ$, $\phi_3 = 19.65^\circ$)

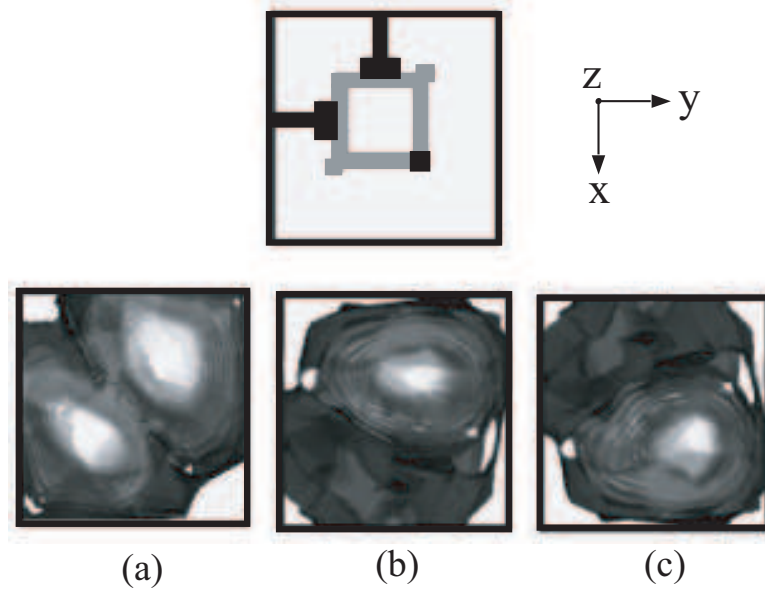


Figure 69. Electric field intensity patterns for (a) E_1 even-mode with field minima along plane AA' ($\delta_1 = 45^\circ$) (b) E_2 with field minimum along plane BB' ($\delta_2 = 75^\circ$) (c) E_3 with field minimum along plane CC' ($\delta_3 = 105^\circ$)

conducted using the software HFSS and the electric field intensity is analyzed on each of the three resonant frequencies. Fig. 69(a) shows the first electric field distribution E_1 with resonant frequency $f_{01} = f_0$. E_1 has an even characteristic with field minimum located along the symmetrical line AA' ($\delta_1 = 45^\circ$). Fig. 69(a) shows the field intensity with two field maxima located on each side of the symmetrical axis and along the plane with normal vector $N_1 = z$ ($\theta_1 = 0$ and $\phi_1 = 0$). Fig 69 (b) shows the field plane for E_2 at $f_{02} > f_0$ with normal vector N_2 ($\theta_2 = 345^\circ, \phi_2 = 19.65^\circ$). The field minimum is located along the line BB' ($\delta_2 = 75^\circ$). The field intensity is shown in Fig. 69(b). Fig 69(c) shows the field plane for E_3 at $f_{03} < f_0$. The normal vector is N_3 ($\theta_3 = 375^\circ, \phi_3 = 19.65^\circ$). The field minimum is located along the line CC' ($\delta_3 = 105^\circ$), Fig. 69(c) shows the electric field intensity. The rotation angles $\phi_2 = \phi_3$ are determined for the odd distribution fields E_2, E_3 and can be calculated based on the cavity dimensions

$$\phi_2 = \phi_3 = \tan^{-1}(H/L). \quad (36)$$

where $H = 150$ mil is the total height of the resonant cavity, and $L = 450$ mil is the side dimension of the cavity walls. It is worth noting that all 3 field distributions produce 2 field maxima located on either side of their respective axis (not visible for E_2 and E_3 given the offset angles ϕ_2 and ϕ_3). The electric field distribution closely follows the current density of the ring resonator with the current minima aligned with the axis AA', BB' and CC'.

An equivalent circuit for triple mode filters has been presented in [96] and [97] and is shown in Fig.70. The circuit parameters are calculated in terms of the lowpass equivalent elements g_i , C_i and L_i for $i = 1,2,3$. In this circuit model, the angular resonant frequency for each resonator is given by the standard equation(4), while the ABCD matrix of each inverter J can be expressed by (5)

$$\omega_{oi} = \frac{1}{\sqrt{L_i C_i}} \quad (37)$$

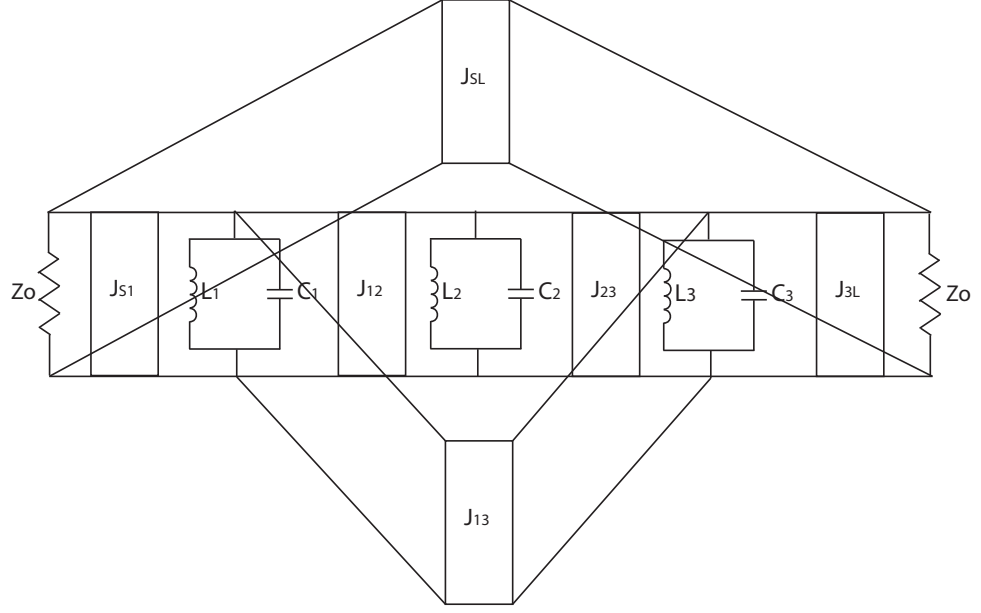


Figure 70. Equivalent circuit model for a triple mode filter with fully canonical response.

$$\begin{bmatrix} 0 & jJ^{-1} \\ jJ & 0 \end{bmatrix} \quad (38)$$

The synthesis of this filter closely follows the procedure outlined in [98] and [99]. The coupling coefficients from the different resonant modes are calculated by placing a ground termination on the last resonator and calculating or measuring the input phase reflection. A simple calibration of the reference planes at the ports is conducted to terminate the last resonator and calculate the phase response [99]. The inter-resonator coupling coefficients can be extracted from the zeros f_{zt} ($\pm 180^\circ$) and poles f_{pq} (0° crossings) of the input phase reflection. The circuit model inverters can then be calculated and related to the circuit model using equations (6) through (8).

$$J_{i,i+1} = \sqrt{b_i b_{i+1}} k_{i,i+1} \quad (39)$$

$$k_{i,i+1} = \left(\frac{\sum_{j=1}^{n-i+1} f_{zt}^2 - \sum_{q=1}^{n-i} f_{pq}^2 - f_{0i}^2}{f_{0i} f_{0,i+1}} \right)^{\frac{1}{2}} \quad (40)$$

$$f_{0i} = \frac{\prod_{t=1}^{n-i+1} f_{zt}}{\prod_{q=1}^{n-i} f_{pq}} \quad (41)$$

As demonstrated in [99], a fully canonical form is achieved when both the input/output coupling k_{SL} and the cross-coupling k_{13} are introduced in the circuit. The isolation level in the out-of-band region of the filter can be used to determine the appropriate level of coupling strength between the source and load ports [100]. At this point, it is worth noting that some topology dimensions have a natural physical constrain. For example, it is clear that the total height H of the cavity separating the ground planes is determined by the total thickness of the filter layers. Also, the size of the perturbation via between the loop and square patch p is also determined by the substrate thickness at the middle layers. Given these constrains, a computer optimization is conducted using only a minimum number of variable parameters. In this case, the variables in consideration are the coupling patch size p , and the tuning patches with size r .

The size constrain of the perturbation via forces the coupling coefficient k_{13} to exist with in a small variation of negative values. This unknown coupling value is calculated by matching the variation in the input phase reflection when the inverter J_{13} is introduced. The negative value inverter J_{13} causes the final filter response to have the third transmission zero in the upper side of the passband. This result is in good agreement with the known cross-coupling response of the filter which produces a transmission zero at the upper side under the condition $J_{12}J_{23}/J_{13} > 0$ and a lower side transmission zero under the condition $J_{12}J_{23}/J_{13} < 0$ [96]. A slight adjustment in the resonant frequencies of the filter is produced when the tuning patches r are varied. The fractional bandwidth of the filter Δ is mostly affected by the inter-resonator coupling $k_{12} = -k_{23}$ which in turn are directly proportional to the coupling size p .

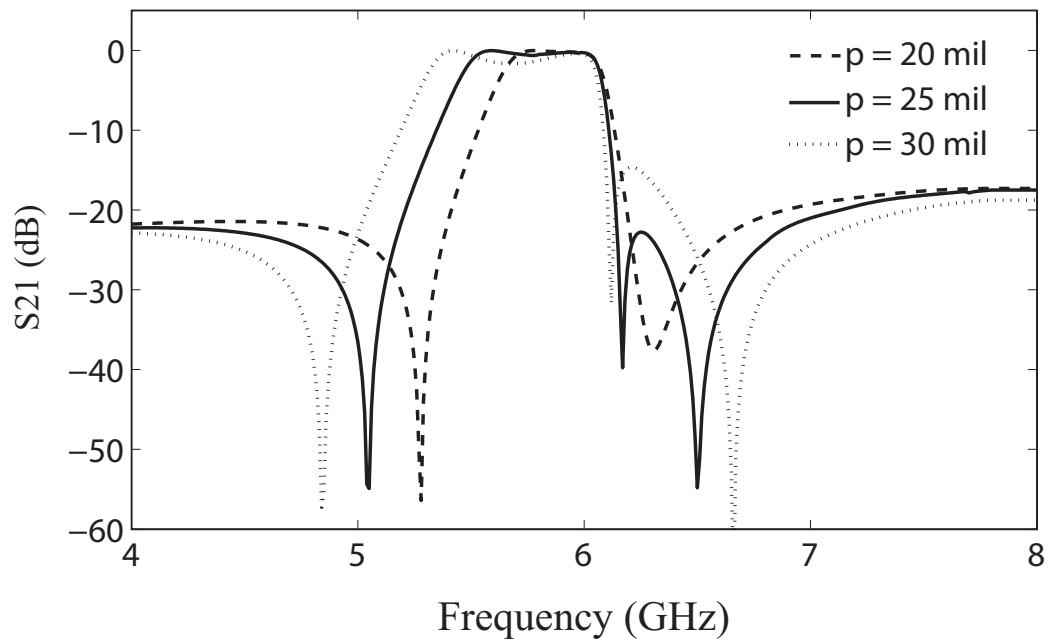


Figure 71. Simulated response for $p = 20, 25, 30$ mil and optimal $r = 22$ mil.

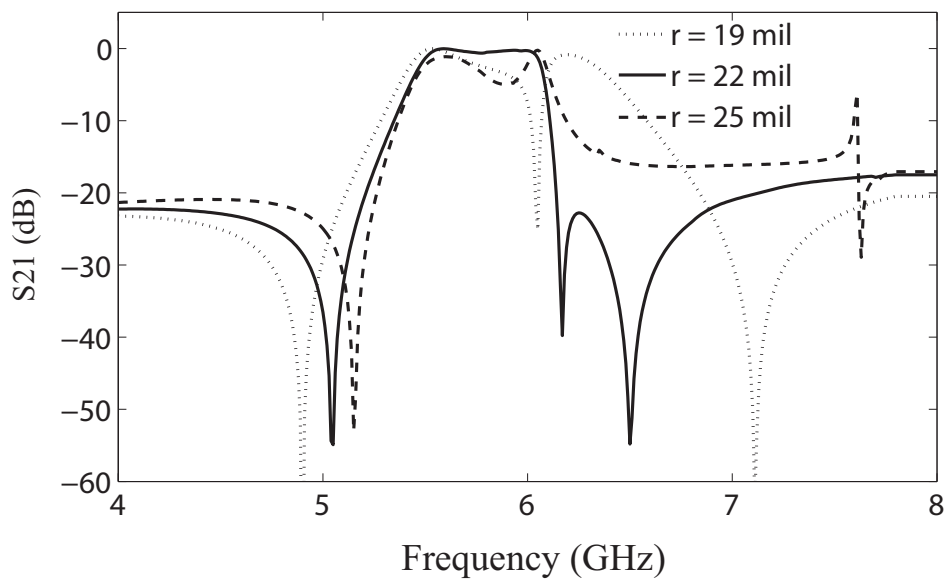


Figure 72. Simulated response for $r = 19, 22, 25$ mil and optimal $p = 25$ mil.

7.2 Triple-Mode Design Methodology

This section presents a design outline for a triple mode fully canonical form filter with $f_0 = 5.8$ GHz. The goal is to produce a third order response with 3 transmission zeros. The following procedure can be followed to scale the filter to an arbitrary frequency band. The current design requires an initial calculation of the resonant cavity dimensions x, y . For simplicity, the cavity is design under the constrains $z = \lambda_g/4$ and $x = y$. This constrain guarantees that the dimensions of the resonant loop remains within the x and y boundaries of the cavity. Setting $f_{res} = f_0 = 5.8$ GHz in equations (1) and (2), it follows that the resonance from mode TM_{110}^z occurs when $x = y = 460$ mil. The different layers of the filters are simply located at heights $H/3 = 50$ mil, $H/2 = 75$ mil and $2H/3 = 100$ mil, where H is the total height of the filter or cavity dimension z . At this point, the sides of the filter are replaced by metal vias of with diameter $d_c = 50$ mil. The center of the via is placed along the cavity wall. This allows some of the standard planar attributes such as integration, system in package and compactness of design.

The square loop resonator is designed with arm sizes $a = \lambda_g/4 = 150$ mil. The first resonance split for the square loop modes TM_{100}^z and TM_{100}^z is produced with introduction of the capacitive square patches r [55]. The size of these patches affect the coupling between the synchronous resonators k_{13} , and also gives a degree of freedom allowing the control of the location of the two loop resonances. This will be one of the variables used for fine tuning and optimization of the final response. Its value is dependant on the fractional bandwidth Δ , and external quality factor of the filter Q_e .

The ports are designed with the standard 90° orthogonal feed. This allows the dual-mode operation of the loop and also creates one of the transmission zero on the lower side of the passband. This effect has been studied in [96] and it is attributed to the introduction of the coupling between source and load. J_{sl} is calculated from the isolation level of the filter as shown in [100]. The ports are designed as strip lines with characteristic impedance $Z_0 = 50 \Omega$

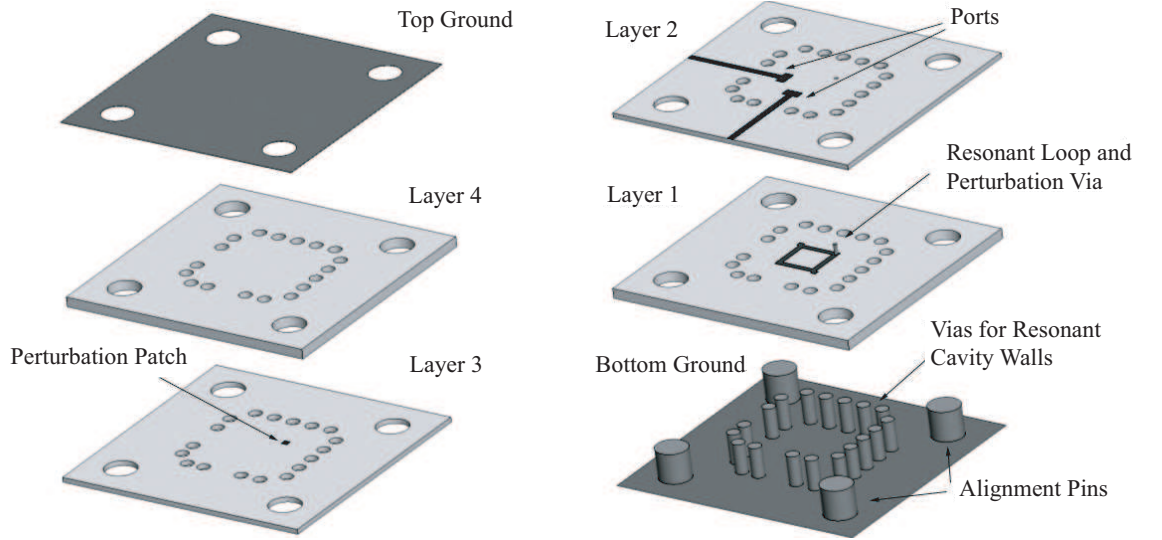


Figure 73. Construction layers for the fabricated triple mode filter.

The coupling via with diameter $d_v = 15$ mil ($\lambda_g/40$) and square patch p are introduced to control both the inter-resonance couplings $k_{12} = -k_{23}$ and the mode resonant frequency f_{02} . This corresponds to the asynchronous middle resonator from the equivalent circuit model in Fig. 70. A variation in the diameter of the perturbation via $d_v = 20, 15, 10$ and 5 mil shows very little effect on the overall response. This is to be expected given the vertical direction of the electric field (perpendicular to the ground plane) of the TM_{mnl}^z modes. The size $d_v = 15$ mil was simply chosen because it is well within the dimensions of the perturbation patch and it is large enough to guarantee an appropriate electric contact to both the patch p and resonant loop. The structure is then optimized using the perturbation patches p and r as variables.

By computer optimization it is found that the optimal triple mode response with fully canonical form is produced when $p = 25$ mil and $r = 22$ mil. Fig. 71 shows the simulated S21 response for the various values of $p = 20, 25$ and 30 mil and a fixed optimal value of $r = 22$ mil. Here, the effect of the perturbation patch can be seen as it directly affects the split of degenerate modes. The case with $p = 20$ mil corresponds to the dual-mode operation where only the loop resonances have been coupled. The case with $p = 30$ mil shows stronger coupling for k_{12} and k_{23} and therefore a larger fractional bandwidth Δ . Fig.

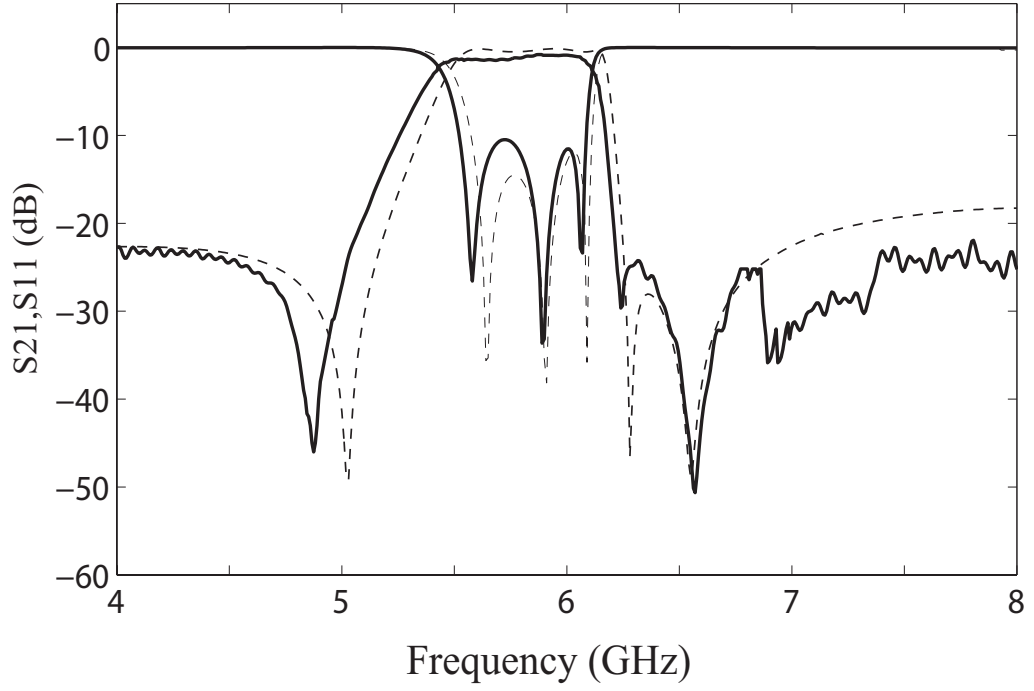


Figure 74. Measured (solid line) vs. simulated (dashed line).

72 shows the S21 response for the resonator with fixed optimal $p = 25$ mil and variable size $r = 19, 22$ and 25 mil. In the case with $r = 19$, the synchronous loop resonances are shifted to higher frequencies resulting in a passband interrupted by a transmission zero. This transmission zero is produced from the introduced cross coupling k_{13} . The case with $r = 25$ mil shows the resonant loop frequencies shifted to lower values with respect to the optimal case ($r = 22$ mil, $p = 25$ mil). The equivalent circuit in Fig. 70, models the behavior of the structure and the optimal parameters are found to be $J_{S1} = J_{3L} = 0.23$, $J_{12} = -J_{23} = 2.4$, $J_{13} = -1.28$, $J_{SL} = 0.008$, $C_1 = C_3 = 0.765nF$, $L_1 = L_3 = 0.94pH$, $C_2 = 1.3nF$, $L_2 = 0.53pH$. The optimized dimensions of the filter are $a = 150$ mil ($\lambda_g/4$), $p = 25$ mil ($\lambda_g/24$), $r = 22$ mil ($\lambda_g/27$), $S = 50$ mil ($\lambda_g/12$), $L = 450$ mil ($3\lambda_g/4$).

The substrate used in this filter was Rogers Duroid, with a dielectric constant of $\epsilon_r = 10.2$, $\tan\delta = 0.025$ and 0.5 OZ of copper metallization. Fig. 73 shows the fabricated layers. A substrate thickness of 50 mil was used for layers 1 and 4 and a thickness of 25 mil was used for the middle layers 2 and 3. The total filter height $H = 150$ mil. The via holes for the

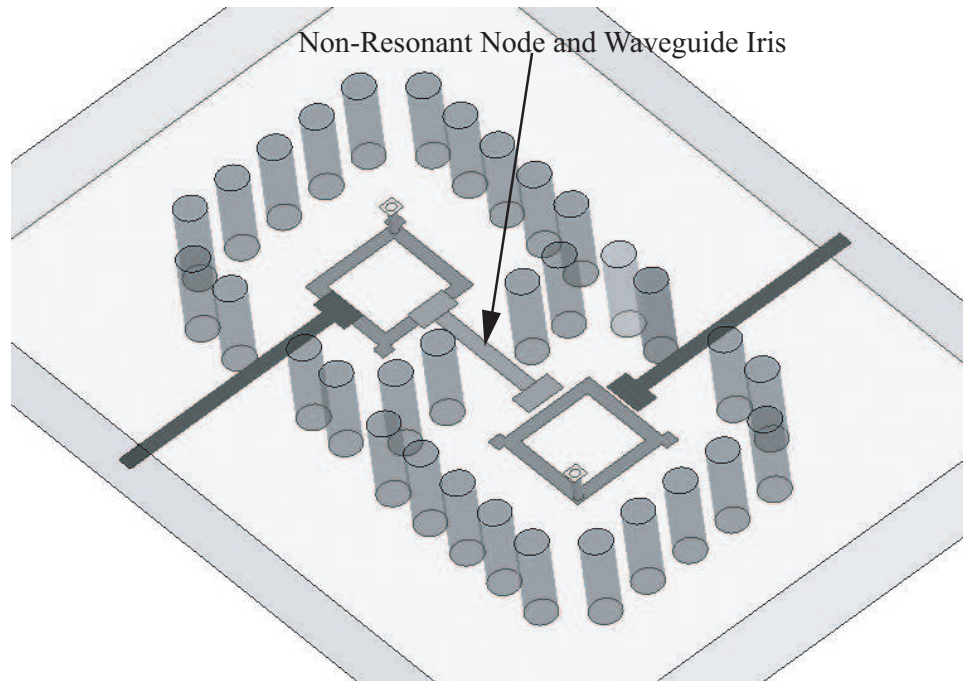


Figure 75. Conceptual realization of higher order filters

cavity have a diameter of 50 mil, while the perturbation via has a diameter of 15 mil. The boards were individually patterned using standard photolithography while the vias were completely filled using copper wires of gauges AWG 17 and 27. An aluminum fixture was fabricated with alignment pins of 1/8 inch. The fixture served as the ground planes and as the holder for the SMA connectors. The measurements were conducted after a short, open, load and thru (SOLT) standard calibration. Excellent agreement can be seen between the measured and simulated transmission and return responses in Fig.74. The insertion loss of the filter was 1.1 dB including the loss of the SMA connectors. This shows an advantage over standard dual-mode planar filters with insertion losses ranging from 2.4 dB [55] to 3.1 dB [101]. Also the largest effective dimension of the filter $L = 11.7$ mm is smaller than the waveguide triple mode reported in [102] with largest dimension of 19.6 mm at 10 GHz. The return loss was better than 11 dB across the band. This may be further improved by increasing the external coupling of the filter. This can be easily accomplished by enlarging the overlapping area between the input/output ports and the resonant loop. The measured fractional bandwidth was $\Delta = 0.12$.

Higher order filters using this multilayer approach may be realized by increasing the number of resonators. In this case, both the resonant loops and the cavities would have to be appropriately coupled. Fig. 75 shows a conceptual six order filter using a non-resonant node to couple the resonator loops and a waveguide iris to couple the filter cavities.

7.3 Chapter Summary

This chapter reports a new type of filter with a third order degeneracy. A hybrid combination of resonant planar structures and waveguide cavities is used to design a semi-planar topology. This filter uses a multilayer approach and produces low loss when compared to conventional planar filters. The filter is able to keep a small size profile while providing resonant Qs and loss performance that are usually only seen in waveguide filters. The resulting topology has all the desired characteristics of a planar circuit in terms of substrate integration. The in-cavity design eliminates cross-talk with other components making it very attractive for system integration.

The X-band prototype yielded an insertion loss of 1.1 dB including the loss of the SMA connectors. The return loss was better than 11 dB across the band. The measured fractional bandwidth was 12 %.

CHAPTER 8

CONCLUSION AND FUTURE WORK

This work has produced several first time demonstrations of reconfigurable filter techniques, unique dual-mode and triple-mode filters with advanced responses, and several hybrid designs using multi-layer technologies, ferroelectric and MEMS switches.

Agile frequency and bandwidth filters were demonstrated using inter-resonator coupling variation techniques. Single mode filters with adjustable bandwidth require a length compensating technique to maintain a fixed center frequency. Filters with tunable center frequency, on the other hand, suffer from return loss degradation if the external coupling is kept fixed. Trade offs between tunability dynamic range, loss, and circuit complexity was established through out the research work.

Tunable filters with fractional bandwidths were found to produce an $N:1$ pass band ratio where N is the order of the filter. Tuning mechanism was achieved in a discrete manner by introducing p-i-n diodes or MEMS switches that directly manipulate the geometry of the filter's topology in a controlled manner. This work includes the first filter demonstration that combines ferroelectric BST capacitors and MEMS switches. Continuous tuning was achieved by strategically placing capacitors at the loading ends of resonators. These tunable capacitors were able to effectively change the effective length of the resonators and consequently tune their resonant frequency.

Dual-mode resonators were designed with reconfigurable passband width, and center frequency. Moreover, coupling matrix synthesis techniques were used as powerful tools for the creation of filters capable of manipulating the location of their transmission zeros in both the imaginary and/or real axis of the complex s -plane. Dual-mode filters that are tunable in frequency provide advantages in the reduction of size and number of tuning elements when compare to single-mode tunable filters today.

A triple-mode bandpass filter was designed using a multilayer approach for the first

time. The filter topology consists of a square loop resonant pattern located inside a reflector cavity. A filter prototype was fabricated and measured producing a fully canonical filtering function with 3 resonant poles and 3 transmission zeros. The final prototype approaches the performance of waveguide filters in terms of loss, while keeping a compact size profile comparable to standard planar filters.

8.1 Future Work

Future research opportunities may be created from this investigation. The derived synthesis and design techniques to create reconfigurable bandpass filters can also be applied to a range microwave devices. Microwave circuits that can benefit from added functionality include adaptable antenna arrays, impedance tuners, broad-band matching networks, couplers and phase-shifters.

The work presented here may be expanded by investigating the behavior of tunable filters as packaged stand-alone units or as fully integrated circuits in a system-on-package approach. The performance of tunable filters and tunable components can be explored at higher frequencies such as V-band and W-band. Other possible projects include the integration of active elements and reconfigurable circuits.

Components such as the hybrid triple-mode filter give rise to potential future investigations. The filters using this semi-planar technology show advantages over standard microstrip circuits by providing higher Qs and lower loss. It is important to determine the limitation of this technology in term of power handling. Power handling and slightly lower loss are the remaining advantages of waveguide filters. Future work may also include the use of MEMS switches in the creation of tunable semi-planar or waveguide filters.

REFERENCES

- [1] R. W. DeGrasse, Low-loss gyromagnetic coupling through single-crystal garnets, in Magnetism Conference Philadelphia, 1958.
- [2] P. S. C. Jr., Magnetically tunable micro-wave filters employing single-crystal garnet resonators, in West Coast Joint Technical Meeting of the Committee on Solidstate Devices of the AIEE, the PGED, and the San Francisco Section of PGMTT, Jan. 1960.
- [3] R. Blau, Yig filters in the 50500 mc range, Proc. IEEE, vol. 52, 1964.
- [4] P. S. Carter, Side-wall, coupled, strip-transmission-line magnetically tunable filters employing ferrimagnetic yig resonators, IEEE Trans. on Microwave Theory and Techniques, vol. 13, 1965.
- [5] M. H. N. Potok, Capacitive-iris-type mechanically tunable waveguide filters for the x-band, Proc. IEE (London), vol. 109, 1962.
- [6] G. W. R. Wadd and E. Cota, Compact tunable filters, Microwave J , vol. 7, 1964.
- [7] H. L. Schumacher, Direct coupled ganged tuned bandpass filters, Microwave J, vol. 7, 1964.
- [8] G. D. Boyd, Experiments on the interaction of a modulated electron beam with a plasma, Nonr 220 Technical Report No. 1 , Calif. Inst. of Tech., vol. 13, 1959.
- [9] I. Kaufman and W. H. Steier, An electronically tunable band pass microwave filter, Space Technology Laboratories, Inc. Technical Report, 1962.
- [10] A. E. Williams, Four-cavity elliptic waveguide filter, IEEE Trans. Microwave Theory and Techniques, vol. 18, 1970.
- [11] J. A. R. Kaur, A tunable bandpass ring filter for rectangular dielectric waveguide integrated circuits, IEEE Trans. Microwave Theory and Techniques, 1976.
- [12] A. Presser, High-speed, varactor-tunable microwave filter element, IEEE Trans. Microwave Theory and Techniques, vol. 21, 1979.
- [13] A. E. Atia and A. E. Williams, New type of bandpass filters for satellite transponders, COMSAT Technical Review, Vol. 1, NO. 1, pp. 21-43, Fall 1971.
- [14] A. E. Atia and A. E. Williams, Narrow bandpass waveguide filters, IEEE Trans. on Microwave Theory and Tech., Vol. MTT-20, pp. 258-265, Apr. 1972.

- [15] C. B. Hofman and A. R. Baron, Wideband ESM receiving systems Part I, *Adicroitave J.*, vol. 23, no. 9., Sept. 1980.
- [16] W. J. Keane, YIG filters aid wide open receivers, *Microwave J.*, vol. 17, no. 8, Sept. 1980.
- [17] I. C. Hunter and John David Rhodes, Electronically Tunable Microwave Bandpass Filters, *IEEE Trans. Microwave Theory Tech.*, vol. MTT-30, Sept. NO. 9, September 1982
- [18] I. C. Hunter and J. D. Rhodes, Varactor tuned microwave bandstop filters: *IEEE*
- [19] Variable Impedance Devices. M. J. Howes and D. V. Morgan, Eds. New York: Wiley, *Trans. Microwave Theory Tech.*, vol. MTT-30, Sept. ch. 1.
- [20] Kun Wang and Clark T.-C. Nguyen High-Order Micromechanical Electronic Filters *IEEE Trans. Microwave Theory Tech.*, vol. MTT-30, Sept. 19
- [21] H. T. Kim, J. H. Park, Y. K. Kim, and Y. Kwon, Millimeter-wave micromachined tunable filters, in *IEEEMTT-SDig.*, vol. 3, June 1999, pp. 12351238.
- [22] Jeremy B. Muldavin, Gabriel M. Rebeiz X-Band nnable MEMS Resonators 2000 *IEEE MTT-S Digest*
- [23] D. Peroulis, S. Pacheco, K. Sarabandi, and L. P. B. Katehi, Tunable lumped components with applications to reconfigurable MEMS filters, in *IEEE MTT-S Dig.*, May 2001, pp. 341344.
- [24] Hong-Ted Kim, Jae-Hyoung Park, Yong-Kweon Kim, and Youngwoo Kwon, Low-Loss and Compact V-Band MEMS-Based Analog Tunable Bandpass Filters *IEEE Microwave and Wireless Comp. lett.* VOL. 12, NO. 1 1, November 2002
- [25] R. D. Wanselow, prototype characteristics for a Class of Dual-Mode Filters, *IEEE Trans. Microwave Theory Techn.* MTT-23 (1 975) 708-7 1 1.
- [26] G. Pfitzenmaie, An Exact Solution for a six-cavity dual-mode elliptic bandpass filter *IEEE Trans. Microwave Theory Techn.* MTT-22 (1 977)
- [27] R. J. Cameron AND J. D. Rhodes, Asymmetric Realizations for Dual-Mode Bandpass Filters *IEEE Trans. Microwave Theory Techn.* MTT-29, January 198 1
- [28] S. J. Fiedziuszko, Dual Mode Dielectric Resonator Loaded Cavity Filter *IEEE Pans. Microwave Theory Tech.*, VOL.MTT-30, pp 131 1- 1316, September 1982.
- [29] I. Galin, A New Type Of Dual Mode Circular Cavity Filter, *Microwave Journal*, Vol. 23, pp 92-93, October 1980.
- [30] Xiao-Peng Liang, Kawthar A. Zaki Dual Mode Coupling by Square Cut in Res- onators and Filters 1992 *IEEE MTT-SDigest*, pp 1327 - 1330.

- [31] J. A. Curtis and S. J. Fiedziuszko Miniature dual-mode microstrip filters 1991 IEEE MTT-S Digest, pp 443 - 446.
- [32] J.S. Hong and M.J. Lancaster Bandpass characteristics of new dual-mode microstrip square loop resonators Electronic letters 25th May 1995 Vol. 31 No. 11 pp 891-892
- [33] J.S. Hong and M.J. Lancaster Realisation of quasielliptic function filter using dual-mode microstrip square loop resonators Electronic letters 25th May 1995 Vol. 31 NO. 11 pp 2085-2086
- [34] A. Abramowicz: Investigation of the HTS microstrip filters based on dual-mode ring resonators, Proc. Int. Conf. on Microwaves and Radar, MIKON-98, Krak6w 1998, pp.8-12
- [35] S.J. Hedges, D. Jedamzik, M. Guglielmi: Dual mode HTS microstrip ring resonator filter, Proc. ESA/ESTEC Workshop on: Space Applications of High Temperature Superconductors, Noordwijk, The Netherlands 1993, pp.97-106
- [36] J.-S. Hong and S. Li Dual-mode microstrip triangular patch resonators and filters, 2003 IEEE MTT-S, Int. Microwave Symp. Dig., June 2003, pp. 1901-1904.
- [37] M. Saito, Synthesis for general-coupled resonator transmission networks, Electron. Commun. Japan, vol. 53-A, no. 5, pp. 2633, Chelsea Publishing Co., 1969.
- [38] J. D: Rhodes, The theory of generalized interdigital networks, IEEE Trans. Circuit Theory, vol. CT-16, pp. 280-288, Aug. 1969.
- [39] A. E. Atia and A. E. Williams, New types of waveguide bandpass filters for satellite transponders. COMSAT Tech. Rev.. vol. 1, no. 1, pp. 21-43, 1971.
- [40] A. E. Atia and A. E. Williams, Narrow-bandpass waveguide filters, IEEE Trans. Microwave Theory Tech., vol. MTT-20, pp. 258-265, Apr. 1972.
- [41] R. E. Collin, Foundations for Microwave Engineering. New York: Mc- Graw-Hill, 1966.
- [42] Narrow-bandpass waveguide filters, IEEE Trans. Microwave Theory Tech., vol. MTT-20, pp. 258-265, Apr. 1972.
- [43] A. E. Atia, A. E. Williams, and R. W. Newcomb, Narrow-band multiple- coupled cavity synthesis, IEEE Trans. Circuits Syst., vol. CAS-21, pp. 649-655, Sept. 1974.
- [44] M. H. Chen, Singly terminated pseudo-elliptic function filter, COMSAT Tech. Rev., vol. 7, pp. 527-541, Fall 1977.
- [45] S. Amari, Direct synthesis of folded symmetric resonator filters with source load coupling, IEEE Microwave Wireless Comp. Lett., vol. 11, pp. 264-266, June 2001,
- [46] H. C. Bell, Canonical asymmetric coupled-resonator filters, IEEE Trans. Microwave Theory Tech., vol. MTT-30, pp. 1335-1340, Sept. 1982.

- [47] R. J. Canieron, General coupling matrix syntliesis methods for Chebyshev filtering functions, IEEE Trans. Microwave Theoiy Tech., vol. 47, pp. 433442, Apr. 1999.
- [48] Richard J. Cameron, Advanced Coupling Matrix Synthesis Techniques for Microwave Filters IEEE Trans. Microwave Theory Tech., vol. 51, pp. 1-10, Jan. 2003.
- [49] S. Amari, General coupling matrix synthesis methods for Chebyshev filtering functions, IEEE Trans. Microwave Theory Tech., vol. 47, pp. 433442, Apr. 1999.
- [50] Smain Amari, Uwe Rosenberg, and Jens Bornemann, Adaptive Synthesis and Design of Resonator Filters With Source/Load-Multiresonator Coupling IEEE Trans. Microwave Theory Tech. vol. 50, pp. 1969 1978, Aug. 2002.
- [51] J.-S. Hong and M. J. Lancaster, Microstrip Filters for RF/Microwave Applications. New York: Wiley, 200 1.
- [52] J.-S. Hong Coupling of asynchronously tuned coupled microwave resonators, IEE Proc. Microw. Antennas Propag., 2000, 147, pp. 354-358.
- [53] G.L. Mathaei, L. Young, and E.M.T Jones. Microwave Filters, Impedance-Matching Networks, and Coupling Structures. Nonvell, MA: Artech House, 1980, pp. 427-433.
- [54] Dussopt, L. and Rebeiz G. Intermodulation Distortion and Power handling in RF MEMS Switches, Varactors and Tunable Filters, IEEE Trans. Microwave Theory Tech., vol.51, pp. 573-577, Apr. 2003.
- [55] A. Goriir, Description of coupling between degenerate modes of a dual-mode microstrip loop resonator using a novel perturbation arrangement and its dual-mode bandpass filter applications, IEEE Trans. Microwave Theory Tech., vol. 52, pp. 671 - 677, Feb. 2004.
- [56] S. Amari, Comments on description of coupling between degenerate modes of a dual-mode microstrip loop resonator using a novel perturbation arrangement and its dual-mode bandpass filter applications, IEEE Trans. Microwave Theory Tech., vol. 52, pp. 2190-2192, Sep. 2004.
- [57] C. Rauscher Reconfigurable bandpass filter with a three-to-one switchable passband width, IEEE Trans. Microwave Theory Tech., vol. 51, pp. 573 - 577, Feb. 2003.
- [58] C. Lugo, D. Thompson and J. Papapolymerou, Reconfigurable Bandpass Filter with Variable Bandwidth and 5.8 GHz Using a Capacitive Gap Variation Technique, Eur: Micruwave Conf Dig., Munich, Germany, Oct. 2003, pp. 923-926.
- [59] A. Gorur Realization of a dual-mode bandpass filter exhibiting either a chevyshev or an elliptic characteristic b changing perturbations size, IEEE Microwave Wireless Corp. Lett., vol. 14, pp. 118-120, March 2004.
- [60] I. Wolff, Microstrip bandpass filter using degenerate modes of a microstrip ring resonator, Electrurz. Lett., vol. 8, no. 12, pp. 302-303, June 1972.

- [61] C. Rauschler Reconfigurable bandpass filter with a three-to-one switchable passband width, *IEEE Pans. Microwave Theory Tech.*, vol. 51, pp. 573 - 577, Feb. 2003.
- [62] J.-S. Hong and S. Li Theory and experiment of dual-mode microstrip triangular patch resonators and filters, *IEEE Trans. Microwave Theory Tech.*, vol. 52, pp. 1237-1243, April. 2004.
- [63] A. C. Kundu and I. Awai Control of attenuation pole frequency of a dual-mode microstrip ring resonator bandpass filter, *IEEE Trans. Microwave Theory Tech.*, vol. 49, pp. 1113-1117, June. 2001.
- [64] J. -S. Hong and M. J. Lancaster, Bandpass characteristics of new dual-mode microstrip square loop resonators, *Electron. Lett.*, vol. 31, no. 11, pp. 891-892, May 1995.
- [65] S. Amari Coments on description of coupling between degenerate modes of a dual-mode microstrip loop resonator using a novel perturbation arrangement and its dual-mode bandpass filter applications, *IEEE Trans. Microwave Theory Tech.*, vol. 52, pp. 2190-2192, Sep. 2004.
- [66] G. Zheng, J. Papapolymerou and M. Tentzeris, Design of a Compact, Broadband Via-Less CPW to Microstrip Transition for RF Communication Systems on a Chip, *IEEE Microwave and Wireless Components Letters*, Vol. 13, No. 12, pp. 544-546, December 2003.
- [67] Flag freq patch J. -S. Hong and M. J. Lancaster, "Bandpass characteristics of new dual-mode microstrip square loop resonators," *Electron. Lett.*, vol. 31, no. 11, pp. 891-892, May 1995.
- [68] R. Wu and S. Amari "New triangular microstrip loop resonators for bandpass dual-mode filter applications," *2005 IEEE MTT-S, Int. Microwave Symp. Dig.*, June 2005, pp. 118-120.
- [69] C. Lugo and J. Papapolymerou, "Bandpass filter design using a microstrip triangular loop resonator with dual-mode operation," *IEEE Microwave Wireless Comp. Lett.*, vol. 15, pp. 475 - 477, July 2005.
- [70] C. Lugo, J. Hadrick and J. Papapolymerou, " Dualmode reconfigurable filter for 3D system on package (SOP) integration *Electron Comp. and Tech. Proceedings* pp. 532 - 535, June 2005
- [71] Smain Amari, Uwe Rosenberg, and Jens Bornemann, "Adaptive Synthesis and Design of Resonator Filters With Source/Load-Multiresonator Coupling" *IEEE Trans. Microwave Theory Tech.* vol. 50, pp. 1969-1978, Aug. 2002.
- [72] E. Fourn, A. Pothier, C. Champeaux, P. Tristant, A. Catherinot, P. Blondy, G. Tanne, E. Rius, C. Person and F. Huret, "MEMS switchable interdigital coplanar filter", *IEEE Trans. Microwave Theory Tech.*, vol. 51, pp. 320- 324, Jan. 2003.

- [73] E. Fourn, C. Quendo, E. Rius, A. Pothier, P. Blondy, C. Champeaux, J.C. Orlianges, A. Catherinot, G. Tanne, C. Person, F. Huret "Bandwidth and central frequency control on tunable bandpass filter by using MEMS cantilevers," *2003 IEEE MTT-S, Int. Microwave Symp. Dig.*, June 2003, pp. 523-526.
- [74] R. Young, J. Adam, C. Vale, T. Braggins, S. Krishnaswamy, C. Milton, D Bever, L. Chorosinski, L. Chen, D. Crockett, C. Freidhoff, S. Talisa, E. Cappelle, R. Tranchini, J. Fende, J. Lorthioir and A. Torres. "Low-loss bandpass RF filter using MEMS capacitance switches to achieve a oneoctave tuning range and independently variable bandwidth" *2003 IEEE MTT-S, Int. Microwave Symp. Dig.*, June 2003, pp. 1781-1784.
- [75] A. Brown, G. Rebeiz, "A varactor tune RF filter", *IEEE Trans. Microwave Theory Tech.*, vol. 48, pp. 1157 - 1160, July 2000.
- [76] B. Lakshminarayanan and T.Weller "Tunable bandpass filter using distributed MEMS transmission lines," *2003 IEEE MTT-S, Int. Microwave Symp. Dig.*, June 2003, pp. 1789-1792.
- [77] A. Tamijani, L. Dussopt, and G. Rebeiz "A high performance MEMS miniature tunable bandpass filter," *2003 IEEE MTT-S, Int. Microwave Symp. Dig.*, June 2003, pp. 1785-1788.
- [78] D. Kuylenskierna, A. Vorobiev, and S. Gevorgian, "40 GHz lumped element tunable bandpass filters with transmission zeros based on thin Ba_{0.25}Sr_{0.75}TiO₃ (BST) film varactors." *2006 Topical Meeting on Silicon Monolithic Integrated Circuits in RF Systems*, Page(s):342 - 345.
- [79] C. Lugo and J. Papapolymerou, "Single switch reconfigurable bandpass filter with variable bandwidth using a dual-mode triangular patch resonator" *2005 IEEE MTT-S, Int. Microwave Symp. Dig.*, June 2005, pp. 779 - 782.
- [80] Y.-K. Yoon, D. Kim, M. G. Allen, J. S. Kenney, and A. T. Hunt, "A reduced intermodulation distortion tunable ferroelectric capacitor architecture and demonstration," *IEEE Trans. Microwave Theory Tech.*, vol. 51, no. 12, Dec. 2003, pp. 2568-2576.
- [81] F. A. Miranda, G. Subramanyam, F. W. Van Keuls, R. Romanofsky, J. D. Warner, and C. H. Mueller, "Design and development of ferroelectric tunable microwave components for Ku- and K-band satellite communication systems," *IEEE Trans. Microwave Theory Tech.*, vol. 48, no. 7, Jul 2000, pp. 1181-1189.
- [82] A. Tombak, J. P. Maria, F. T. Ayguavives, Z. Jin, G. T. Stauff, A. I. Kingon, and A. Mortazawi, "Voltage-controlled RF filters employing thin-film barium-strontium-titanate tunable capacitors," *IEEE Trans. Microwave Theory Tech.*, vol 51, no. 2, Feb 2003, pp. 462-467.
- [83] R. A. York, A. S. Nagra, P. Periaswamy, O. Auciello, S. K. Streiffer, and J. Im, "Synthesis and characterization of (Ba_xSr_{1-x})Ti_{1+y}O_{3+z} thin films and integration into

- microwave varactors and phase shifters”, *Integr. Ferroelectrics*, vol. 34, no. 1-4, 2001, pp. 1617-1628.
- [84] F. De Flaviis, N. G. Alexopoulos, O. M. Stafsudd, ”Planar microwave integrated phase-shifter design with high purity ferroelectric material,” *IEEE Trans. Microwave Theory Tech.*, vol. 45, no. 6, Jun 1997, pp. 963 - 969.
 - [85] A. T. Hunt, W.B. Carter, and J.K. Cochran, Jr., ”Combustion Chemical Vapor Deposition: A Novel Thin-Film Deposition Technique.” *App. Phys. Lett.*, Vol. 63, No. 2, pp. 266-268, July 1993.
 - [86] A. T. Hunt, W. B. Carter and J. K. Cochran, Jr., ”Combustion chemical vapor deposition of films and coatings,” US Patent # 5,652,021, July 29, 1997.
 - [87] J. Schmitt, G. G. Cui, H. A Luten, III, F. Yang, F. A. Gladden, S. Flanagan, Y. Jiang, and A. T. Hunt, ”Electronic and optical materials,” US Patent # 6,986,955, January 17, 2006.
 - [88] J. W. Lu and S. Stemmer, ”Low-loss, tunable bismuth zinc niobate films deposited by rf magnetron sputtering,” *Appl. Phys. Lett.* vol. 83, no. 12, pp. 2411-2413, Sept. 2003.
 - [89] B. Acikel, T. R. Taylor, P. J. Hansen, J. S. Speck, and R. A. York, ”A new high performance phase shifter using Ba_{0.5}Sr_{0.5}TiO₃ thin films,” *IEEE Microwave wireless Components Lett.*, vol. 12, no. 7, pp. 237-239, Jul. 2002.
 - [90] A. E. Williams and A. E. Atia, ”Dual-mode canonical waveguide filters,” *IEEE Trans. Microwave Theory Tech.*, vol. MTT25, pp. 1021-1026, Dec. 1977.
 - [91] S. J. Fiedzinski, ”Dual-mode dielectric loaded cavity filters,” *IEEE Trans. Microwave Theory Tech.*, vol. MTT30, pp. 1311-1316, Sept. 1982.
 - [92] L.H. Chua and D. Mirshekar-Syahkal, ”Analysis of dielectric loaded cubical cavity for triplemode filter design” *IEE Proc. Microw. Antennas Propag.*, vol. 151, no. 1, pp. 61-66, Feb. 2004,.
 - [93] J. Hattori, H. Wakamatsu, H. Kubo and Y. Ishikawa, ”2 GHz band triple mode dielectric resonator duplexer for digital cellular base station”. *Asia-Pacific Microwave Conf.*, 2000, pp. 1315-1318.
 - [94] I.C. Hunter, J.D. Rhodes and V. Dassonville, ”Triple mode dielectric resonator hybrid reflection filters ” *IEE Proc. Microw. Antennas Propag.*, vol. 145, pp. 337-343, Aug. 1998.
 - [95] X. D. Huang and C. H. Cheng ”A novel coplanar-waveguide bandpass filter using a dual-mode square-ring resonator” *IEEE Microw. Wireless Compon. Lett.*, vol. 16, no. 3, pp. 13-15, Jan. 2006.
 - [96] S. J. Park, K. V. Caekenberghe and G. M. Rebeiz ”A Miniature 2.1-GHz Low Loss Microstrip Filter With Independent Electric and Magnetic Coupling” *IEEE Microw. Wireless Compon. Lett.*, vol. 14, no. 10, pp. 13-15, Oct. 2004.

- [97] L. H. Chua and D. M. Syahkal, "Analysis and design of three transmission zeros band-pass filter utilizing triple-mode dielectric loaded cubical cavity", *2003 IEEE MTT-S, Int. Microwave Symp. Dig.*, June 2003, pp. 937-940.
- [98] L. H. Chua and D. M. Syahkal, "Rigorous Analysis of effect of input-output direct coupling on triple-mode third-order chebyshev bandpass filter" *Eur. Microwave Conf. Dig.*, Munich, Germany, Oct. 2003, pp. 179-182.
- [99] W. Steyn and P. Meyer, "A shorted waveguide-stub coupling mechanism for narrow-band multimode coupled resonator filters" *IEEE Trans. Microwave Theory Tech.*, vol. 52, pp. 1622-1625, June. 2004.
- [100] A. E. Atia and H.-W. Yao, "Tuning and measurement of couplings and resonant frequencies for cascaded resonators," *IEEE MTT-S Int. Microwave Symp. Dig.*, June 2000, pp. 1637-1640.
- [101] Zaki, K.A., Chen, C., and Atia, A. E.: A circuit model of probes in dual-mode cavity, *IEEE Trans. Microwave Theory Tech.*, vol. 36, pp. 1740-1746, Dec. 1988.
- [102] G. Lastoria, G. Gerini, M. Guglielmi, and F. Emma "CAD of Triple-Mode Cavities in Rectangular Waveguide" *IEEE Microwave Guided Wave Lett.*, vol. 8, pp. 339-342, Oct. 1998.